The HERMES Gaseous Internal Polarized Proton Target and its use in the HERA Positron Storage Ring

Dissertation
der Fakultät für Physik
der Ludwig-Maximilians-Universität München

vorgelegt von
Hauke Kolster
aus Husum

München, 3. Februar 1998

1. Gutachter:	Prof. Dr. G. Graw
2. Gutachter:	Prof. Dr. E. Steffens
Tag der mündlichen Prüfung:	2. April 1998

Zusammenfassung

Das HERMES Experiment ist ein tief-inelastisches Streuexperiment, bei dem polarisierte Leptonen an polarisierten Nukleonen gestreut werden, um die Spinstruktur der Nukleonen zu untersuchen. Im HERMES Experiment kam zum ersten mal ein polarisiertes internes Gastarget bei HERA, einem Hochenergiespeicherring, zum Einsatz. Die hohe Reinheit des Target Materials und die hohe erreichbare Polarisation in dem internen Gastarget, die zu einen hohen Gütefaktor führen, qualifizieren dieses Target für die Verwendung in einem Hochpräzisionsexperiment. Die für die benötigte Statistik erforderliche Targetdichte wird dabei durch den Einsatz einer offenen Speicherzelle erreicht, welche die Aufenthaltszeit der Targetatome im Wechselwirkungbereich des hochenergetischen Strahles erhöht. Die Bestimmung der Targetpolarisation wird dabei durch die Messungenen des Dissoziationgrades und der Polarisation eines Probestrahls aus dem Target durchgeführt.

Die vorliegende Arbeit befasst sich, anhand der mit dem Wasserstoff-Target genommenen Daten, mit folgenden Fragestellungen und Aufgaben:

- die Untersuchung der Rekombination und Polarisation in der HERMES Speicherzelle,
- die Einflüsse des HERA Strahls auf die Speicherzelle und die daraus im Hinblick auf den Teilchentransport folgenden Korrekturen zu den Messungen am Probestrahl,
- die Wechselwirkung der Targetatome mit den durch den HERA Strahl erzeugten hochfrequenten Feldern.

Die Rekombinations- und Relaxationsprozesse in der Speicherzelle lassen sich anhand der Stoßalterverteilungen der Wasserstoffatome untersuchen. Zu diesem Zweck wurden Monte-Carlo Simulationen durchgeführt, welche die Akzeptanz des Targetgas-Analysators und des Polarimeters berücksichtigen. Basierend auf der Diffusion der Atome in der Zelle wurde eine analytische Beschreibung der simulierten Stoßalterverteilungen entwickelt. Die den Diffusionsprozess bestimmenden Parameter für die mittlere Weglänge und Länge der Zelle wurden durch das analytische Modell, nach einer Anpassung an die simulierten Daten, innerhalb einer Abweichung von 3% reproduziert.

Die Messungen des Targetgas-Analysators, einer Neuentwicklung für das HERMES Target, und des Polarimeters wurden beschrieben. Die Kalibrationsmessungen ergaben einen sytematischen Fehler von $\Delta\alpha_r^{\mathrm{TGA}} = 0.01$ und $\Delta P_r^{\mathrm{BRP}} = 0.009$ für die jeweiligen Messungen. Die Unsicherheit der Messung des unpolarisierten molekularen Anteils des Targets aus Restgas-Strömung aus der Targetkammer und ballistischem Fluß von der Atomstrahlquelle ergibt sich zu $\Delta\alpha_0^{\mathrm{TGA}} = 0.01$ Es wurden Messungen der Rekombination und Polarisation in einem Temperaturbreich von 35 K bis 250 K bzw. von 35 K bis 110 K bei einem magnetischen Haltefeld von 335 mT mit einer sauberen bzw. einer wasserbedeckten Drifilmoberfläche durchgeführt. Die gemessenen Werte für Rekombination und Polarisation erstreckten sich dabei in einen Bereich von 0.2 bis 1.0 atomaren Anteil des Wasserstoffgases bzw. 10% bis 92% Polarisation der Atome.

Modellrechnungen für die Rekombination und Polarisation unter der Annahme einer Langmuir-Bedeckung der Oberfläche und Oberflächendiffusion als treibenden Prozeß der Depolarisation zeigen gute Übereinstimmung mit den gemessenen Daten. Ein Vergleich der Ergebnisse der Rekombinationsmessungen der mit Drifilm beschichteten Zelle mit dem zugrunde gelegten Modell zeigen, daß die Wasserstoffatome auf zwei verschiedenen Bindungsstellen adsorbieren, wobei die erste Bindung als Chemisorption mit einer Bindungsenergie von $E_0^{(1)} = (0.611 \pm 0.015)\,\mathrm{eV}$ und die zweite als Physisorption mit einer Bindungsenergie von $E_0^{(2)} = (0.0318 \pm 0.0004)\,\mathrm{eV}$ identifiziert werden konnte. Der Hochtemperaturlimes der mittleren Haftungsdauer τ_s der Atome auf der Oberfläche, die sich gemäß $\tau_s = \tau_s^0 \exp(E_0/\mathrm{k}T)$ verteilt, konnte zu $\tau_s^0 = (1.0 \pm 0.2) \cdot 10^{-10}\,\mathrm{s}$ bestimmt werden. Die Messungen der Polarisation wurden simultan mit den Messungen der Rekobmination durchgeführt. Ein erwarteter Polarisationsverlust von 3.5% durch Spinaustausch-Wechselwirkung der Atome in der Zelle wurde beobachtet. Die Grössen, die die Diffusion der Atome auf der Oberfläche bestimmen, wie die Korrelations Zeit $\tau_c = \tau_c^0 \exp(\Delta E_j/\mathrm{k}T)$ und die für die Diffusion zu überwindende Potentialbarriere ΔE_j, sind in guter Übereinstimmung mit $\tau_c^0 = 2.5 \cdot 10^{-12}\,\mathrm{s}$ und $\Delta E_j^{(2)} = 0.49\, E_0^{(2)}$.

Die ersten bei HERMES durch die Strahlwechselwirkungen hervorgerufenen depolarisierenden Resonanzen in der Speicherzelle wurden gemessen. Die gemessene Resonanzform der kerndepolarisierenden Resonanzen wurde mit Hilfe eines analytischen Modells basierend auf der Zellgeometrie beschrieben. Eine Abschätzung für die Ausdehnung des Wechselwirkungsbereiches bei den kerndepolarisierenden Resonanzen, $l_{\mathrm{int}} = 2.5\,\mathrm{mm}$, und die longitudinale Ausdehnung der hochfrequenten Felder des Positronen Strahls, $\Delta z_{\mathrm{fwhm}} = (16.5 \pm 0.5)\,\mathrm{mm}$, konnte gewonnen werden. Bei dem nominalen Haltefeld von 335 mT ist der Abstand der kerndepolarisierenden Resonanzen groß, am Arbeitspunkt konnte keine Depolarisation der Kerne konnte beobachtet werden.

Die Messungen der Rekombination bei einer Zelltemperatur von 100 K mit der Drifilm Oberfläche zeigten einen gemessenen Dissoziationsgrad von $\alpha_r^{\mathrm{TGA}} \approx 0.9 - 0.95$. Während des Betriebs des Beschleunigers wurde die Drifimoberfläche angegriffen und eine Verringerung auf $\alpha_r^{\mathrm{TGA}} \approx 0.2$ beobachtet. Ein indirekter Nachweis einer Wasserbedeckung in der Zelle ist gegeben, die von Wasser, das in dem ABS Dissoziator produziert wird, herrührt. Die Messungen mit der wasserbedeckten Drifilmoberfläche zeigten einen Anstieg des gemessenen Dissoziationsgrades auf $\alpha_r^{\mathrm{TGA}} \approx 1$. Der Einfluß der Wasserbedeckung auf die Polarisation is gering und Werte von $P^{\mathrm{BRP}} = 0.92$, $\alpha_r^{\mathrm{TGA}} \approx 1$ und $\alpha_0^{\mathrm{TGA}} \approx 0.97$ wurden im Falle eines vollständig optimierten Targets gemessen.

Abstract

The HERMES experiment at HERA studies the spin structure of the nucleon using deep-inelastic positrons scattered off polarized nucleons. It is the first experiment, which makes use of an internal polarized target inside a high energy beam environment. The figure of merit qualifies the internal gas target for the use in a high precision experiment, because of the purity of the target material and the high polarization, which can be achieved. The target thickness required for high statistics is obtained by use of the storage cell technique. The polarization and degree of dissociation of the target is measured using a sample beam from the target. Additional requirements on the target components are given by the accelerator environment. Strong synchrotron radiation and possible interactions of ions with the cell surface limit the lifetime of the components. Additional interactions with the transient fields of the strongly bunched high energy positron beam are expected.

The work presented investigates the interactions of the internal target with the high energy positron beam of the HERA accelerator based on the data taken with the hydrogen target. It focuses on the following topics:

- investigation of the recombination and depolarization processes inside the HERMES target cell,
- the influence of the HERA beam on the storage cell and the resulting corrections on the external measurements with regard to the particle transport through the cell,
- the interaction of the target atoms with the transient fields of the HERA beam (beam induced resonances).

The particle motion inside the storage cell was studied by means of a Monte-Carlo simulation. An analytical model is used to study the interactions of the atoms with the cell surface and the influence of the recombination and polarization on the target. Calculations for both processes, which are based on the assumption of a Langmuir type surface coverage and a diffusion process as the driving mechanism for the depolarization, show agreement with the measured data.

The first measurements of beam induced depolarizing resonances at HERA are presented and the observed resonance shape can be explained by an analytic model based on the cell geometry. No depolarizing effects were found at the nominal operation point of the target holding field. The cause for changes in the surface properties of the cell was identified as a water coverage generated by the atomic beam source. This water coverage was found to inhibit recombination and results in a high degree of dissociation and high average target polarization.

Acknowledgements

Mein besonderer Dank gilt Prof. Dr. G. Graw, der mir die Durchführung dieser Arbeit ermöglicht hat und mit viel Einsicht und Diskussionvermögen zum Verständnis beigetragen hat, sowie Herrn Prof. Dr. E. Steffens, der diese Arbeit am Max Planck Institut für Kernphysik in Heidelberg und am DESY in Hamburg mitbetreut hat. Dem DESY Direktorium möchte ich für die Möglichkeit danken, diese Arbeit am DESY durchführen zu können. Bei Herrn Prof. Dr. B. Povh bedanke ich mich dafür, daß er die Durchführung der Arbeit am Max-Planck-Institut für Kernphysik in Heidelberg ermöglicht hat. An dieser Stelle möchte ich mich für die freundliche Aufnahme in die Münchner und Heidelberger Arbeitsgruppen bedanken. Wieterhin danke ich stellvertretend für die Heidelberger Werkstätten Herrn Hornung, Herrn Mallinger und Herrn Ochman für die große und tatkräftige Hilfe beim Aufbau des Polarimeters in Heidelberg und Hamburg.

Im Laufe der Zeit ist das HERMES Target aus den Einzelkomponenten, die unter anderem in Heidelberg, Liverpool, Madison und am DESY/Hamburg entwickelt wurden, zu einer Einheit zusammengewachsen und viele Personen sind an dem Aufbau und der erfolgreichen Inbetriebnahme beteiligt gewesen. Zu nennen und zu danken sind hier neben vielen anderen Dr. B. Braun, A. Metz, C. Baumgarten, E. M. Gabriel für die Arbeit am Polarimeter und am Targetgas-Analysator, Dr. F. Stock, U. Funk, A. Golendoukhin und N. Koch für die Arbeit an der Atomstrahlquelle, Dr. G. Court, Dr. J. Stewart, J. Morton, D. Muskett für die Arbeit am Targetmagneten und Kryotechnik, T. Wise für die Arbeit an der Targetzelle, sowie Prof. Dr. R. Milner, M. Sutter, T. Shin, J. Martin für die Arbeit am unpolarisierten Gaseinlaßsystem. Weiterhin seien Dr. R. Hertenberger, C. Grosshauser, Dr. J. Stenger, R. Schmitz, Prof. Dr. P. Dalpiaz, S. Frabetti und A. Reali für die Mitarbeit bei der Installation der einzelnen Komponenten gedankt, sowie Dr. Y. Holler, V. Prahl, J. Plett, K. Hakelberg, E. Hänisch und M. Jürgens für die Unterstützung beim Aufbau in der HERMES Experimentierhalle und Dr. W. Brückner und Dr. M. Kirsch für die Hilfe beim Aufbau der Datennahme.

Bei B. Braun, C. Baumgarten und M. Henoch, die wesentlich für die Entwicklung und Durchführung der Monte-Carlo Simulationen und Polarimeter Kalibration verantwortlich sind, bedanke ich mich für die Überlassung der Simulations- und Polarimeter-Kalibrationsergebnisse. Zu erwähnen sind noch die Beiträge von C. Baumgarten und C. Simani bei der Kalibration des Targetgas-Analysators.

Allen Mitgliedern der Targetgruppe des HERMES Exprimentes danke ich für die vielen Anregungen und ein ausgezeichnetes Arbeitsklima sowie der HERMES Kollaboration für die gute Zusammenarbeit.

Besonders m"ochte ich mich bei meinen lieben Eltern Ingrid und Dieter und meinem Bruder Sönke bedanken sowie bei Allison für die Unterstützung, die mir diese Arbeit erst möglich gemacht hat.

Table of Contents

List of Figures

List of Tables

1 Introduction

The HERMES experiment is designed to study the spin structure of the nucleon at HERA by use of spin-dependent deep inelastic scattering of positrons scattered off polarized nucleons. In the quark parton model, the nucleon spin s_z is composed of the spin contributions of the valence quarks Δu and Δd, the sea quarks Δq_s, the contributions from the gluons ΔG, and angular momentum L_z

$$s_z = \frac{1}{2} = \frac{1}{2}(\Delta u + \Delta d + \Delta q_s) + \Delta G + L_z. \tag{1.1}$$

The goal of the experiment is to measure these spin contributions as functions of the Bjorken variable x, the fraction of the total momentum of the nucleon carried by the struck quark, and the momentum transfer Q^2. Sum rules based on integrals of quark distribution functions were derived from theoretical considerations. Predictions in comparison with the experimental results allow to test basic assumptions about the spin structure of the nucleon. The assumption, that the total spin contribution of the strange quark is negligible, $\Delta s = 0$, leads to the Ellis-Jaffe sum rules for proton and neutron.

First experiments on spin dependent deep inelastic scattering were carried out at SLAC [Al76, Bau83] in the 70's and 80's, which agreed with the assumption, $\Delta s = 0$. Further studies were done at CERN [Ant93, Abe95, Ade93] by the European Muon Collaboration (EMC)[Ash88], which found a violation of the Ellis-Jaffe sum rule for the proton. This so called 'spin crisis' led to proposal of new experiments, such as the HERMES experiment at DESY [Her90, Her93].

In the former experiments, the separation of the different quark flavors, which was based on inclusive measurements, was only possible in an indirect manner. The direct separation requires a good particle identification, a thin target with low dilution, and semi-inclusive hadron measurements, which are possible with open spectrometers like the ones used at SMC and HERMES.

The developments at the HERA accelerator at DESY have led to the first longitudinal spin polarized beam in a high energy electron storage ring. This allows the use of the new technique of a polarized internal gas target for the study of spin dependent interactions in the HERMES experiment. The storage cell technique was introduced and tested in an accelerator environment at low and intermediate energies up to 2 GeV [Gil90, Bra92, Lor93, Zho96]. The advantage of the internal target technique is a pure target without dilution by species other than the target material and a high polarization up to 0.90 for hydrogen and deuterium targets [Bra95].

1.1 The HERMES Experiment

The HERMES experiment is located in one of the four experimental areas of the HERA storage ring, a proton-electron collider at DESY/Hamburg (Fig 1.1). HERMES makes use of the HERA the electron beam in combination with the internal gas target. The measurements with the polarized hydrogen target at HERMES were carried out using a positron beam. The energy of the positrons was 27.5 GeV with a maximum beam current

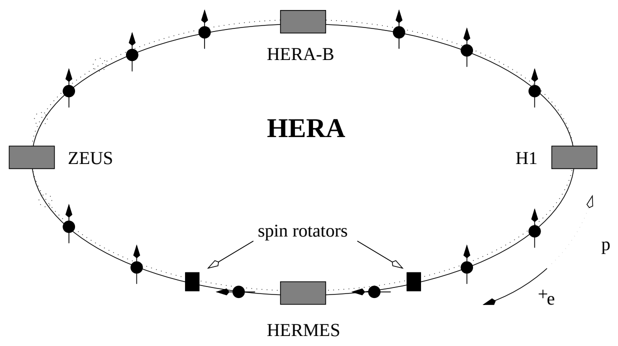

Fig. 1.1: Schematic of the HERA accelerator at DESY. The transverse polarization of the positrons in the ring results from the Sokolov Ternov effect. The HERMES experiment is located in between two spin rotators to provide a longitudinally polarized positron beam.

of 42 mA. The luminosity achieved is in the order of $10^{31}\,\mathrm{cm}^{-2}\,\mathrm{s}^{-1}$. Because HERA was designed for colliding experiments, the structure of the positron beam is highly bunched. It allows 220 bunches to be filled with positrons, which are separated by 96 ns. The positrons are transversally polarized due to the Sokolov-Ternov effect [Sol64]. To provide longitudinal polarized positrons at the HERMES experiment a set of spin rotators is installed at both ends of the experiment. During run of the spin rotators a maximum polarization of 65% was achieved. Polarimeters for the measurement of the longitudinal and transversal polarization were installed in the respective areas.

1.2 The Internal Gas Target at HERMES

Figure 1.2 shows a perspective view of the HERMES target as it is installed in the HERMES experiment. Figure 1.3 gives a scematic overview of the different components. The storage cell is located along the axis of the positron beam in the center of the target chamber with the cell axis in $+z$ direction, upstream the HERA beam. The Stern Gerlach atomic beam source (ABS) feeds polarized hydrogen atoms into the storage cell. The high polarization of the atoms inside the cell is maintained by a strong longitudinal holding field. A sample beam is extracted from the target center and is analyzed by a target gas analyzer and a Breit-Rabi type polarimeter.

The target thickness achieved within the interaction region of the positron beam by use of the storage cell technique is $7 \cdot 10^{13}\,\mathrm{cm}^{-2}$ [Sto94a, Sto95], which is more than two orders of magnitude higher compared to the target thickness achieved by a free jet target of $2 \cdot 10^{11}\,\mathrm{cm}^{-2}$ [Dun84, Dmi85]. The spin state of the target is set every 60s with a switching time of less than 1s. The order of the two spin states is randomly selected by the ABS at a constant holding field in the target. The target atoms remain inside the cell for typically 3 ms and cross the interaction region multiple times. Inside the target cell the target atoms are subject to various effects due to interactions with fields and cell walls, which are

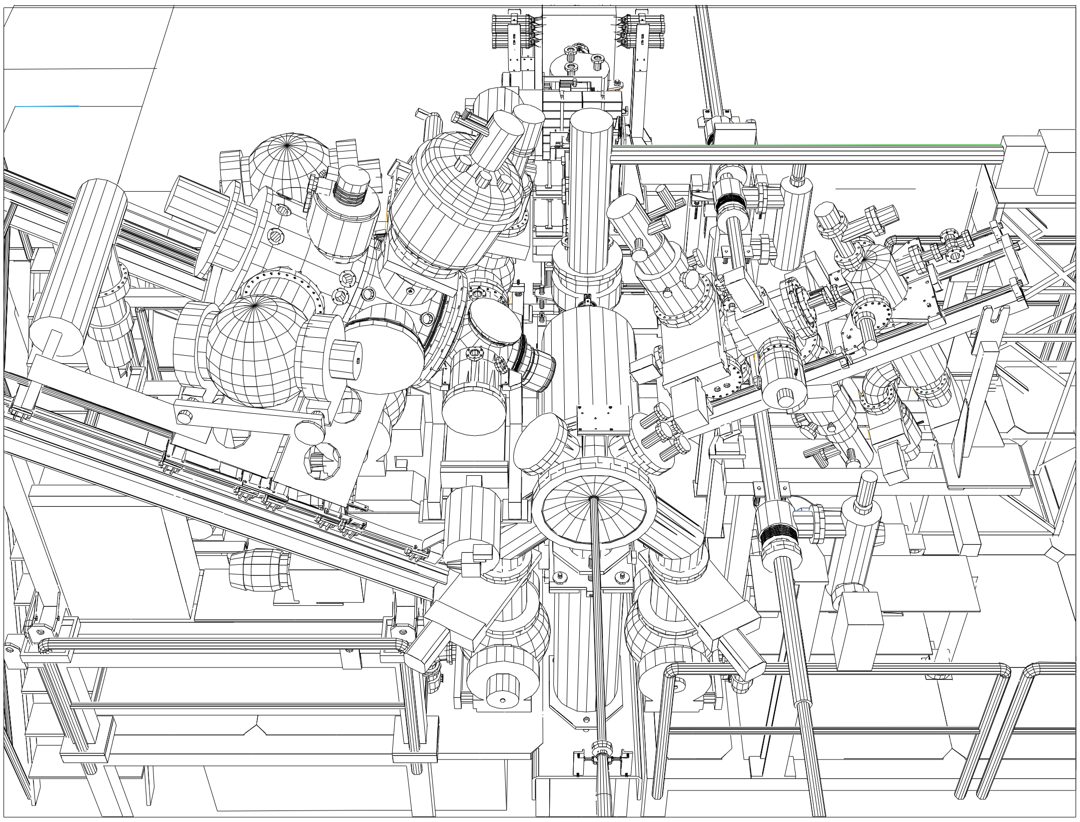

Fig. 1.2: Overview of the internal target at HERMES. The view is in $(-z)$ direction upstream the positron beam line. The picture shows the target platform supporting the ABS (left), the BRP (right), the pump stations (center in front) and the target chamber (center, above the pump stations) surrounded by the target magnet. The positron beam line in the center passes the thin walled exit window of the target chamber. The proton beam line (to the right) intersects the polarimeter support frame.

- Recombination: the atoms inside the cell can recombine at the cell walls and form molecules, which contribute to the target density.
- Wall depolarization: the wall collisions of the atoms causes them to remain on the surface for a brief time where they interact with surface magnetic fields, which lead to a relaxation of the atom polarization.
- Spin exchange collisions: a collision of the atoms in the gaseous phase inside the cell may lead to a spin exchange between the hyperfine states of the atoms and cause exchange of electron and proton polarization.

Previous studies in test experiments using different surface materials as coatings of the storage cell were made to find a suitable cell coating, which prevents the target atoms from recombining and inhibits relaxation of the target polarization. Recombination and

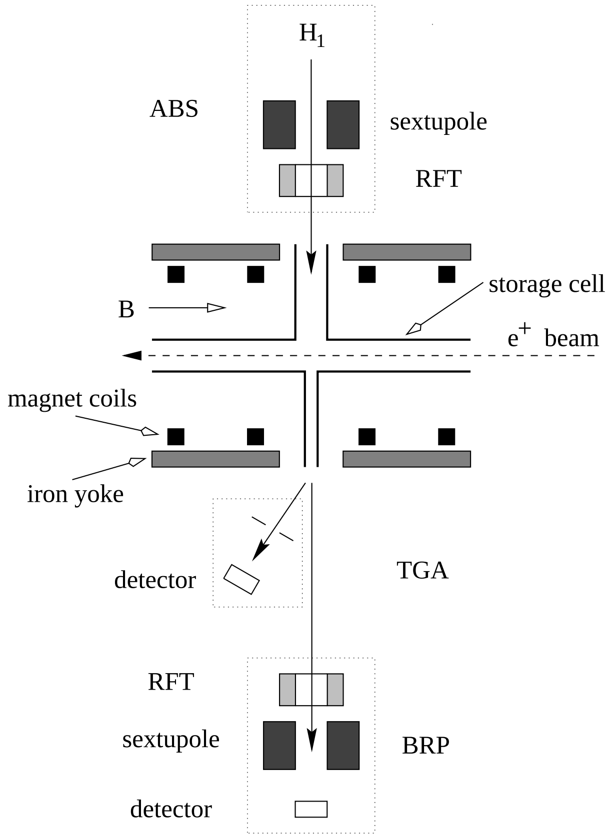

Fig. 1.3: Schematic of the HERMES target.
From top to bottom: Atomic beam source (sextupole magnets and RF transition units); target cell and positron beam; target magnet coils to provide the holding field; target gas analyzer (aperture and detector); Breit-Rabi polarimeter (RF transition units, sextupole magnets and quadrupole mass spectrometer (QMS) for single ion detection).

depolarization of hydrogen and deuterium atoms at high and low magnetic holding fields inside a storage cell was studied by Price [Pri93a, Pri93b] as a function of the temperature of the cell. Detailed studies of the temperature and magnetic field dependence of the depolarization of hydrogen and deuterium due to wall collisions and spin exchange collisions were performed by Braun [Bra90, Bra95]. The results show that a Drifilm coating on bare aluminum is able to inhibit the recombination and depolarization to a high degree, so a high target polarization should be maintained at the HERMES target. The measurements [Bra95] also indicate that a significant amount of water is injected into the storage cell by ballistic flow from the ABS dissociator. It originates from an admixture of oxygen in the ABS dissociator which improves the dissociation process [Wis67, Kor90]. The data give evidence of a change in the recombination rate dependent on the amount of water on the cell surface.

The recombination and polarization measurements at HERMES are carried out based on a sample beam of the target gas, which is extracted from the target cell through an additional sample tube. For atoms which are detected externally the average number of wall collisions of the atoms inside the target cell is different from the number of wall collisions of the atoms, which are detected in the sample beam. Because the recombination and relaxation depend on the number of collisions the measurements need to be corrected for the additional interactions the atoms undergo while leaving the cell. For this purpose, a Monte Carlo code was developed [Bra90], which simulates the particle motion through the cell. It gives information about the age distribution of the atoms at any position in the cell. The average polarization of a sample of atoms can be described in this model by

$$\langle P \rangle = \int_0^\infty P(0) A(b) \exp\left(-2 P_{\text{flip}}\, b\right) db, \tag{1.2}$$

where b is the number of wall collisions an atoms has inside the cell (collision age), $A(b)$ is the distribution of the collision ages of the atoms in the sample, P(0) is the initial polarization of the atoms in the sample, and P_{flip} is the probability for a spin flip to occur during a wall collision. Due to the dependence of the polarization on the number of wall collisions the difference between the quantities measured and the quantities inside the cell can be expressed by a correction factor.

Additional interactions of the HERMES target with the positron beam of the accelerator are expected to occur:

- Beam induced resonant depolarization: the bunch structure of the positron beam leads to high transient magnetic fields with an equidistant frequency spectrum including components up to the GHz range. These fields induce resonant transitions of the target atoms which lead to depolarization.

- Changes in the cell coating: the high amount of synchrotron light due to the high energy of the beam can potentially destroy the surface material, which would results in an increase of the recombination and depolarization of the target atoms. The possible interaction of the transient fields of the beam with water adsorbed on the surface would lead to a beam current dependent change of the recombination and polarization.

The effect of beam induced resonances inside the HERMES target was studied theoretically by Kinney [Kin91a, Kin91b, Kin93]. The results gave the design criteria for the target holding field magnet [Ste95, Ste97], so that the magnetic holding field is sufficiently uniform to have magnetic holding field settings free of depolarizing resonances.

Figure 1.4 shows a measurement period in 1996 with the measurement of the degree of dissociation and the cell temperature after a warm up of the target cell to $T_c = 280\,\mathrm{K}$. The degree of dissociation before the warm up was measured to be $\alpha^{\mathrm{TGA}} \approx 0.9$. The cell was then cooled down to 50 K for measurements with unpolarized target gas and set to 100 K for measurements with polarized hydrogen atoms. The degree of dissociation was lowered to a value of $\alpha^{\mathrm{TGA}} \approx 0.5$ directly after the warmup and increased slowly during ABS operation only. The measurements with unpolarized gas (intervals UP) did not change the degree of dissociation. The differences in the degree of dissociation, which are caused by the cell heating, and its dependence on the ABS operation indicates that these changes are related to water, which is produced in the ABS dissociator and enters the target cell as ballistic flow. During the heating of the cell the water evaporated from the cell surface and is pumped from the target chamber. After cooling of the cell it slowly adsorbed on the surface during ABS operation.

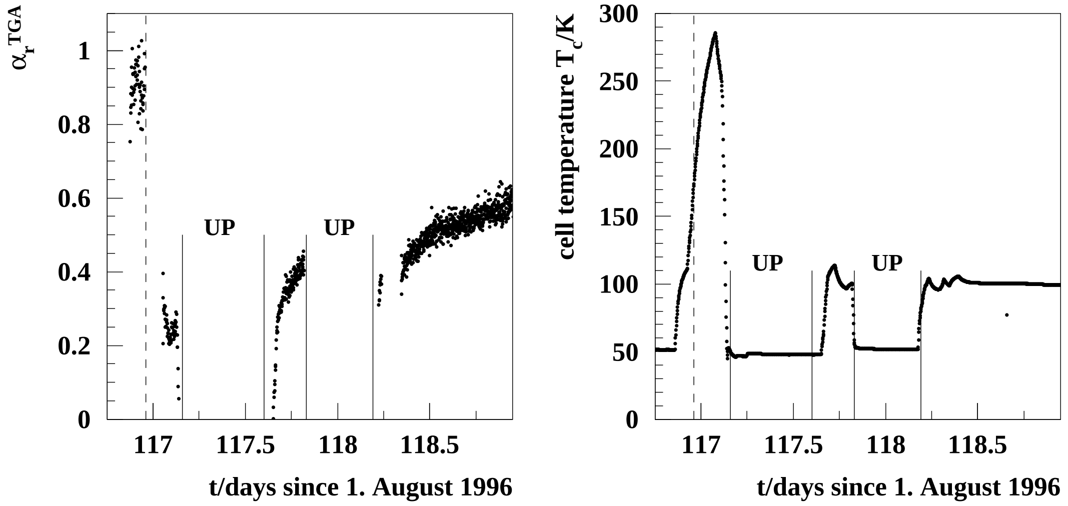

Fig. 1.4: Change in the measured degree of dissociation related to the ABS operation. The plots show a measurement period in 1996 with the measurement of the degree of dissociation (left) and the cell temperature (right), where the cell was warmed up to 280 K and cooled down again to 50 K for measurements with unpolarized target gas (interval UP) and 100 K for measurements with polarized atomic hydrogen. The increase of the degree of dissociation after cooling of the cell is related to running of the ABS only.

A plot of the measured recombination and polarization versus the positron beam current is shown in Fig.1.5, demonstrating how the beam interactions can affect the HERMES target. The upper figure shows the mass 1 signal measured by the target gas analyzer, which is reduced if recombination inside the target cell takes place. The center figure shows the HERA positron current. The time intervals when the beam was injected and the time interval of normal beam are indicated. The lower picture shows the electron and proton polarization of the hydrogen atoms measured by the polarimeter. The recombination shows a dependence on the beam current, which might be related to the removal of water, which is adsorbed on the surface. The change in recombination is clearly related to the positron beam current. The electron polarization is lowered during the injection phase of the positron beam due to beam induced resonances. The time structure of the HERA beam depends on the energy and after injection at higher beam energy the resonances are suppressed. The proton polarization shows only little changes when the change of the recombination or the depolarization of the electrons takes place.

1.3 Hyperfine Splitting of Hydrogen

Several components of the HERMES target make use of the hyperfine splitting of hydrogen. The sextupole systems in the ABS and the BRP use the sub-state dependent

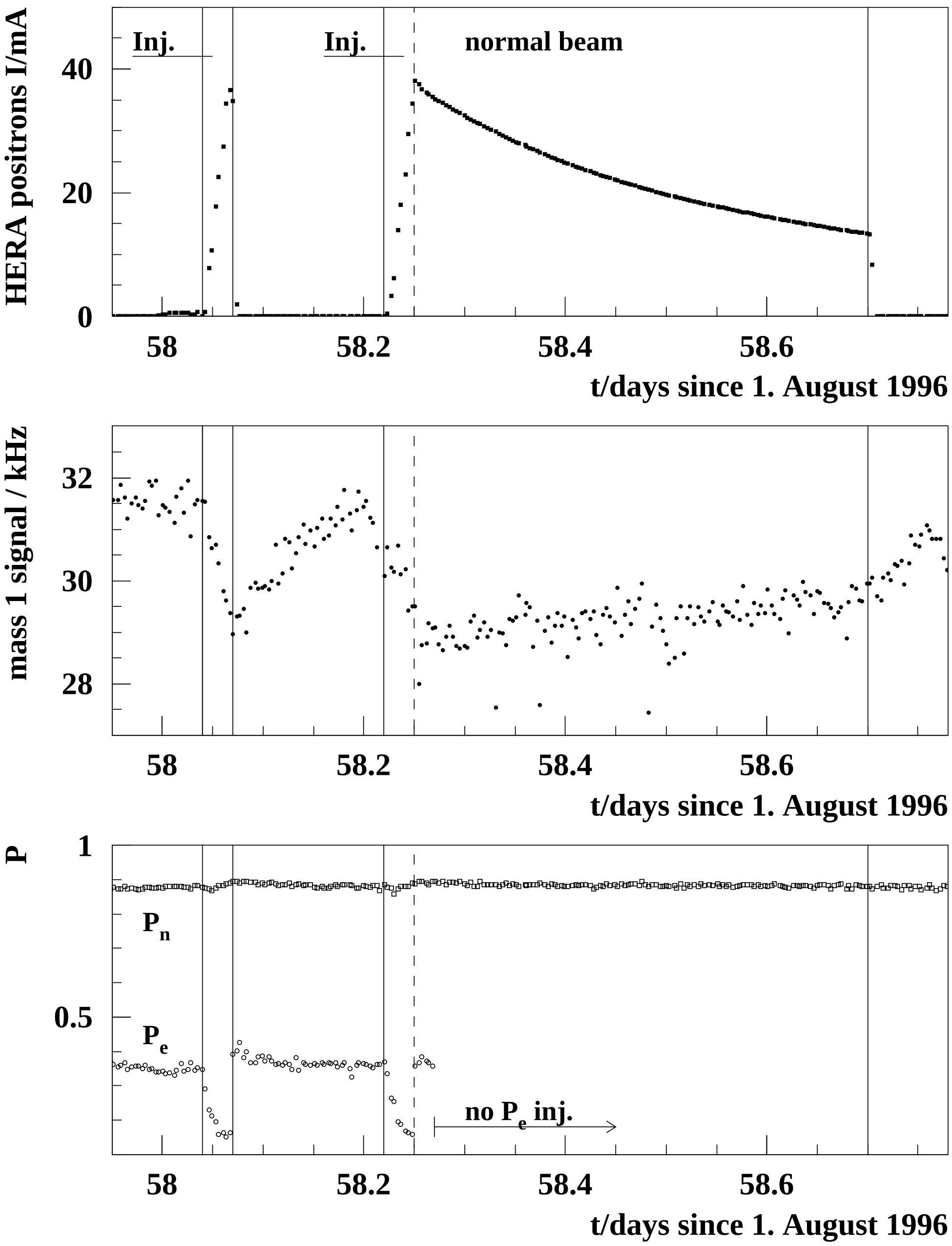

Fig. 1.5: Target performance during a HERA fill in 1996. The HERA positron beam current (upper), mass 1 beam signal measured by the target gas analyzer (center), polarization measured by the polarimeter (lower) versus time. P_n is the proton polarization and P_e is the electron polarization of the hydrogen atoms. The times with injection of the beam and normal beam are indicated.

forces inside the sextupole magnets for the selection of the spin states. A high magnetic holding field is used to maintain a high polarization inside the target cell making use of the magnetic field dependence of the expectation values for the polarization of the single sub-states.

A hydrogen atom in the ground state $1s$ is a system of two spin $\frac{1}{2}$ $\mathbf{I}$ and $\mathbf{S}$, coupled by the hyperfine interaction $\mathbf{H}_{\text{hf}} = \mathcal{A}\mathbf{I}\cdot\mathbf{S}$, where $\mathcal{A}$ is a constant and $\mathbf{I}$ and $\mathbf{S}$ are the proton and electron spin operators, respectively. The eigenstates are expanded in the basis formed by the eigenvectors common to $\mathbf{S}^2, \mathbf{I}^2, S_z, I_z$: $\left| S=\frac{1}{2}; I=\frac{1}{2}; m_S; m_I \right\rangle$. The spins of electron and proton couple to the total angular momentum $F=0$ or $F=1$, where the degeneracy of the state $F=1$ is equal to 3. The splitting of the energy values due to this interaction is the hyperfine splitting. The total angular momentum $\mathbf{F}=\mathbf{S}+\mathbf{I}$ defines eigenstates common to $\mathbf{S}^2, \mathbf{I}^2, \mathbf{F}^2, F_z$: $\left| S=\frac{1}{2}; I=\frac{1}{2}; F; m_F \right\rangle$ with eigenvalues

$$E(F=1) = \frac{1}{4}\mathcal{A}\hbar^2 \;\; \text{and} \;\; E(F=0) = -\frac{3}{4}\mathcal{A}\hbar^2. \tag{1.3}$$

For atoms in an external magnetic field B parallel to the axis $\mathbf{e}_z$ the interaction of the magnetic moments with the external field removes the degeneracy of the state $F=1$. This field dependence is described by the additional contribution $\mathbf{H}_{\text{e}} = \mathbf{M}_{\mathbf{S}}\cdot \mathrm{B} + \mathbf{M}_I \cdot \mathrm{B}$ to the Hamiltonian, where $\mathbf{M}_S$ and $\mathbf{M}_I$ are the magnetic moments of the electron and proton spins, respectively, and $\mathbf{B}$ is the external magnetic field. The total Hamiltonian for hydrogen in the presence of an external magnetic field B is

$$\mathbf{H} = \mathbf{H}_{\text{hf}} + \mathbf{H}_{\text{e}} = \mathcal{A}\mathbf{I}\cdot\mathbf{S} + \omega_S S_Z - \omega_I I_Z, \tag{1.4}$$

where ω_S and ω_I, the Larmor angular frequencies in the field $B=(0,0,B_0)$, are defined as

$$\begin{aligned} \omega_S &= \frac{g_e\mu_e}{\hbar}B_0, \\ \omega_I &= \frac{g_p\mu_p}{\hbar}B_0, \end{aligned} \tag{1.5}$$

where g_e, g_p and μ_e, μ_p are the g-factors and magnetic moments of the electron and proton, respectively.

The configuration $|\,1;1\,\rangle$ and $|\,1;-1\,\rangle$ in the representation $|\,F;m_F\,\rangle$ are eigenfunctions of the Hamiltonian Eq.(1.4) independent of the strength of the external magnetic field. The remaining two eigenstates are linear combinations of the states $|\,0;0\,\rangle$ and $|\,1;0\,\rangle$. The eigenenergies E_i of the four substates $|\,i\,\rangle$ are

$$\begin{aligned} E_1 &= \quad \tfrac{1}{4}\mathcal{A}\hbar^2 + \tfrac{1}{2}\hbar\,(\omega_S-\omega_I), \\ E_2 &= - \quad \tfrac{1}{4}\mathcal{A}\hbar^2 + \sqrt{\left(\tfrac{1}{2}\mathcal{A}\hbar^2\right)^2 + \tfrac{1}{4}\hbar^2(\omega_S+\omega_I)^2}, \\ E_3 &= \quad \tfrac{1}{4}\mathcal{A}\hbar^2 - \tfrac{1}{2}\hbar\,(\omega_S-\omega_I), \\ E_4 &= - \quad \tfrac{1}{4}\mathcal{A}\hbar^2 - \sqrt{\left(\tfrac{1}{2}\mathcal{A}\hbar^2\right)^2 + \tfrac{1}{4}\hbar^2(\omega_S+\omega_I)^2}. \end{aligned} \tag{1.6}$$

The dependence of the energies of the hyperfine states on the magnetic field strength is shown in Figure 1.6. The energy is plotted in units of the hyperfine splitting energy

$$E_{\text{hf}} = \mathcal{A}\hbar^2 = h\nu_{\text{hfs}}\,,\;\; \nu_{\text{hfs}} = 1\,420.4\,\text{MHz} \tag{1.7}$$

and the magnetic field is plotted in units of the critical field B_c, $x = B_0/B_c$, which is given by the condition $\hbar(\omega_S - \omega_I) = \mathcal{A}\hbar^2$. The value is

$$B_c = \frac{\mathcal{A}\hbar}{g_s\mu_B} = 50.7\,\mathrm{mT}. \tag{1.8}$$

The critical field is useful to characterize the interaction within different ranges of the

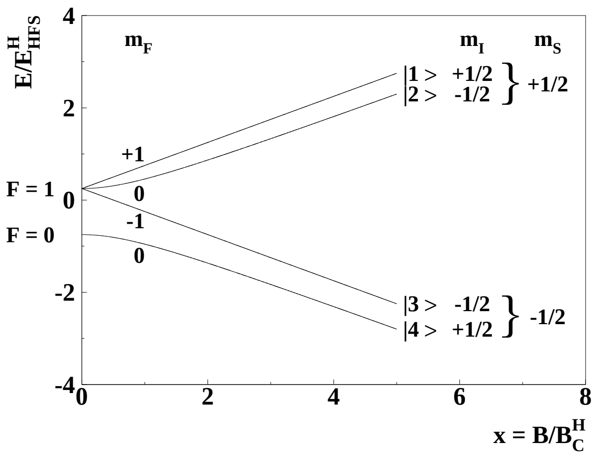

Fig. 1.6: Hyperfine splitting of hydrogen. The energy of the substates $|\,i\,\rangle$ of hydrogen is plotted versus the strength of the magnetic field in units of the critical field $B_c = 50.7\,\mathrm{mT}$.

external magnetic field:

- $B_0 \ll B_c$ (weak fields): $\mathbf{H}_{\mathrm{hf}} \gg \mathbf{H}_{\mathrm{e}}$, this is the Zeeman regime and $\mathbf{H}_{\mathrm{e}}$ can be seen as a perturbation. The basis $|\,F; m_F\,\rangle$ is a good approximation for the eigenvectors $|\,i\,\rangle$.

- $B_0 \gg B_c$ (strong fields): $\mathbf{H}_{\mathrm{hf}} \ll \mathbf{H}_{\mathrm{e}}$, the hyperfine term can be seen as a perturbation of the strong field states and the basis $|\,m_S; m_I\,\rangle$ is a good approximation for the eigenvectors $|\,i\,\rangle$.

In the case of an arbitrary external field the four substates $|\,i\,\rangle$ are defined in the basis $|\,m_S; m_I\,\rangle$ introducing a mixing angle θ defined as

$$\tan 2\theta = \frac{1}{x}. \tag{1.9}$$

The values of θ at the limits of $x = B/B_c$ are

$$\begin{array}{ll} x = 0 & \Rightarrow \theta = \frac{\pi}{4}, \\ x \to \infty & \Rightarrow \theta = 0. \end{array} \tag{1.10}$$

The eigenfunctions $|\,i\,\rangle$ of the Hamiltonian Eq. (1.4) then are

$$\begin{aligned} |\,1\,\rangle &= \;|+;+\,\rangle\,, \\ |\,2\,\rangle &= \;\cos\theta\,|+;-\,\rangle \;+\; \sin\theta\,|-;+\,\rangle\,, \\ |\,3\,\rangle &= \;|-;-\,\rangle\,, \\ |\,4\,\rangle &= \;\sin\theta\,|+;-\,\rangle \;-\; \cos\theta\,|-;+\,\rangle\,. \end{aligned} \tag{1.11}$$

The polarization of a sample of particles is given by the expectation value

$$P_{e,z} = \sum_{i=1}^{4} n_i \, \langle\, i \,|\, \mathcal{P}_{e,z} \,|\, i \,\rangle \,, \tag{1.12}$$

where the n_i are the relative occupation numbers of state $|\, i \,\rangle$ in the sample, normalized to one, $\sum_i n_i = 1$, and $\mathcal{P}_e$ and $\mathcal{P}_z$ are the projection operators of the electron or proton polarization, respectively,

$$\begin{array}{ll} \langle\, 1 \,|\, \mathcal{P}_e \,|\, 1 \,\rangle = +1, & \langle\, 1 \,|\, \mathcal{P}_z \,|\, 1 \,\rangle = +1, \\ \langle\, 2 \,|\, \mathcal{P}_e \,|\, 2 \,\rangle = +\cos 2\theta, & \langle\, 2 \,|\, \mathcal{P}_z \,|\, 2 \,\rangle = -\cos 2\theta, \\ \langle\, 3 \,|\, \mathcal{P}_e \,|\, 3 \,\rangle = -1, & \langle\, 3 \,|\, \mathcal{P}_z \,|\, 3 \,\rangle = -1, \\ \langle\, 4 \,|\, \mathcal{P}_e \,|\, 4 \,\rangle = -\cos 2\theta, & \langle\, 4 \,|\, \mathcal{P}_z \,|\, 4 \,\rangle = +\cos 2\theta. \end{array} \tag{1.13}$$

Using the identity $\cos 2\theta = \frac{x}{\sqrt{1+x^2}}$ the polarizations can be written as

$$\begin{array}{l} P_e = n1 - n3 + (n2 - n4)\frac{x}{\sqrt{1+x^2}}, \\ P_z = n1 - n3 - (n2 - n4)\frac{x}{\sqrt{1+x^2}}. \end{array} \tag{1.14}$$

After giving an overview of the setup of the target, this thesis will focus on three topics: the measurements of recombination and polarization, the relation of the externally measured quantities to the ones inside the cell, and the target beam interactions.

Chapter two gives an overview of the experimental apparatus of the HERMES target and the data acquisition. It describes the measurement methods and calibrations of the target gas analyzer and the polarimeter.

Chapter three describes the particle motion through the target cell and presents Monte-Carlo results for the HERMES setup. An analytical approximation for the Monte Carlo data is developed, which is used for further calculation of the correction factors for recombination and polarization. The dependence of recombination and polarization of a sample of atoms on the collision age distribution is shown.

Chapter four introduces the theory for recombination based on a model in which recombination occurs between a gaseous atom and an adsorbed atom, which collides with the cell walls and is adsorbed. The bound state of the adsorbed atom is described by a binding energy and a harmonic potential. The temperature of the cell alters the coverage of the surface and the recombination rate is calculated through the collision rate of the gaseous and the adsorbed atoms. Recombination measurements for a wide temperature range with a clean and a water coated cell are presented and discussed.

In Chapter five the theory of spin exchange collisions and wall relaxation is introduced. The model for wall relaxation is based on surface diffusion of the atoms. This leads to fluctuating fields, with which the atoms interact. The underlying process is a resonant depolarization due to the frequencies in the spectrum of the fluctuating fields. The temperature of the cell causes a change in the diffusion rate which results in a change of the frequency spectrum and the relaxation rate. Polarization measurements for a wide temperature range with a clean and a water coated cell are presented and discussed.

Chapter six presents the first measurements of the beam induced resonances measured at HERMES. A simple analytical model is introduced for the proton depolarizing resonances, which is able to explain the observed resonance shape based on the cell geometry. An additional measurement of the electron resonances is presented and discussed.

The definitions for the degree of dissociation and the polarization of the total target based on the measurements of the target gas analyzer and Polarimeter are given in Chapter seven. Additional measurements of the recombination inside the cell using the HERMES luminosity monitor, which gives an independent measurement, are discussed. The polarization of the molecules which are formed by recombined atoms inside the target cell and their contribution to the total target polarization is discussed.

2 The Experimental Setup

This chapter describes the setup of the internal target which was developed for the HERMES Experiment. The components of the internal target which are important in the present context are shown in Figure 1.3. In the atomic beam source (ABS) [Sto94b, Sto94a, Sto95, Ste97] the atomic hydrogen electrons are polarized using Stern-Gerlach-separation in a sextupole system. Adiabatic RF transitions [Abr58, Hae67] interchange sub-state populations of hyperfine states to allow the selection of different proton polarization states in the injected target gas [Sto94a, Bra97]. A super conducting magnet [Ste97, Ste95] provides the quantization axis, which is parallel to the positron beam axis. The field is produced by 4 coils, resulting in a non-uniformity of $\frac{\Delta B}{B} = \pm 1.5\%$ along the interaction region axis. The target cell [Ste97, Ste95] increases the target density by two orders of magnitude compared to a free jet. The achieved target thickness is $7 \cdot 10^{13}\,\mathrm{nucl\,cm^{-2}}$. The atoms in the cell are sampled and their polarization measured using a Breit-Rabi type polarimeter (BRP) [Gau92, Bra95, Ste97, Bra97]. A combination of adiabatic RF transitions followed by a sextupole system allows the magnetic sub-state population and thus the polarization of the atoms to be measured [Bra95]. The Target Gas Analyzer (TGA) [Bau96, Bra97] detects count rates of particles mass 1 and 2 which are used to calculate the degree of dissociation of the sample beam.

2.1 The Storage Cell

The storage cell for hydrogen atoms is a straight tube, through which the positron beam of the HERA storage ring passes. The cell has an elliptical cross section of 29 mm width $\times$ 9.8 mm height and an effective length of 400 mm (Fig. 2.1). The polarized atoms are injected through a 10 mm diameter, 100 mm long feed tube into the center of the cell. A 5 mm diameter, 100 mm long sample tube followed by a 10 mm diameter, 120 mm long

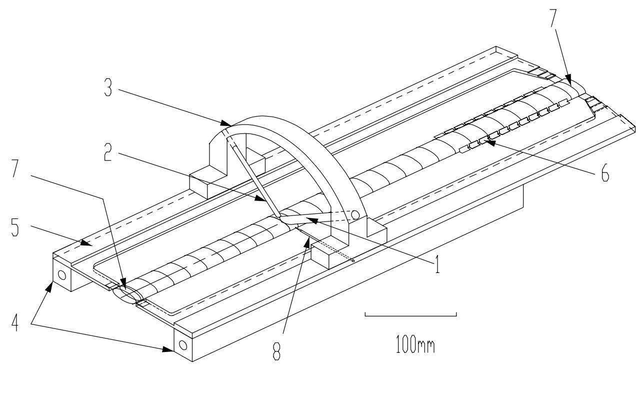

Fig. 2.1:
The HERMES target cell. The various components are as follows: 1) H/D feed tube; 2) Sample tube (extension tube not shown); 3) Target cell and entry tube support arch; 4) Cryogenic cooling and support rails; 5) Support plates; 6) Cell extension with pumping apertures; 7) Cell end support collar; 8) Unpolarized gas feed capillary.

extension tube is used to sample the injected target gas which diffuses out of the tubes into the BRP and TGA. Both tubes are connected to the center of the cell at an angle of 60 degrees from the vertical to avoid direct injection of the atoms from the ABS into the BRP. The extension tube is surrounded by a permanent dipole to maintain a strong magnetic field along the extension tube outside the target magnetic field. During normal operation of the target, the cell is cooled to 100K by a flow of cold helium gas through its support structure, after passing the super conducting magnet. The operating range of the HERMES cell cooling system is 35 K–260 K. The ends of the cell are open and the target gas atoms affect the storage ring vacuum after diffusing out of the cell. A powerful differential pumping system with a total pumping speed of about $9000\,\mathrm{ls}^{-1}$ is installed to minimize their effect. Two molecular turbo pumps, with a combined speed of $4400\,\mathrm{ls}^{-1}$ maintain a pressure in the target chamber of $1.5{\cdot}10^{-7}$ mbar. Three additional pump stations, two upstream and one downstream, reduce the pressure to about $5{\cdot}10^{-9}$ mbar at the entrance to the HERA ring. The cell is coated with Drifilm to inhibit depolarization and recombination of the atomic hydrogen on the cell walls. The operating temperature was chosen at 100K to optimize the density at the minimum of degradation in polarization and recombination.

The cell coating can be damaged by synchrotron radiation, which originates from the positron beam. Therefore, a set of two collimators is installed upstream of the target. The first collimator C1, with minimum vertical and horizontal openings of 2.6 mm and 6.5 mm, respectively, is positioned 2 m upstream from the target and protects against direct synchrotron radiation. The second collimator C2 with with vertical and horizontal openings of 3.0 mm and 8.6 mm, respectively, is located near the cell and protects against secondary scattered radiation. [Her90, Her93]

2.2 The Target Holding Field Magnet

The longitudinal target magnet is designed to operate up to 0.37 T and is a conduction cooled super conducting magnet with a through bore of 250 mm and overall diameter of 348 mm. Four short coils generate the magnetic field. An iron flux return yoke minimizes the stray field at the position of the ABS and the TGA. During operation the remaining

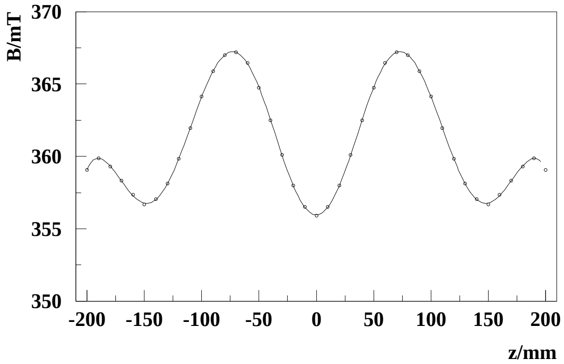

Fig. 2.2:
Plot of the magnetic holding field along the beam axis as a function of z position.

magnetic field outside the yoke near the TGA is 6 mT . The inhomogeneity $\frac{\Delta B_z}{B_z}$ of the magnetic field at positions ±200 mm along the cell is less than ±1.5%, as shown in Fig. 2.2.

2.3 The Polarized Hydrogen Source

The Atomic Beam Source (ABS) [UFun95, Sto94b, Sto94a] is based on the principle of Stern-Gerlach separation of an atomic hydrogen beam. An intense atomic beam is produced by means of RF dissociation and a cooled nozzle for expansion of the atoms into the vacuum. The atoms which pass two subsequent collimators of the differential pumping system form the atomic beam which enters the sextupole separation system (Fig 2.3). The sextupole magnets focus the atoms of the two higher hyperfine levels $|1\rangle$ and $|2\rangle$ with $m_s = +\frac{1}{2}$, while the lower hyperfine levels $|3\rangle$ and $|4\rangle$ are deflected, thus producing an electron polarized beam in the strong field limit. A second set of sextupoles focus the beam into the target cell. The sextupole magnets are azimuthally segmented permanent magnets with a remanent magnetization of 1.25 T. Adiabatic hyperfine transitions are used to interchange the atom state population. During data taking a nuclear polarized beam is injected into the target cell. For testing and calibration purposes additional combinations of spin states can be injected. Table 2.1 gives an overview of the different combinations of injected spin states available at present. The ABS RF dissociator [UFun95] operates at a

ABS transitions	inj. states	P_e	P_z
off	$|1\rangle, |2\rangle$	+1	0
WFT 1–3	$|2\rangle, |3\rangle$	0	-1
SFT 2–4	$|1\rangle, |4\rangle$	0	+1
MFT 2–3, SFT 2–4	$|1\rangle$	+1	+1
MFT 1–3, WFT 1–3	$|2\rangle$	+1	-1
MFT 2–3, WFT 1–3	$|3\rangle$	-1	-1
MFT 1–3, SFT 2–4	$|4\rangle$	-1	+1

Tab. 2.1: Overview of the possible combinations of spin states injected by the ABS. The first row shows the status of the transition units. The second row shows the selection of the hyperfine substates due to the transitions. The third and fourth row show the ideal case of the resulting polarization of the injected states.

frequency of 13.56 MHz with a nominal RF power of 300 W and a hydrogen throughput of 1.25 mbar l s^{-1} with an admixture of 0.14% per volume of oxygen. Both the power and the flow are adjusted to maximize the intensity of the dissociator. The oxygen improves the dissociator output and also results in the formation of ice on the nozzle and on the target cell surface. The nozzle consists of 0.995 aluminum and is cooled to 100±1 K.

The ABS has a powerful four stage differential pumping system with a total pumping speed of more than 15.000 l s^{-1}. The pressure levels for the different chambers during operation are listed in Tab. 2.2. The pressure in the last chamber is in the same order of magnitude as the target chamber pressure. Measurements of the ballistic flow of undissociated hydrogen molecules from the dissociator into the target cell show that only

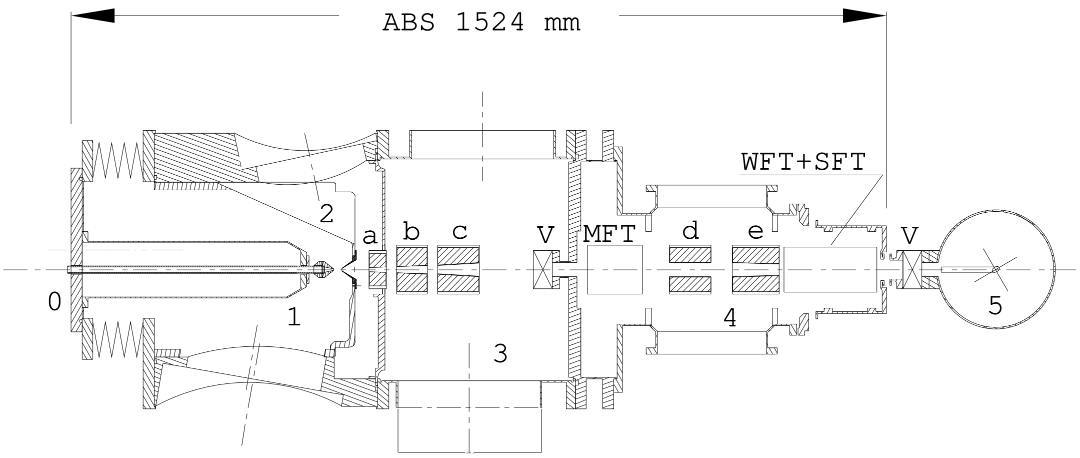

Fig. 2.3: Vertical cut of the HERMES ABS along the atomic beam axis. Indicated are the dissociator(1) on the adjustable dissociator flange (0), the four pump stages (1-4), the target chamber (5), the sixpole magnets (a-e), the RF transitions (MFT, WFT, and SFT), and two separation valves (V).

ABS chamber	pumps	pressure
Dissociator	2×2200 Turbo	$0.9{\cdot}10^{-4}$ mbar
Skimmer	2×1000 Turbo	$1.3{\cdot}10^{-5}$ mbar
1st 6-pole	2200 Turbo, 2500 Cryo	$1.6{\cdot}10^{-6}$ mbar
2nd 6-pole	360 Turbo, 2×1500 Cryo	$2.7{\cdot}10^{-7}$ mbar

Tab. 2.2: ABS chamber pressures during normal operation.

about 1% of the target gas originates from this source, which is unpolarized. The atomic hydrogen flow rate from the ABS, measured before installation using a calibrated compression tube with the same dimensions as the injection tube, was $6.4 \cdot 10^{16}$ atoms s^{-1} for two hyperfine states. This corresponds to a target thickness of $7.0 \cdot 10^{13}$ atoms cm^{-2} at 100 K target cell temperature.

2.4 The Target Gas Analyzer

The average target polarization, as it is seen by the positron beam, includes the polarization of the molecules. Molecules from the recombination of atomic hydrogen as well as unpolarized molecules due to ballistic flow of undissociated hydrogen in the dissociator of the ABS and a fraction of the target chamber gas, which enters the cell, give a contribution to the target density. These contributions need to be measured to avoid systematic uncertainties in the determination of the target polarization. A target gas analyzer (TGA) was developed for the HERMES target and is used to monitor the relative flow rates of atomic and molecular hydrogen through the target cell. A detailed description is given in [Bau96]. The TGA is mounted off axis of the BRP extension tube, at an angle of 7^o, so as not to interfere with the mounting of the Breit-Rabi polarimeter. The atoms and molecules are detected by ionization in a quadrupole mass spectrometer with an open ionizer geometry. A pair of baffles collimate the beam which enters the TGA ensuring that atoms exiting the sample tube cannot strike the metal structure of the ionizer. A schematic is shown in Fig. 2.4. The mass spectrometer was modified so that the ion optics is remote controlled and a channeltron detector is used for single ion detection. The channeltron provides a stable response, which is linear to changes in the emission current of the ionizer. A chopper in between the baffles is needed to subtract the count rate caused by the background gas. The TGA chamber is pumped by a titanium sublimation pump with a pumping speed of $\approx 2000\,\mathrm{l\,s^{-1}}$. The pressure in the TGA chamber during operation is typically $3{\cdot}10^{-9}$ mbar.

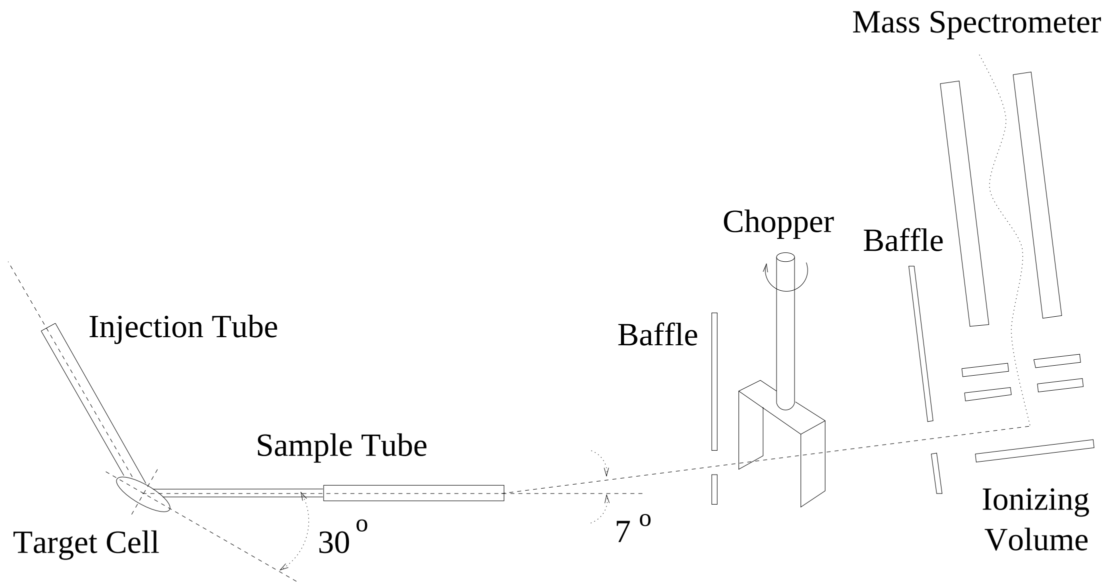

Fig. 2.4: A schematic of the Target Gas Analyzer. The beam leaving the sample tube is chopped and analyzed in a quadrupole mass spectrometer (QMS). The first baffle inhibits gas flow from sources other than the sample tube. The second baffle collimates the beam so that no particles from the beam hit the walls of the ionizing volume.

The contribution of the molecules in a particle sample is expressed in terms of the degree of dissociation α which is defined as the ratio of the number of nucleons in atoms divided by the total number of nucleons in the particle sample. The TGA spectrometer is sensitive to particle densities of the beam in the ionizing volume. These densities depend on the nucleon flow rate through the sample tubes which is again dependent on the total flow rate through the cell. Thus a definition based on nucleon flow rates is only dependent on the recombination inside the cell tubes and the total flow rate through the cell. To obtain the relative flow rates the relative ionization and detection sensitivity of masses 1 and 2 of the TGA needs to be calibrated as well as the temperature dependence of the measured signals. The degree of dissociation and information about the average density of particles inside the cell tubes can then be deduced from the TGA measurements.

2.4.1 Degree of Dissociation

The degree of dissociation $\alpha^{\rm TGA}$ measured by the TGA is defined using the nucleon flow rates $\Phi_{1,2}^{\rm TGA}$ of atoms and molecules which are detected by the TGA:

$$\alpha^{\rm TGA} = \frac{\Phi_1^{\rm TGA}}{\Phi_1^{\rm TGA} + \Phi_2^{\rm TGA}}. \tag{2.1}$$

This value gives information on the degree of dissociation of the particles which have left the sample tubes. The sum of the individual flow rates is proportional to the total flow rate through the cell which is given by the ABS flow rate

$$\Phi_1^{\rm TGA} + \Phi_2^{\rm TGA} = K \cdot \Phi^{\rm ABS}. \tag{2.2}$$

The dependence of $\Phi_{1,2}^{\rm TGA}$ on $\alpha^{\rm TGA}$ and $\Phi^{\rm ABS}$ can be shown in a normalized flow rate diagram. Different values for $\Phi_1^{\rm TGA}$ and $\Phi_2^{\rm TGA}$ at constant ABS flow rate give a straight line with slope -1 for values of $\alpha^{\rm TGA}$ between 0 and 1 [Bau96] (Fig. 2.5). It is obvious

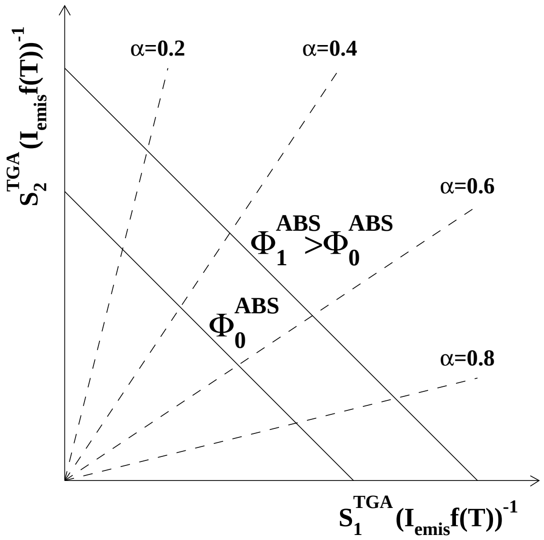

Fig. 2.5: Normalized flow rate diagram for the TGA. A constant ABS flow rate appears in the diagram as a straight line with slope -1 dependent on the degree of dissociation (solid lines). The values for a constant degree of dissociation appear as straight lines for different values of the ABS flow rate (dashed lines).

from the diagram how any error of the measured flow rates $\Phi_{1,2}^{\rm TGA}$ contributes to the error in $\alpha^{\rm TGA}$. In the case $\alpha^{\rm TGA} = 0$ only the error $\Delta\Phi_1^{\rm TGA}$ contributes to $\Delta\alpha^{\rm TGA}$, whereas in the case $\alpha^{\rm TGA} = 1$ only $\Delta\Phi_2^{\rm TGA}$ contributes to $\Delta\alpha^{\rm TGA}$. In the case $\alpha^{\rm TGA} = 0.5$ both errors $\Delta\Phi_{1,2}^{\rm TGA}$ have equal weight. Defining the angle

$$\phi = \frac{\pi}{2}\,\alpha^{\rm TGA}, \tag{2.3}$$

the error on $\alpha^{\rm TGA}$ dependent on $\Delta\Phi_{1,2}^{\rm TGA}$ can be written as

$$\Delta\alpha^{\rm TGA} = \Delta\Phi_1^{\rm TGA}\,\cos\phi + \Delta\Phi_2^{\rm TGA}\,\sin\phi. \tag{2.4}$$

2.4.2 Signals and Flow Rates

The measured signals in the QMS of the TGA are the raw count rates for atomic hydrogen N_1^{TGA} and molecular hydrogen N_2^{TGA}. The signals N^{TGA} include the background count rates, which need to be subtracted, to give the corrected count rates $S_{1,2}^{\mathrm{TGA}}$, which are related to the particles leaving the sample tubes. The data processing is described in Sec. 2.6. The count rates $S_{1,2}^{\mathrm{TGA}}$ can be put in relation to nucleon flow rates $\Phi_{1,2}^{\mathrm{TGA}}$ measured by the TGA and in a second step to the ABS flow rate. This way one can establish the relation between the TGA signals and the definition of α^{TGA} as shown in the previous section and minimize the number of calibration parameters.

The count rates of particles with mass μ in atomic mass units are related to the nucleon flow rates as

$$S_\mu^{\mathrm{TGA}} = \frac{I_{\mathrm{emis}}}{\bar{v}_\mu} \frac{\varepsilon_\mu^{\mathrm{ion}}}{A^{\mathrm{ion}}(\Delta\Omega)} \frac{1}{\mu} \int\limits_{\Delta\Omega} \left(\frac{\partial\Phi_\mu}{\partial\Omega}\right)^{\mathrm{sam}} d\Omega. \tag{2.5}$$

This equation involves the product of the in-going flow rate of particles, the ionizing probability and the detection probability of the particles in the QMS. Here I_{emis} is the emission current of the QMS, $\bar{v}_\mu$ is the velocity of the particles, $A^{\mathrm{ion}}(\Delta\Omega)$ is the surface area of the ionizing volume, $\Delta\Omega$ is the solid angle defined by A^{ion} and the distance from the exit tube , and $(\partial\Phi/\partial\Omega)^{\mathrm{sam}}$ is the angular intensity distribution of particles leaving the sample tubes. The detection probability $\varepsilon^{\mathrm{ion}}$ depends on the ionizing cross section, the transmission probability through the QMS ion optics, and the detection probability in the channeltron. The factor $1/\mu$ accounts for the fact that the QMS detects single ionized particles with mass μ whereas Φ_μ^{TGA} is defined as the nucleon flow rate. The detection probability and the velocity of the particles depend on the mass of the particles. The velocity depends on the temperature of the extension tube as

$$\bar{v} = \sqrt{\frac{8\mathrm{k}T_{\mathrm{ext}}}{\pi m}}, \tag{2.6}$$

also introducing an additional mass dependence. The integral over the intensity distribution in Eq. (2.5) equals the nucleon flow rate Φ_μ^{TGA} and Eq. (2.5) can be written as

$$S_\mu^{\mathrm{TGA}} \propto \frac{I_{\mathrm{emis}}}{\sqrt{\mu T_{\mathrm{ext}}}} \, \Phi_\mu^{\mathrm{TGA}}. \tag{2.7}$$

These equations require calibration constants for signals of mass $\mu = 1, 2$.

An additional relation to the total flow rate Φ^{ABS} reduces the number of calibration constants and is established in the following. If no recombination occurs in the sample tube the particle flow rate Φ^{sam} through the sample tubes is related to the particle density in the center of the cell n^{c} and the conductance C^{sam} of the sample tubes by

$$\Phi_\mu^{\mathrm{sam}} = n_\mu^c \cdot C_\mu^{\mathrm{sam}}. \tag{2.8}$$

The particles injected by the ABS enter the cell as ballistic flow, there is no entrance conductance. In the center the particles start to diffuse, moving as molecular flow according to Eq. (2.8). The flow rate leaving the sample tubes is the ratio of the conductance of the sample tubes $C_{\rm sam}$ and the total conductance of the cell $C_{\rm tot}$ multiplied by the in-going flow rate. The flow rate into the cell equals the sum of flow rates out of the cell. As a consequence the density inside the cell depends on the temperature and the flow rate into the TGA is directly proportional to the ABS flow rate

$$\Phi_\mu^{\rm sam} = \frac{C_\mu^{\rm sam}}{C_\mu^{\rm tot}}\,\Phi^{\rm ABS}. \tag{2.9}$$

This equation is valid independent of recombination inside the target cell. The case of additional recombination inside the sample tube is dicussed in Sec. 3.2. The recombined particles are injected as atoms and detected as molecules, the number of nucleons is conserved. Therefore

$$\Phi^{\rm ABS} \propto \Phi_1^{\rm sam} + \Phi_2^{\rm sam}, \tag{2.10}$$

where $\Phi_1^{\rm sam}$ and $\Phi_2^{\rm sam}$ are, respectively, the nucleon flow rates of atoms and molecules leaving the sample tubes.

The combination of Eqs. (2.7) and (2.10) yields the relation between the ABS flow rate and the TGA count rates $S_\mu^{\rm TGA}$

$$K\cdot\Phi^{\rm ABS} = \frac{1}{I_{\rm emis}\sqrt{T_{\rm ext}}}\left(S_1^{\rm TGA} + \sqrt{2}\kappa\, S_2^{\rm TGA}\right) = \Phi_1^{\rm TGA} + \Phi_2^{\rm TGA}, \tag{2.11}$$

where κ is a relative calibration constant, defined as

$$\kappa = \frac{\varepsilon_1^{\rm ion}}{\varepsilon_2^{\rm ion}}. \tag{2.12}$$

It describes the relative detection probability of mass 2 particles compared to mass 1 particles. The factor $\sqrt{2}$ results from the mass dependence of the velocity (the factor $(1/\mu)$ from Eq. (2.5)). The remaining constants are combined and result in a factor K. Equation (2.8) defines the nucleon flow rates $\Phi_1^{\rm TGA}$ and $\Phi_2^{\rm TGA}$ of atoms and molecules, respectively, independent of the temperature of the sample tubes and the emission current of the QMS. They are directly proportional to the flow rate entering the target cell from the ABS.

2.4.3 Calibration

A change in the degree of dissociation allows a calibration measurement for the constant κ, if the ABS flow rate is constant. In the comparison of two measurements with a different degree of dissociation, the loss in nucleon flow rate of mass 1 must equal the gain in nucleon flow rate mass 2. Therefore the relative sensitivity to masses 1 and 2 can be deduced from the measurements.

The temperature dependence of the recombination is used to arbitrarily change the degree of dissociation. The calibration of the TGA includes the following steps:

- measurement of temperature dependence of TGA signals,
- calculation of TGA flow rates,
- plot of TGA flow rates in flow rate diagram gives fit of constant κ.

A problem which arises here is that the temperature of the extension tube is not measured directly. It may differ from the temperature of the target cell. Due to the constructional constraints the temperature can be calculated from the increase of the sum of the TGA signals from a value measured at a known reference temperature. During normal operation the extension tube has a higher temperature than the sample tube, because it is heated by radiation from the surrounding dipole magnet. The temperature of the sample tube and the cell are the same since both are mounted on the cooling frame. At 300 K (room temperature) the system is in a state of thermal equilibrium and the temperature of the sample and the extension tube are also the same. The TGA signals measured at 300 K can be used as reference signals.

The relation between the TGA count rates and the extension tube temperature is

$$(S_1^{\mathrm{TGA}} + \sqrt{2}\kappa\, S_2^{\mathrm{TGA}})\, I_{\mathrm{emis}}^{-1} \propto \frac{1}{\sqrt{T_{\mathrm{ext}}}}. \tag{2.13}$$

The sum of the count rates divided by the emission current versus the cell temperature is plotted in Fig. 2.6, left. Figure 2.6, right shows the extension tube temperature calculated

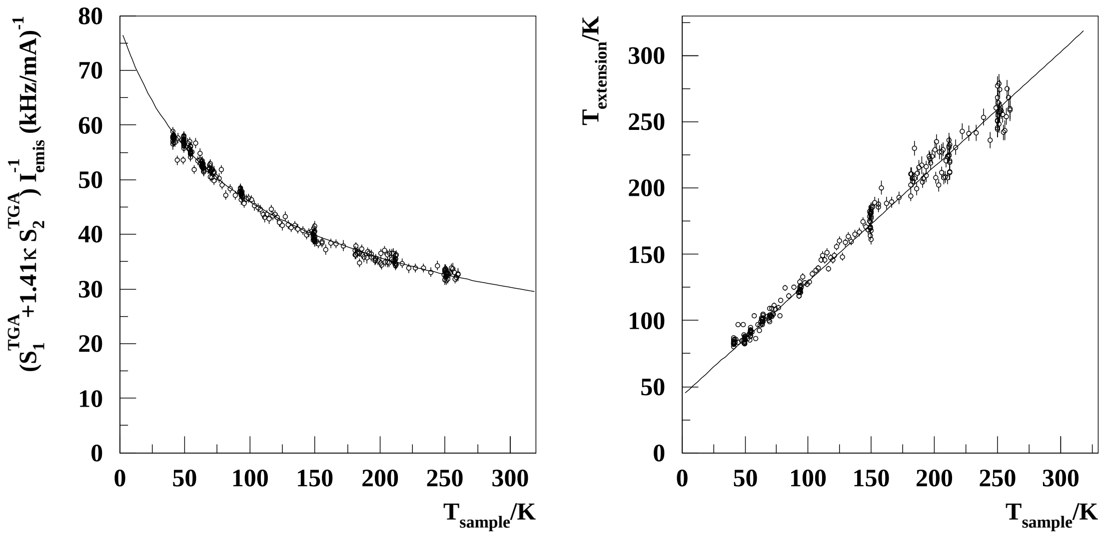

Fig. 2.6: Temperature correction of the TGA corrected count rates.

from the increase in count rate using $T = 300\,\mathrm{K}$ as the temperature of the state of equilibrium. The dependence of the extension tube temperature on the sample tube temperature can be approximated by a function

$$t_{\mathrm{ext}}(T_{\mathrm{sam}}) = t_0 + T_{\mathrm{sam}}\frac{300 - t_0}{300}, \tag{2.14}$$

where t_0 is a constant giving the temperature at the absolute zero for T_{sam}. In Fig. 2.6, right, the function t_0 is fitted to the data with the parameter

$$t_0 = 42.84 \pm 0.7$$

and $\chi^2 = 2.0$. The difference in temperature between the extension tube and the sample tube depends linearly on the sample tube temperature. At T_{sam}=0 K a difference of 50 K in the temperatures is observed. At 300 K the system is in a thermal equilibrium and the temperatures are the same. A plot of the resulting corrected count rates is shown in Fig.2.7 plotted as a flow rate diagram. The slope of a linear function fitted to the data points is -1.28 ± 0.01 resulting in

$$\kappa = 0.552 \pm 0.004. \tag{2.15}$$

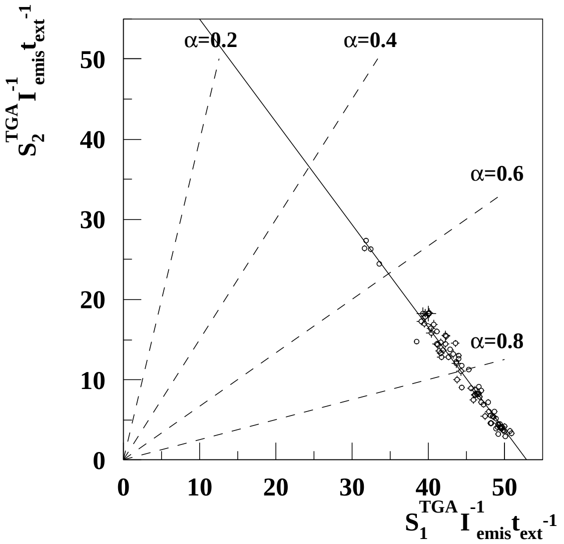

Fig. 2.7: TGA calibration measurement plotted in a normalized flow rate diagram for the TGA flow rates. The change in α_r^{TGA} caused by a change in the cell temperature is used for the calibration.

The constants t_0 determined from the calibration measurements in 1997 are listed in Tab. 2.3.

time	$t_0 \pm \Delta t_0$
10.2	50.97 ± 0.84
84.7	51.67 ± 1.00
118.6	42.70 ± 0.79
122.8	46.01 ± 0.84
168.5	42.84 ± 0.70
194.8	49.62 ± 7.01

Tab. 2.3: Errors of the TGA temperature normalization measurements during the data taking period in 1997. The time is given in days since the start of data taking March 1$^{\mathrm{st}}$, 1997.

An alternative calibration method was available when the HERA beam was accidentally dumped near the target region and the cell coating was damaged. The degree of dissociation measured by the TGA started off at values $\alpha^{\mathrm{TGA}} = 0.2$ and increased slowly within 24 hours. The other target parameters, e.g. temperature, were stable during this time. A plot of the resulting corrected count rates is shown in Fig.2.8 plotted as a flow rate diagram. The slope of a linear function fitted to the data points is $m = -1.362 \pm 0.01$ resulting in

$$\kappa = 0.519 \pm 0.004. \tag{2.16}$$

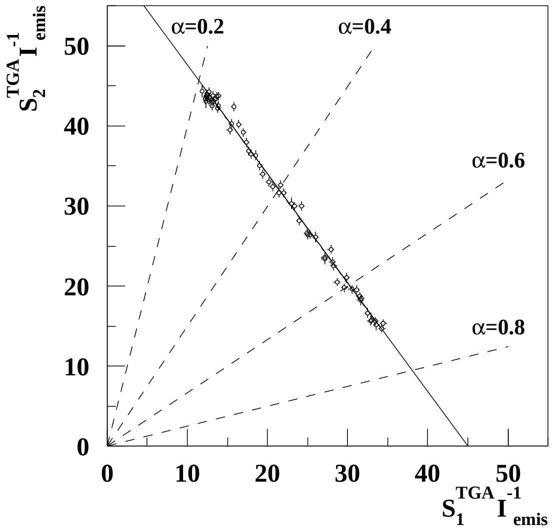

Fig. 2.8: TGA calibration measurement plotted in a flow rate diagram for the TGA corrected count rates. The change in α_r^{TGA} caused by a beam dump near the target is used for the calibration measurement with constant cell temperature. (t = 145 days since Marchst, 1997)

The two calibration measurements were taken with different cells and show an agreement within 6% in the κ value. This difference could be caused by a different mechanical mounting of the extension tube, which needed to be removed during the cell exchange, and may result in a different thermal contact to the environment. On the other hand, a comparison of the different parameters t_0 in Tab. 2.3 does not give evidence for a change in thermal contact from the time period before and after the cell exchange ($t = 145\,\mathrm{d}$).

The calibration in the 1996 running period obtained a value of

$$\kappa = 0.649 \pm 0.006 \tag{2.17}$$

after an accidental beam dump of the HERA positron beam near the target region. The difference in the 1996 and 1997 κ values is due to the maintenance of the TGA during the shutdown 1996/1997, where the hardware of the TGA quadrupole mass spectrometer was optimized.

2.5 The Breit Rabi Polarimeter

The Breit Rabi Polarimeter is located along the axis of the sample tube (Fig.1.3). The particles diffusing from the cell pass the adiabatic hyperfine transitions in the first BRP chamber, where hyperfine state populations can be interchanged. The subsequent sextupole magnet system deflects the two energetically lower hyperfine states $|\,3\,\rangle$ and $|\,4\,\rangle$ with $m_S = -\frac{1}{2}$ (Fig.1.6). The transmission of the states $|\,3\,\rangle$ and $|\,4\,\rangle$ on the axis of the sextupoles is suppressed by a beam blocker. The hyperfine states $|1\rangle$ and $|2\rangle$ are focused into the detector which consists of a chopper, a QMS and a channeltron for single ion detection and counting, similar to the TGA mass spectrometer. A schematic of the setup is shown in Fig. 2.9.

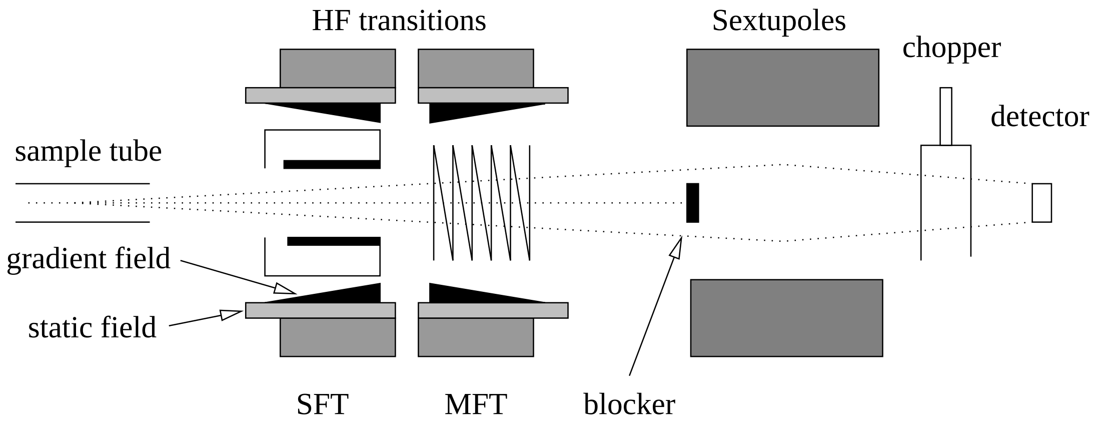

Fig. 2.9: Schematic of the BRP. The RF transition coils are located within the gradient field magnets. The static field magnets are separated C-shaped magnets with coils outside of the chamber vacuum. Four iron plates are mounted inside the chamber to guide the static field inside the transition unit range [Met96]. The particles which leave through the sample tubes enter the RFT units followed by the sixpole system and are detected in a QMS. The beam axis is blocked for the particles to improve the separation in the sextupole magnets.

The vacuum system of the BRP is a differential pumping system which consists of the sextupole chamber and the detector chamber with a total pumping speed of $13000\,\mathrm{l\,s^{-1}}$ (Fig. 2.10). The chamber pressures during operation are listed in Tab. 2.4. The TGA chamber is part of the BRP vacuum system and is located between the target chamber and the sextupole chamber (Fig. 1.3).

BRP chamber	pumps	pressure
(TGA)	$2000\,\mathrm{l\,s^{-1}}$ Ti–Subl.	$3 \cdot 10^{-9}$ mbar
Sextupole	$2\times$ $1500\,\mathrm{l\,s^{-1}}$ Cryo	$2 \cdot 10^{-9}$ mbar
Detector	$10000\,\mathrm{l\,s^{-1}}$ Ti–Subl.	$5 \cdot 10^{-10}$ mbar

Tab. 2.4: BRP and TGA chamber pressures during normal operation.

Each of the two transition units, SFT and MFT can run two different transitions, which requires a change in the setting of static and gradient fields. The frequencies of the RF transitions and the different settings of the magnetic field values and are listed in Tab. 2.5. A comparison of the field values at the working point shows the relation among the static and gradient field for each transition. Due to the tight mounting of the magnets one finds cross talk between the static fields of the SFT and MFT units. The

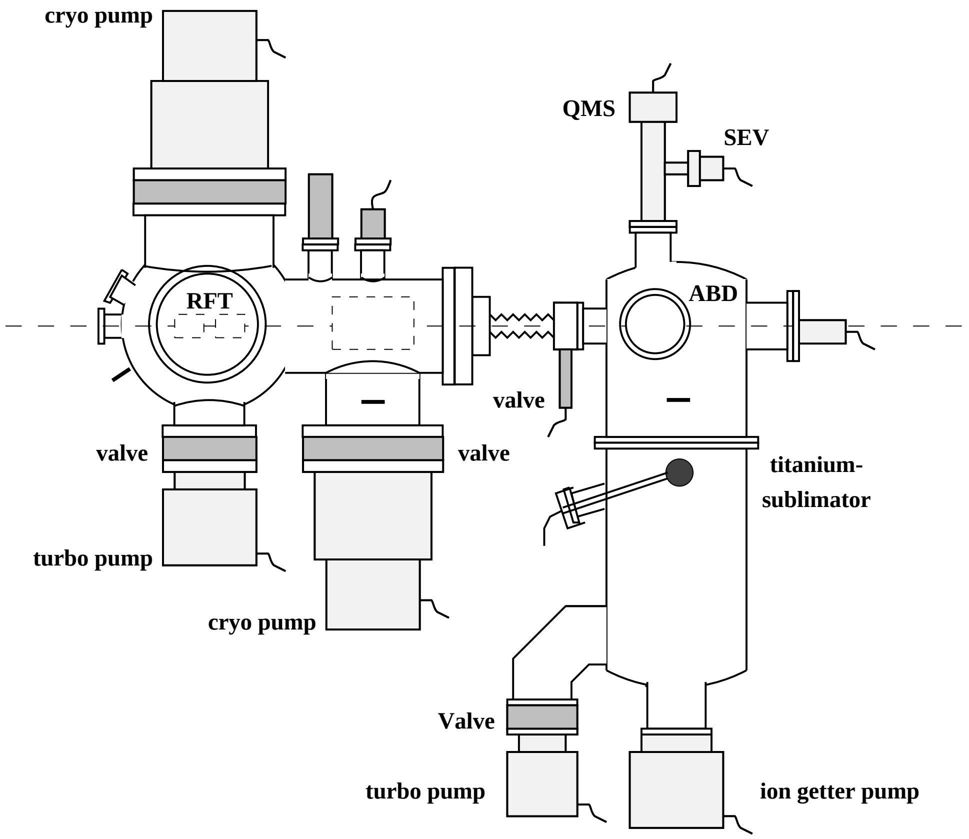

Fig. 2.10: The BRP vacuum system. The adiabatic hyperfine transitions and the sextupole system are located in the sextupole chamber (left). The atomic beam detector (ABD) is located in the detector chamber.

difference in the magnetic field for the different MFT transitions is small enough to have no influence on the SFT transition setting, whereas the big difference in the magnetic field values of the SFT transitions shows a definite influence on the MFT transitions. A different setting of the MFT magnetic field values for the cases of the SFT 1-4 and SFT 2-4 magnetic field values was chosen (Tab. 2.5). If a transition needs to be turned off [1], the amplitude of the RF field should go to zero. In the case of the SFT transitions the power line can be interrupted. In the case of the MFT transitions the power can not be turned off completely, therefore a magnetic field value outside of the resonant field must be set to avoid a transition and provide a quantization axis for the spins of the atoms throughout the BRP. The MFT 1-3 transition, other than the SFT transitions, is a two step transition (1-2) followed by (2-3) [Dre83, Bra95]. The transitions take place at different magnetic field values, hence at different positions inside the transition unit. Depending on the gradient of the magnetic field inside the MFT unit either one or both transitions are effective inside the MFT unit. In the first case the field value can be

[1] In the following 'transition off' means the power of the transition unit is turned off, 'transition on' means the power of the transition unit is turned on.

transition, (resonance)	v/MHz	B/mT	U^{stat}/V	U^{grad}/V	ε_j
SFT 1-4	1465	31	-0.03	3.0	$\varepsilon_{\mathrm{s14}}$
MFT 1-3, (1-2)	90	68	0.70	5.5	$\varepsilon_{\mathrm{m13r12cs14}}$
MFT 1-3, (2-3)	90	60	0.70	5.5	$\varepsilon_{\mathrm{m13r12cs14}}$
MFT 2-3, (1-2)	—	—	—	—	$\varepsilon_{\mathrm{m13r12cs14}}$
MFT 2-3, (2-3)	90	60	0.71	4.0	$\varepsilon_{\mathrm{m13r23cs14}}$
SFT 2-4	1465	128	1.03	5.0	$\varepsilon_{\mathrm{s24}}$
MFT 1-3, (1-2)	90	68	0.70	5.5	$\varepsilon_{\mathrm{m23r12cs24}}$
MFT 1-3, (2-3)	90	60	0.70	5.5	$\varepsilon_{\mathrm{m23r23cs24}}$
MFT 2-3, (1-2)	—	—	—	—	$\varepsilon_{\mathrm{m23r12cs24}}$
MFT 2-3, (2-3)	90	60	0.75	3.5	$\varepsilon_{\mathrm{m23r23cs24}}$
MFT off	—	—	0.56	3.5	—

Tab. 2.5: The frequencies and magnetic field values of the BRP RF transitions. The values of the voltage which is proportional to the magnet current are shown for the static and gradient field. The MFT off field is set outside a resonance. The definition of the efficiencies of the transitions are shown in the last column.

chosen to operate the (2-3) transition only, in the second case the direction of the gradient needs to be chosen so that both transitions appear inside the unit and in the order (1-2) followed by (2-3) [Dre83, Bra95]. The Resonance MFT 1-2 interchanges between states which are both in the acceptance of the detector and is not useful for the measurement of the polarization.

The measurement of the polarization is carried out as a sequence of measurements with different hyperfine transitions switched on, which change the signals measured in the detector dependent on the initial occupation of the hyperfine states. A measurement of the electron and proton polarizations of the atoms for a single ABS state requires a minimum of four beam measurements with different transitions on or transitions off. Transitions available in the BRP are the medium and strong field transitions MFT 1-3, MFT 2-3, SFT 1-4, and SFT 2-4. The resulting different polarization measurements allow a cross check during the experiment. The efficiencies of the transitions ε_j and the transmission probabilities σ_i of the states $|\, i\,\rangle$ through the sextupole system enter into the calculation of the polarization and also need to be known. The definition of the efficiencies is shown in Tab. 2.5, where the subscript e.g. of the efficiency $\varepsilon_{\mathrm{m13r23cs14}}$ denotes the efficiency of the resonance (2-3) of the transition MFT 2-3 with the SFT 1-4 magnetic field set in parallel. For a single polarization measurement a number of 10 efficiencies and additional transmission probabilities is involved. Because this number exceeds the number of measured signals a calibration measurement of the efficiencies and transmission probabilities is needed.

2.5.1 Theory of Polarization Measurement

The effect of a transition on the occupation of the hyperfine states will be shown for the SFT 1-4 transition. Switching on the RF power of the SFT 1-4 transition interchanges states $|1\rangle$ and $|4\rangle$ and in the ideal case of fully efficient transitions[2] and equal transmission probabilities for states $|1\rangle$ and $|2\rangle$ through the sextupoles the influence of the BRP transition on the atomic beam can be described by

$$\begin{pmatrix} n_1 \\ n_2 \\ n_3 \\ n_4 \end{pmatrix} \xrightarrow{|1\rangle \leftrightarrow |4\rangle} \begin{pmatrix} n_4 \\ n_2 \\ n_3 \\ n_1 \end{pmatrix} \xrightarrow{\text{sextupole}} \begin{pmatrix} n_4 \\ n_2 \\ 0 \\ 0 \end{pmatrix}, \tag{2.18}$$

where the n_i are the occupation numbers of the states $|i\rangle$. The signal I_{s14} in the detector then is the sum $I_{s14} \propto n_4 + n_2$. The ratio of the detector signals for one of the above transitions turned on and the signal without transition ($I_{\text{off}} \propto n_1 + n_2$) can be written as

$$R_{ij} = 1 - \frac{n_i + n_j}{n_1 + n_2}. \tag{2.19}$$

The additional normalization $\sum_i n_i = 1$ leads to a system of linear equations which, in the case of the transitions MFT 2-3, SFT 1-4, and SFT 2-4, can be written in the form

$$\begin{pmatrix} 1 & 1 & 1 & 0 \\ -R_{14} & 1-R_{14} & 0 & 1 \\ 1-R_{24} & -R_{24} & 0 & 1 \\ 1-R_{23} & -R_{23} & 1 & 0 \end{pmatrix} \begin{pmatrix} n_1 \\ n_2 \\ n_3 \\ n_4 \end{pmatrix} = \begin{pmatrix} 1 \\ 0 \\ 0 \\ 0 \end{pmatrix}, \tag{2.20}$$

where the first row represents the normalization. The system can be solved for n_i and any combination of the three transitions.

In the case of non-ideal efficiencies ε_{ji} of the transition $(i-j)$ and transmission probabilities σ_i Eq. (2.18) has to be modified

$$\begin{pmatrix} n_1 \\ n_2 \\ n_3 \\ n_4 \end{pmatrix} \xrightarrow{|1\rangle \leftrightarrow |4\rangle} \begin{pmatrix} (1-\varepsilon_{s14})\, n_1 + \varepsilon_{s14} n_4 \\ n_2 \\ n_3 \\ \varepsilon_{s14} n_1 + (1-\varepsilon_{s14})\, n_4 \end{pmatrix} \xrightarrow{\text{sextupole}} \begin{pmatrix} \sigma_1 \left[(1-\varepsilon_{s14})\, n_1 + \varepsilon_{s14} n_4\right] \\ \sigma_2\, n_2 \\ 0 \\ 0 \end{pmatrix}. \tag{2.21}$$

Due to the beam blocker inside the sextupole magnets the transmission probabilities σ_3 and σ_4 can be set to zero. The signal I_{s14} in the detector in this case is given by the sum

$$I_{s14} \propto \sigma_1 \left[(1-\varepsilon_{s14})\, n_1 + \varepsilon_{s14} n_4\right] + \sigma_2\, n_2. \tag{2.22}$$

[2] In the case of the MFT 2-3, (1-2) resonance this leads to $\varepsilon_{m13r12} = 0$.

In the non ideal case the calculation of all occupation numbers in Eq.(2.20) depends e.g. on the efficiencies $\varepsilon_{\mathrm{s14}}$, $\varepsilon_{\mathrm{s24}}$, $\varepsilon_{\mathrm{m13r13cs14}}$, $\varepsilon_{\mathrm{m13r23cs14}}$, and their products. The efficiency $\varepsilon_{\mathrm{m13r13cs14}}$ appears because the medium field transition (1-3) is a two step transition, (1-2) followed by (2-3). The exact calculation is given in detail in Ref. [Bra95]. This system is solved for n_i if the efficiencies and transmission probabilities are known. The polarization values are calculated using Eq. 1.14.

2.5.2 Calibration, Error Calculation

The efficiencies and transmission probabilities are parameters of the calculation of the polarization which need to be calibrated. From Tab. 2.5 it is apparent that a number of 10 efficiencies, two SFT and 2×4MFT efficiencies, have to be measured. The number of remaining transmission probabilities σ_1 and σ_2 from Sec. 2.5.1 can be reduced by setting $\sigma_1 = 1$ and $\tilde{\sigma} = \sigma_2/\sigma_1$, which then needs to be measured. The number of unknown parameters for a measurement with a single ABS state is larger than the number of measured beam signals. A combination of measurements with different ABS states gives a larger number of measured signals than calibration constants. In the following the calculation is shown based on a single ABS state for simplicity.

The calibration measurements include the hyperfine occupation numbers of the beam entering the BRP as unknown parameters n_i, $\sum_i n_i = 1$, which are related to the intensities N_i by the normalization

$$n_i = \frac{N_i}{\sum\limits_i N_i}. \tag{2.23}$$

The Equation (2.22) can be written as

$$I_{\mathrm{s14}} = (1 - \varepsilon_{14})\, N_1 + \tilde{\sigma}\, N_2 + \varepsilon_{14} N_4, \tag{2.24}$$

forming one row of a matrix equation $I = M \cdot N$. The vector I contains beam signals from the respective combinations of BRP transitions 'on' and 'off' for a given ABS operation mode

$$\begin{pmatrix} I_{\mathrm{off}} \\ I_{\mathrm{s14}} \\ I_{\mathrm{s24}} \\ \vdots \end{pmatrix} = \begin{pmatrix} 1 & \tilde{\sigma} & 0 & 0 \\ (1-\varepsilon_{14}) & \tilde{\sigma} & 0 & \varepsilon_{14} \\ 1 & \tilde{\sigma}\,(1-\varepsilon_{24}) & 0 & \varepsilon_{24} \\ \vdots & \vdots & \vdots & \vdots \end{pmatrix} \cdot \begin{pmatrix} N_1 \\ N_2 \\ N_3 \\ N_4 \end{pmatrix}. \tag{2.25}$$

In a given ABS operation mode the parameters N_i are constant. The definition of the beam signals and efficiencies of the RF transitions of the BRP are listed in Tabs. A.1.

Equation (2.25), expressed as a vector of functions of the unknown parameters $x = (N_i, \varepsilon_j, \tilde{\sigma})$, can be written as

$$f(x) = M \cdot N - I = \mathbf{0}. \tag{2.26}$$

The function f can be expanded in a Taylor series and since all unknown parameters appear in f in first order only, the calculation yields

$$f_k(x) = f_k(x^{(0)}) + \sum_l \frac{\partial f_k}{\partial x_l}(x_l - x_l^{(0)}) + O^2(x_l). \tag{2.27}$$

Defining the matrix $D_{lk} = \partial f_k / \partial x_l$, Eq. (2.27) can be solved for the unknown parameters assuming $O^2(x_l) \approx 0$

$$x = x^{(0)} - (D^t D)^{-1} D^t \, f(x^{(0)}), \tag{2.28}$$

where $(D^t D)^{-1} D^t$ is the pseudo inverse of D. The beam signals I_k measured by the BRP have uncertainties $(\sigma_I)_k$. Eq. (2.28) can be solved iteratively by the least square fit method. The uncertainties $(\sigma_I)_k$ are weight factors on the beam signals I_k described by the matrix G_I, which is defined as the inverse of the covariance matrix of the beam signals C_I

$$G_I = C_I^{-1} = \begin{pmatrix} \ddots & & 0 \\ & (\sigma_I)_k^2 & \\ 0 & & \ddots \end{pmatrix}^{-1} . \tag{2.29}$$

This diagonal form of the covariance matrix is caused by the independence of the beam signals I_k. Equation (2.28) needs to be modified for the iteration process and the error weight and yields for the $(n+1)^{\mathrm{th}}$ step

$$x^{(n+1)} = x^{(n)} - (D^t G_I D)^{-1} D^t G_I \, f(x^{(n)}). \tag{2.30}$$

The χ^2 value is defined by

$$\chi_n^2 = \left| \, G_I \cdot f(x^{(n)}) \, \right|^2 \tag{2.31}$$

and minimized in the iteration process. The covariance matrix of the fit parameters C_x gives the uncertainties $(\sigma_N)_i$ and $(\sigma_\varepsilon)_j$ and the correlations between the parameters x_i, x_j, $i \neq j$

$$C_x = (D^t G_I D)^{-1}. \tag{2.32}$$

This system is underdetermined. In addition, the parameter $\tilde{\sigma}$ cannot be separated from the parameter N_2. A combination of measurements with different ABS operation modes allows the separation because of the variations in N_2.

In the case of different combined ABS modes any additional measurement increases the number of unknown parameters by four N_i, but also increases the number of components of I_k by 11. There are a total of seven different ABS modes available (Tab. 2.1), which leads to a maximum of 77 beam signals I_k compared to a maximum of 39 unknown parameters x_l. The system is overdetermined and can be solved. A measurement of all ABS modes and BRP states is complex and not appropriate for the data acquisition in the HERMES experiment. It is carried out during the time inbetween HERA fills.

During run of the experiment we use the results for the efficiencies ε_j and their errors $(\sigma_\varepsilon)_j$ from the procedure described above as an input to the standard measurements, assuming that the efficiencies are stable in time. This data replaces most of the unknown parameters, leaving only the signals N_i as such. Eq. (2.25) can then be reduced to a measurement of each BRP transition with one ABS state and be rewritten as

$$N = (M^t G_I M)^{-1} M^t G_I \cdot I = R \cdot I. \tag{2.33}$$

The dependence of the beam signals N_i on the beam signals I_k defines the statistical error of the measurement. It is given by the covariance matrix

$$C_N^{\mathrm{stat}} = R C_I R^t. \tag{2.34}$$

The systematic error of the measurement is defined by the dependence of the beam signals N_i on the efficiencies ε_j. By defining the matrix $D_{(I,\varepsilon)} = \frac{\partial I_k}{\partial \varepsilon_j}$ and using Eq. (2.33) the dependence of the beam signals on the efficiencies is

$$\frac{\mathrm{d}N_i}{\mathrm{d}\,\varepsilon_j} = \sum_k \frac{\partial N_i}{\partial I_k} \frac{\partial I_k}{\partial \varepsilon_j} = R_{ik} D_{(I,\varepsilon)\,kj} \tag{2.35}$$

and the systematic error is given by the covariance matrix

$$C_N^{\mathrm{sys}} = R D_{(I,\varepsilon)} C_\varepsilon D^t_{(I,\varepsilon)} R^t. \tag{2.36}$$

This formalism also allows calculation of the values of the occupation numbers and the polarization, including the errors. The covariance matrix for the normalized occupation numbers Eq. (2.23) is calculated by using the dependence of

$$\frac{\mathrm{d}n_i}{\mathrm{d}N_k} = \frac{\delta_{i,k} \cdot (\sum_l N_l) - N_i}{(\sum_l N_l)^2} = X_{i,k} \tag{2.37}$$

and yields

$$C_n = X C_N X^t \tag{2.38}$$

for the statistical and systematic errors. The uncertainty on the polarization is calculated using the polarization vector (Eq. (2.1))

$$P = \begin{pmatrix} P_e \\ P_n \end{pmatrix} = S \cdot n \tag{2.39}$$

for the electron polarization P_e and proton polarization P_n, where

$$S = \begin{pmatrix} 1 & \cos 2\theta & -1 & -\cos 2\theta \\ 1 & \cos 2\theta & -1 & -\cos 2\theta \end{pmatrix} \tag{2.40}$$

includes the magnetic field dependence of the states $|\,2\,\rangle$ and $|\,4\,\rangle$, and yields the covariance matrix for the statistical and systematic error

$$C_p = S C_n S^t. \tag{2.41}$$

Since a single ABS state allows a measurement of five BRP transitions with only four unknown parameters N_i, the system is overdetermined and can be solved for the online measurements. The values for the efficiencies and errors are listed in Tab. A.2.

2.6 Data Acquisition

The data acquisition at HERMES is split into the online system, which records the raw data and the offline system, which organizes the data for online monitoring and analysis. The offline system is based on a client/server model called DAD[3] [Wan95] developed at HERMES which is an extension of the ADAMO[4] [Fis93] data base system developed at CERN. The system operates on unix type computers and allows communication between different servers via the Internet. The server generates table entries for the acquired data which can be accessed by the clients. The communication between clients and different servers allows access and exchange of information acquired at different parts of the experiment. The table entries are marked with the time the data was taken which allows identification of valid data for online monitoring and subsequent analysis. In addition PINK [MFun95] an interface between ADAMO, DAD and the script language Tcl/Tk was developed by the HERMES group. It builds a basis for the clients to connect to the server and therefore provides an interface for online monitoring and experiment control. An overview over the client/server model is shown in Fig. 2.11.

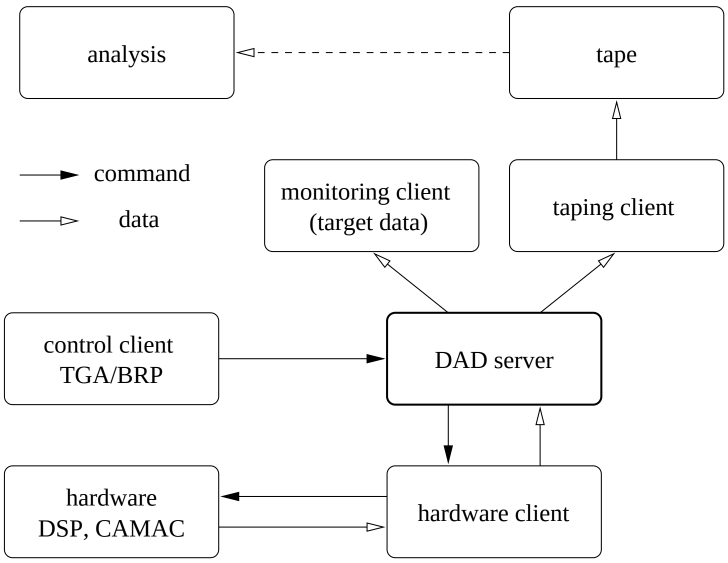

Fig. 2.11: Control and data flow structure of the HERMES target.

Additional relevant target data such as the chamber pressures and ABS information also need to be put in relation to the TGA/BRP data. The data acquisition of the target data can be divided into three items and will be discussed in the following sections:

- Signal Processing TGA/BRP. The count rates in the TGA and BRP are detected and a first separation of beam signal and background takes place in the digital signal processor (DSP/MSI).

- Measurement control, data flow. The control data for the TGA and BRP are generated by the TGA/BRP control client and server. The measured data is transferred

[3] **DAD** **D**istributed **A**damo **D**atabase

[4] **ADAMO** **A**LEPH **DA**ta **MO**del, an entity relationship based database.

from the DSP/MSI to the server where the calculation of the polarization values takes place. The results are transfered to the online monitoring systems and the taping client.

- Data Analysis. The relevant target data is collected according to its time information and averaged over one TGA/BRP event (Sec.B). The data is stored in ntuples as target events for further analysis and quality control.

2.6.1 Signal Processing

The TGA and BRP measurements are based on the detection of atomic and molecular beams with low flow rates. Due to the low intensities of the signals of beam and background the use of a QMS and a channeltron for single ion counting is required. Count rates for the background and the sum of beam and background are measured and subtracted. The beam is chopped by a fork shaped chopper with a rotation frequency of 5.5 Hz controlled by a current stabilized power supply. The signals of the channeltron and the chopper trigger are read into a digital signal processor (DSP/MSI) and analyzed (Fig. 2.12). The DSP/MSI builds up histograms for every combination of transitions of

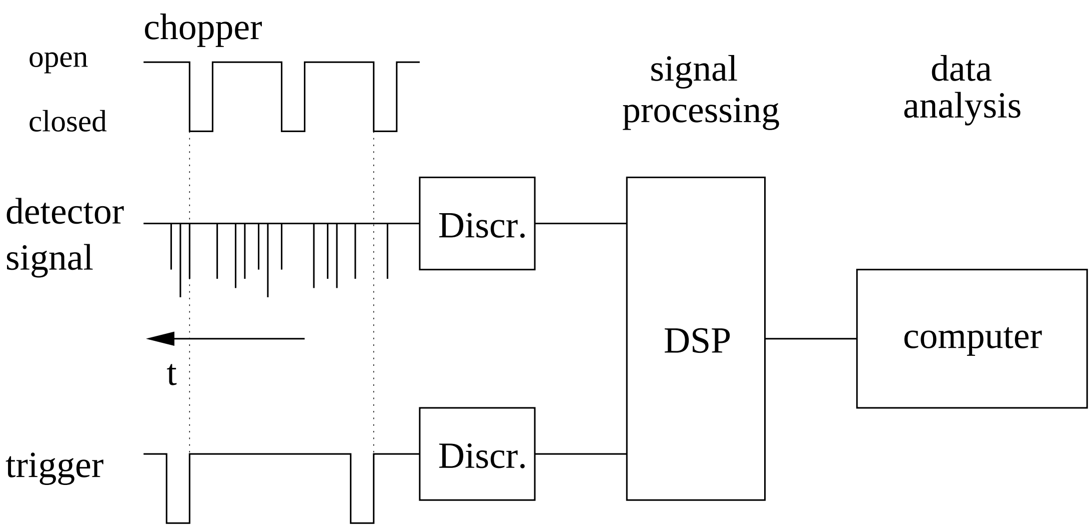

Fig. 2.12: Signal processing of the TGA and BRP count rates. The channeltron and trigger signals are discriminated and acquired by the DSP/MSI. The DSP/MSI separates the beam signal and background count rates and is read out by th computer. The trigger signal is generated by the chopper and is in phase with the chopper position.

the ABS and BRP included in the present measurement (Sec. 2.6.2). Every bin in the histograms accumulates the detected counts within a certain time interval (time resolved spectrum (TRC)). The start is generated by a trigger pulse which is in phase with the chopper position (Fig. 2.13). The bin length of the histograms are adjusted to the chopper frequency, which is measured. The window positions for chopper open and chopper closed are shown in Fig. 2.12 on top of a normalized TRC spectrum, where the contents of every bin is normalized to a time interval of one second. The data accumulated in the windows A and B is integrated and subtracted, therefore the count rates for beam and background are separated. The data in between the two windows A and B is assigned to

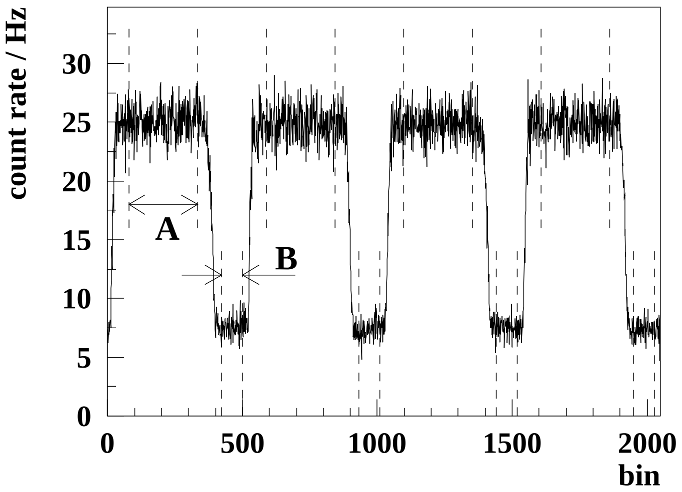

Fig. 2.13: TRC spectrum with the chopper windows for the BRP signal. The indicated area A includes the accepted count rates of the sum of beam and background. The indicated area B includes the accepted count rates for the background only.

an undefined chopper position and ignored. Typical values for the count rates of TGA and BRP during normal operation of the target are listed in Table 2.6.

amu	TGA beam	TGA background
1	17 kHz	75 kHz
2	1 kHz	350 kHz
18	0 kHz	7 kHz
amu	BRP beam	BRP background
1	17.5 kHz	7.5 kHz
2	1 kHz	38 kHz
18	1.6 kHz	52 kHz

Tab. 2.6: Typical count rates for beam signal and background of masses 1, 2, and 18 in the TGA and BRP.

2.6.2 Measurement Control, Data Flow

A BRP polarization measurement is based on the measurement of the mass 1 beam signals of a combination of four different BRP transitions. The TGA/BRP client generates a list of commands which is sent via the server to the DSP/MSI and CAMAC units which control the QMS and the settings of the adiabatic transition units of the BRP. For every BRP transition the beam signals are measured and transfered to the TGA/BRP server. All different BRP and ABS transitions needed for a measurement of the polarization states of the experiment define a measurement cycle (TGA/BRP event). The server calculates the polarization and the degree of dissociation from the count rates measured in one cycle and transfers the data to the online monitoring system and the taping client. Additional corrections which need to be applied to the beam measurements are also calculated by the TGA/BRP server. A portion of the mass 1 beam count rates comes from the dissociative ionization of molecular hydrogen. The count rates must be corrected accordingly. This correction is based on a calibration measurement where the mass 1 beam signal (S_1) dependent on the mass 2 (S_2) or mass 18 (S_{18}) beam signals was measured. The corrected beam mass 1 S_1^c is given by

$$S_1^c = S_1 - k_2\, S_2 - k_{18}\, S_{18}, \tag{2.42}$$

where the constants k_2 and k_{18}, respectively, give the proportion of the beam signals of mass 2 and 18 to the beam signal mass 1. The factors measured for TGA and BRP are listed in Tab. 2.7. Due to a missing mass 18 signal in the TGA the signal is not corrected for a mass 18 contribution.

Device	k_2	k_{18}
TGA	0.0116 ± 0.0010	–
BRP	0.0100 ± 0.0010	0.1142 ± 0.0017

Tab. 2.7: Correction factors for the corrected beam signal in TGA and BRP.

Table 2.8 shows the different modes of measurement of the TGA/BRP server. All measurements for the TGA and BRP are based on a sequence of beam signal measurements for masses 1,2, and 18 which allows simultaneous measurements of the TGA and BRP. The sequence of the transition units in the higher level measurements can be randomized

Measurement	Symbol	Acquired Data / Analysis
beam	bm	single beam signal
corr. H_1 beam	hcb	3×'bm', amu=1,2,18 / k_2, k_{18}, S_1^c
α^{TGA}	hmf	'hcb' / degree of dissociation
P^{BRP}	hp	4×'hcb' / polarization based on 4 RFT states
P^{BRP}	hpx	5×'hcb' / 4×polarization based on 5 RFT states
α^{TGA} run mode	rhm	2×'hmf' / 2×degr. of diss. for 2 ABS states $P_z^{\pm}$
P^{BRP} run mode	rhx	2×'hpx' / 2×polarization for 2 ABS states $P_z^{\pm}$
α^{TGA} standby	ahm	3×'hmf' / 3×degr. of diss. for 3 ABS states $P_z^{\pm}, P_e$
P^{BRP} standby	ahx	3×'hpx' / 3×polarization for 3 ABS states $P_z^{\pm}, P_e$
α^{TGA} bhabha	ehm	2×'hmf' / 2×deg. of diss. for 2 ABS states $P_e^{\pm}$, $P_e^{\mp}$
P^{BRP} bhabha	ehx	2×'hpx' / 2×polarization for 2 ABS states $P_e^{\pm}$, $P_n^{\mp}$

Tab. 2.8: The TGA/BRP measurement modes.

to avoid systematic errors. The length of a measurement can be adjusted and is restricted to multiples of a 'hcb' measurement. For the HERMES experiment a number of four 'hcb' measurements was chosen. The measurement time for a 'rhx' measurement under these conditions is 120 s resulting in a spin flipping time of 60 s.

2.6.3 Data Analysis

Further analysis on the target data, e.g. the correction of the beam count rates, includes additional information such as the emission current of the QMS. The additional data is taken by the CAMAC systems on a different time basis and needs to be adapted to the BRP/TGA event times. The TGA and BRP data collected during one TGA/BRP event represent the average values of the target polarization and degree of dissociation during this time period. The additional data is collected at times within this period and is averaged over one TGA/BRP event and stored in PAW-ntuples[5] as a target event. A

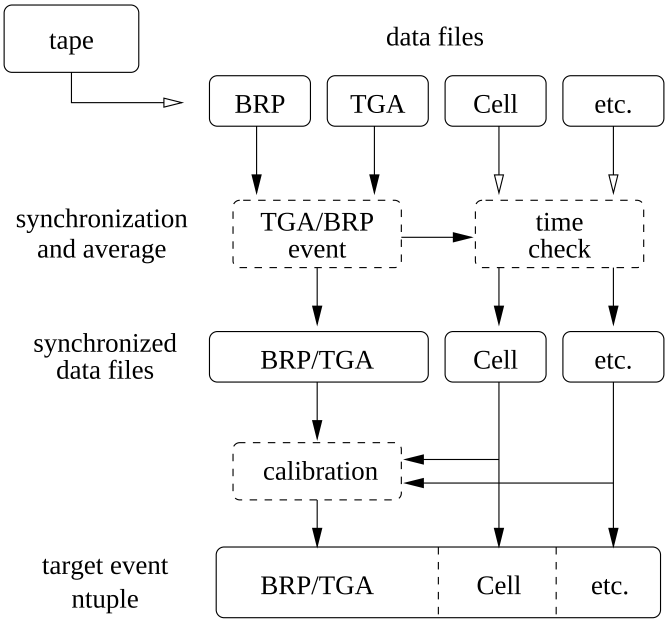

Fig. 2.14: Production of the target event ntuple. In a first step the data of the additional devices are synchronized to the TGA/BRP event time interval and averaged. In a second step the information is then used to calculate the corrections and calibrations. In a last step the data is stored in a ntuple as a single target event.

schematic of the data production is shown in Fig. 2.14. The calculations carried out during the ntuple production are the re-calibration and calculation of the BRP polarization which depends on the target magnetic field. Important calculations based on the ntuples are the emission current correction of the beams signals and the background correction for the TGA flow rates (Sec. 7). which depends on the target chamber pressures. Table B.1 in App. B shows an overview of the most important values related to the target analysis which are included in the ntuples.

[5]Physics Analysis Workstation, developed at CERN

3 Molecular Flow in Tubes

The internal target technique uses an atomic beam which is injected into a target cell to increase the density in comparison to a free jet beam. The density which can be achieved by this technique is low enough for the atoms inside the cell to be within the molecular flow regime. The atoms undergo a certain number of wall collisions before they leave the cell. A sample is detected and analyzed by the BRP and the TGA. The polarization P and degree of dissociation α of the atoms depend on the interaction with the walls, where the recombination and most of the relaxation processes occur. At each and every position P and α depend on the history of each atom. An understanding of the motion of atoms inside the cell tubes gives information about differences between the measured values in the TGA and BRP and the averaged values inside the cell. The atoms, which leave the sample tubes for the analysis of P and α have experienced a different history compared to the atoms inside the cell, which form the target of the experiment. The goal, besides understanding the motion of atoms inside cell tubes, is to develop a tool for further calculations related to recombination and relaxation processes based on the knowledge of the age distributions.

The recombination and relaxation processes discussed in the present work include a functional dependence on the number b of wall collisions of the form $W(b) = (1-\gamma)^b$, where $\gamma \leq 1$ is the recombination or relaxation probability per wall collision and b is the wall collision age of the atom (see Braun [Bra90]). The function $W(b)$ describes the dependenc of e.g. the polarization $P(b)$ on the wall collision number

$$P(b) = P(0)W(b) = P(0)\exp\left(b\ln(1-\gamma_p)\right). \tag{3.1}$$

The polarization of a sample of atoms with wall collision ages b given by a normalized distribution $A(b)$ is then, in the case of $\gamma_p \ll 1$, given by

$$P = \int_0^\infty P(0)A(b)\exp(-\gamma_p b)db. \tag{3.2}$$

Thus, assuming the same relaxation constant γ for each wall collision, the knowledge about γ and the age distributions A(b) allows the calculation of the final polarization of the atoms in the sample.

The age distributions result from Monte-Carlo simulations [Bau96] of the motion of the atom inside the cell. The input for the simulations are the cell geometry and a $\cos\theta$ distribution for the emission angles of the atoms leaving the cell surface. The atoms are traced through the cell and histograms (age distributions) are updated when a atom passes by certain positions. Age distributions are taken at the z-positions along the beam tube axis and of atoms leaving all tubes. In addition, age distributions of atoms accepted by the detectors of TGA and BRP are generated.

3.1 Age Distributions

The motion of a particle, either atom or molecule, inside the cell and its escape from the cell is described by models of diffusion and ballistic flow. The basic situation is shown in Fig. 3.1. The beam is injected into the center of the cell as ballistic flow and the particles start to diffuse. At a certain point they reach the end of the cell and escape.

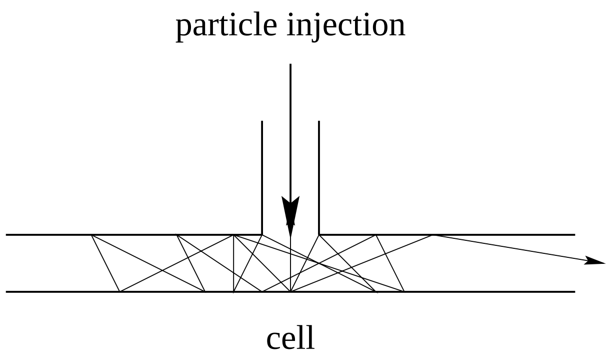

Fig. 3.1:
Motion of particles inside the cell. The particles are injected in the center and move towards the openings where they escape.

The diffusion model in this case is based on the random walk of the particles inside the tube along the tube axis (z direction). Every time the particle hits the wall there is an equal probability for it to go an average distance λ to the left or to the right. The average distance in this case is comparable to the cell dimensions. The resulting density distribution is described by the diffusion equation

$$D(z_0, z, b) = \frac{1}{\sqrt{\pi\, 2\lambda^2 b}} \exp\left(-\frac{(z_0 - z)^2}{2\lambda^2 b}\right), \tag{3.3}$$

which gives the probability of finding the particle at the position z starting at point $z = z_0$ in the center of the cell after b wall collisions. Here the mean free path length λ is the average distance in z per wall collision. It is defined by the geometry of the tube and the angular distribution of the emission angle of the particle, in this case a $\cos\theta$ distribution. The function $D(z_0, z, b)$, centered at $z = z_0$, gives the z-distribution of the particles with a certain age b inside an infinitely long tube.

The difference between the distribution $D(z_0, z, b)$ and the distribution of the particles in a finite tube like the cell tube is the loss of particles at the cell ends. After the particles have left the cell they do not add to the density inside the cell any more, whereas in the case of the infinitely long tube the particles always have a probability to move back to the origin. The density distribution inside the cell tube due to a particle injection into the center of the cell has a triangular shape, which follows from the relation between the flow rate Φ and the conductance C of the cell

$$\Phi = n_c C, \tag{3.4}$$

where n_c is the density in the center and C is the conductance from the center to the cell ends, which is given by

$$C \propto \frac{S^2 U^{-1}}{l + \frac{16}{3} S U^{-1}}, \tag{3.5}$$

where S is the surface area of the tube opening and U is the circumference of the tube of length l. Equation (3.5) can be written as $C \propto l'^{-1}$ where $l' = l + \frac{16}{3} SU^{-1}$ is the effective length of the cell. The condition which can be derived from Eq. (3.5) and which must be fulfilled by the density distribution is $\tilde{n}(z = l') = 0$. The function $D(0, z, b)$ has to be modified to obtain this condition.

A first approach to describe the loss of particles is the following: The diffusion of particles inside a tube is the same in positive and negative direction of z. The function which describes how particles, that start at the position z in an infinitely long tube diffuse in positive z direction also describes the diffusion of particles, that start from this particular position in negative z direction. Thus, images $D(\pm l', z, b)$ of the original function $D(0, z, b)$ which are centered at $\pm 2l'$ with the opposite sign describe the loss of the particles inside the cell (Fig.3.2). The sum of two of those functions is a solution for

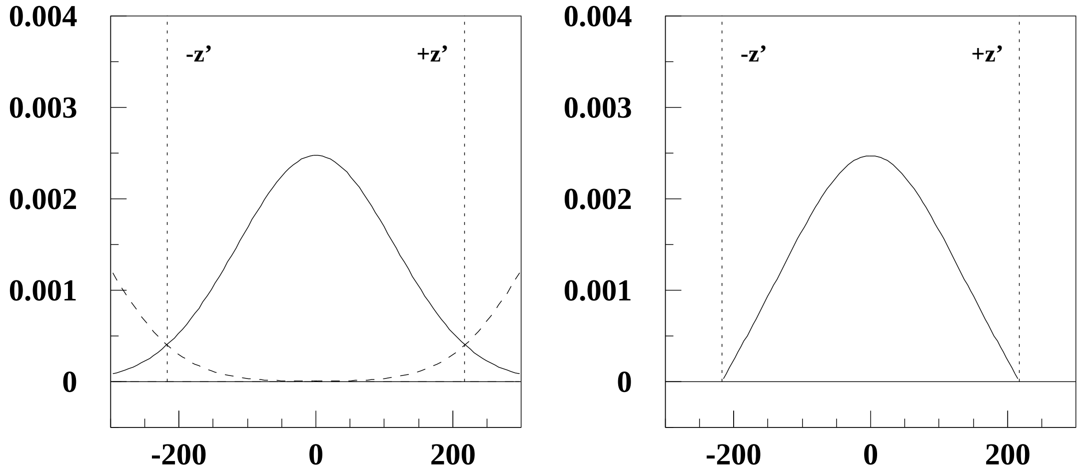

Fig. 3.2:
The solid line in the left figure represents the distribution $D(0, l', b)$ of particles along the cell axis. The distribution of missing particles due to the loss at the cell ends is described by the dashed line which represents the functions $D(2l', z, b)$ and $D(-2l', z, b)$. The right figure shows the difference $D(0, z, b) - D(2l', z, b)$ inside the range $[-l', +l']$ which fulfills the condition described in the text.

the condition $D(0, l', b) - D(2l', l', b) = 0$ at either end of the cell. Any additional function $D(2il', z, b)$, $i = 1, 2, ...$, has a similar overlap at the other end and needs to be corrected, too. This process leads to an infinite sum for the final function describing the density distribution

$$\tilde{D}(z, b) = D(0, z, b) + \sum_{i=1}^{\infty} (-1)^i \left[D(-2il', z, b) + D(+2il', z, b) \right], \tag{3.6}$$

where $\tilde{D}(z,b)$ is a solution of the diffusion equation and the total number of particles is conserved. The following relation is satisfied expressing the loss of particles from the cell:

$$\int_{-\frac{L}{2}}^{+\frac{L}{2}} \tilde{D}(z,b+1)\,dz < \int_{-\frac{L}{2}}^{+\frac{L}{2}} \tilde{D}(z,b)\,dz, \tag{3.7}$$

where L is the total lenght of the cell. The sum of the distributions $\tilde{D}(z,b+1)$ for all ages results in the total target density distribution $n(z)$.

In the model of ballistic escape of a particle from the cell, the ballistic flow is characterized by an average path length between two wall collisions, which is large compared to the cell dimensions. Although the particles diffuse along the cell, as described by the previous model, they have a certain probability to leave the cell directly after every wall collision and at any position z. For most of these cases the path length of the particles is not close to the average path length λ. This is described by the following model: A particle trapped in a certain volume with an opening has a certain probability to leave after every wall collision, which is the inverse of N_0, the average number of wall collisions the particle experiences within that volume. Starting with a number $B(0)$ of particles, the collision age dependenc of the number B is

$$B(b) = B(0)\,\exp\left(-\frac{b}{N_0}\right). \tag{3.8}$$

The combination of the models above give a simple description of the density distribution in an open cell which is the product of a diffusive term which describes the diffusion along the tube and a ballistic term which describes the particle escape. The number density $N(b,z)$ of particles with a wall collisions age b depends on the z-position as

$$N(z,b) = c_0\,\tilde{D}(z,b)\,\exp\left(-\frac{b}{N_0}\right). \tag{3.9}$$

The density distribution $n(z)$ results in

$$n(z) = n_0 \int_0^{\infty} c_0\,\tilde{D}(z,b)\,\exp\left(-\frac{b}{N_0}\right)\,db, \tag{3.10}$$

where n_0 is the average density inside the cell, c_0 is a normalization constant and N_0 is the constant accounting for the loss of particles through ballistic flow. A comparison of the function from Eq. (3.9), a sum over the first 50 terms, with data from a Monte-Carlo simulation is shown in Fig. 3.3. The plots show data for particle ages of $b = 50$ and $b = 500$ wall collisions. The lines are functions fitted to the data with the parameters listed in Tab. 3.1,i. The value l' is fitted to the data and is close to the expected value of $l' = 217.5\,\mathrm{mm}$ calculated from Eq. (3.5). In Figure 3.4 the function $N(z,b)$ is shown in comparison to Monte-Carlo data for fixed values of z. In this case $N(z,b)$ describes the age distribution of the particles dependent on the position inside the cell. The behavior of

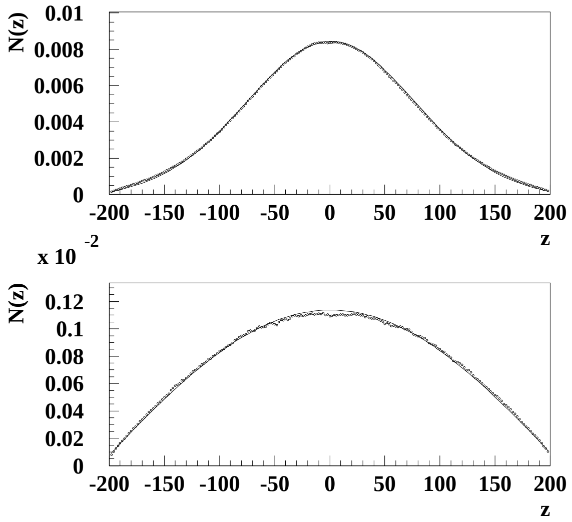

Fig. 3.3:
Comparison of the function N(z,b) from Eq. (3.9) (solid lines) to results from a Monte-Carlo simulation (data points) at fixed values for b. The upper picture shows the z distribution of particles with 50 wall collisions, the lower picture shows the distribution of particles with 500 wall collisions.

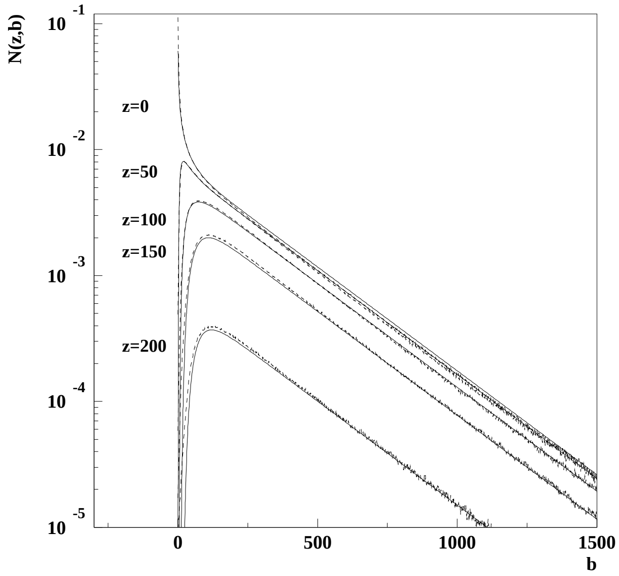

Fig. 3.4:
Comparison of the function N(z,b) from Eq. (3.9) (solid lines) to results from a Monte-Carlo simulation (dashed lines) at fixed values for z. The distributions for different positions are shown using the parameters given in the text.

$N(z,b)$ at a low number of wall collisions ($b < 130$) is clearly dominated by the diffusion process. At a high number of wall collisions the particles are spread over the cell and the behavior of $N(z,b)$ can be described as an exponential decay independent of the position. This exponential decay at a high number of wall collisions is mostly caused by the function $\tilde{D}(z,b)$ and the exponential term with exponent N_0 describes the minority of the particles, which leave the cell due to their high emission angle ($\theta \approx \pi/4$) from the surface. The functions $N(z,b)$ are used in the following to calculate the degree of dissociation and polarization of the particles, which remain inside the cell dependent on their position z.

Further calculations of the degree of dissociation and polarization of the atoms, which leave the cell is also of interest. These calculations involve e.g. an integration of the age distributions over the wall collision age and can be simplified if the infinite sum in the function $\tilde{D}$ is reduced. It will be shown in the following that the age distributions of the atoms, which remain inside the cell or leave the cell can be approximated by a function of the form

$$A_e(b) = c_1\,(D(z_0, z, b) + c_2)\,\exp\left(-\frac{b}{N_0}\right), \tag{3.11}$$

given by $D(z_0, z, b)$ from Eq. (3.3) and the exponential from Eq. (3.8) describing the diffusive and ballistic behavior of the particles. The parameter c_1 is a normalization factor and c_2 gives the relation between the diffusive and ballistic flow rate. The function $A(b)$ is a useful quantity proportional to the outgoing flow rate, because it represents both characteristics of the behavior of the function N(b) through a diffusive and a ballistic term. Because of the use of the $D(b)$ instead of $\tilde{D}(b)$ the z dependence cannot be reproduced. The age distributions, which result from the Monte-Carlo calculations for the escaped particles, are fitted by the function $A(b)$ with parameters N_0,λ,c_1, and c_2 for a given z, where N_0 and λ are now different from the ones used in Eq. (3.9).

Atoms leaving the cell pass the exit opening of the tube. The age distribution $A_e(b)$[6] for those atoms therefore involves the function $D(0, L/2, b)$, where $L/2$ corresponds to the cell end. A plot of the simulated age distribution for atoms leaving the beam tube into the target chamber is shown in Fig. 3.5. The function $A_e(0, L/2, b)$, which corresponds to Eq. (3.11) is plotted on top of the data points. The parameters used for the function are listed in Tab. 3.1,ii.

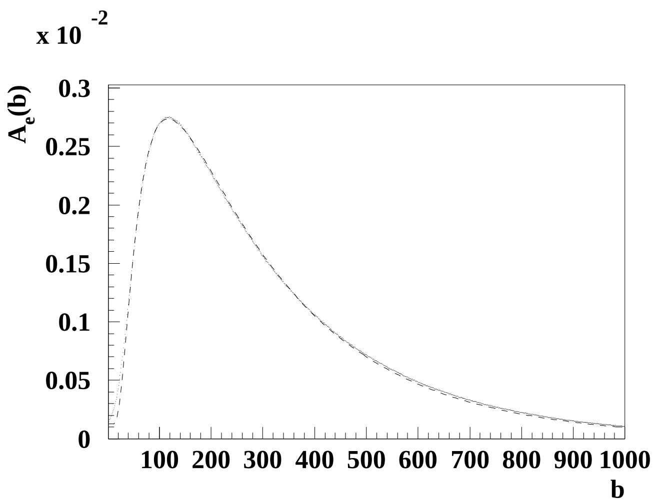

Fig. 3.5:
Comparison of simulated and calculated age distribution of atoms escaping from the cell. The function $A_e(b)$ (dashed line) is plotted on top of the Monte-Carlo data (points).

The age distribution of atoms, which remain in the cell $A_c(b)$[7] results from integration of the distribution $A_e(0, L/2, b)$, which gives information about the number of atoms leaving the cell at an age b and is the derivative of $A_c(b)$. Thus it is given by the integral

$$A_c(b) = \int_b^\infty A_e(0, \tfrac{L}{2}, b)\,db. \tag{3.12}$$

[6]The subscript 'e' stands for 'escape'.
[7]The subscript 'c' stands for 'cell'.

The result of the integration of $A_c(b)$ can be approximated by a function of the analytical form $A_e(0, L/2, b)$. In Fig. 3.6 the age distribution of the remaining atoms inside the cell is shown and compared to a function of the form $A_e(0, L/2, b)$ with the parameters listed in Tab. 3.1,iii.

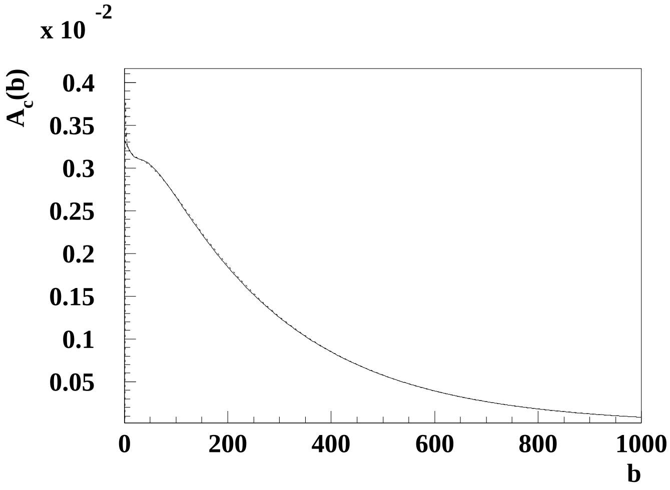

Fig. 3.6:
Comparison of simulated and calculated age distributions of atoms remaining in the target cell. The function $A_c(b)$ (dashed line) is plotted on top of the Monte-Carlo data (points)

The functions introduced in this section are approximations, starting from simplified concepts of physics, they are analytic expressions which describe the motion of particles inside the cell tubes as obtained from the Monte-Carlo calculation. A comparison amongst the age distributions of Figs. 3.4 to 3.6 reveals that the atoms inside the cell mainly show diffusive behavior. The atoms need about $b \approx 130$ wall collisions until they are spread over the cell tube and start to diffuse out of the cell ends. Consequently, the z distribution of young and old atoms is different (Fig. 3.4). Since the distributions of atoms with low ages show a strong dependence on the position z inside the cell, a case of high γ_r and γ_p (Eqs. (3.1)) and (3.2) leads to a dependence of α and P on the position.

3.2 Calculation of the Degree of Dissociation

The recombination process removes atoms from a sample. If it is the only process removing atoms, it can be described as

$$N_a(b, \gamma_r) = N(0)\,(1 - \gamma_r)^b, \tag{3.13}$$

where $N(0)$ is the initial number of atoms in the sample ($b = 0$), γ_r is the recombination probability per wall collision, and $N_a(b, \gamma_r)$ is the number of atoms remaining in the sample after b wall collisions. The atoms, which leave the sample tubes, have an age distribution $A_e(b) = N(b, 0)$. The effect of recombination on the number of atoms leaving the sample tubes is, in the case of a small recombination probability per wall bounce, described by

$$A_e^r(b) = A_e(b)\, \exp(-\gamma_r b). \tag{3.14}$$

The degree of dissociation α^{TGA}, measured by the TGA, depends on γ_r and can be defined using number densities of nucleons in atoms $\tilde{n}_1$ and in molecules $\tilde{n}_2$, which have left the sample tubes

$$\tilde{n}_1 = \int_0^\infty A_e^r(b)\,db, \quad \tilde{n} = \tilde{n}_1 + \tilde{n}_2 = \int_0^\infty A_e(b)\,db, \tag{3.15}$$

and the degree of dissociation expressed in number densities is

$$\alpha^{\mathrm{TGA}} = \frac{\tilde{n}_1}{\tilde{n}_1 + \tilde{n}_2} = \frac{\int_0^\infty A_e^r(b)\,db}{\int_0^\infty A_e(b)\,db}. \tag{3.16}$$

An integration of the function $A_e(b)$ (Eq. (3.11)) yields

$$\begin{aligned} \int_0^\infty A_e(b)\,db &= \frac{c_1 c_2}{N_0^{-1}} + c_1 \left(2\lambda^2 N_0^{-1}\right)^{-\frac{1}{2}} \exp\left(-\frac{2z^2 N_0^{-1}}{\lambda^2}\right), \\ &\stackrel{\text{def}}{=} B'(N_0^{-1}) + D'(N_0^{-1}). \end{aligned} \tag{3.17}$$

The integration of the function $A_e^r(b)$ is similar to $A_e(b)$, the exponent N_0^{-1} in $A_e(b)$ is replaced by $(N_0^{-1} + \gamma_r)$, and Eq. (3.16) leads to the following expression for α^{TGA}:

$$\alpha^{\mathrm{TGA}} = \frac{B'(N_0^{-1} + \gamma_r) + D'(N_0^{-1} + \gamma_r)}{B'(N_0^{-1}) + D'(N_0^{-1})}. \tag{3.18}$$

This function for α^{TGA} depends on the geometry of the cell and on the acceptance solid angle of the TGA. Due to the angle of 7^o between the TGA detector and the tube axis, the atoms which are detected originate mostly from diffusive flow. The result of a MC simulation for the age distribution of the atoms in the TGA is shown in Figure 3.7. The corresponding age distribution from Eq. (3.11) is plotted on top of the data using the parameters listed in Tab. 3.1,iv. The comparison shows, that this function is a useful approximation for a fraction of the sample, which leaves the sample tubes.

The functions A_e and A_e^r are also approximations for the density distribution inside the cell tube, but with different parameters. Thus the calculation of the degree of dissociation inside the cell tube α^T is analogous to the calculation of α^{TGA}. A difference appears in the calculation because the density of the nucleons inside the cell changes due to the recombination process. The molecules are slower compared to the atoms and the nucleons which recombined to molecules have a factor of $\sqrt{2}$ higher density. Equations (3.15) to (3.18) have to be modified accordingly.

3.3 Calculation of the Polarization

The depolarization of the atoms during the contact with the wall is correspondingly described by an exponential decay dependent on a relaxation time τ_{wc}

$$P(t) = P(0)\exp(-\frac{t_s}{\tau_{wc}}). \tag{3.19}$$

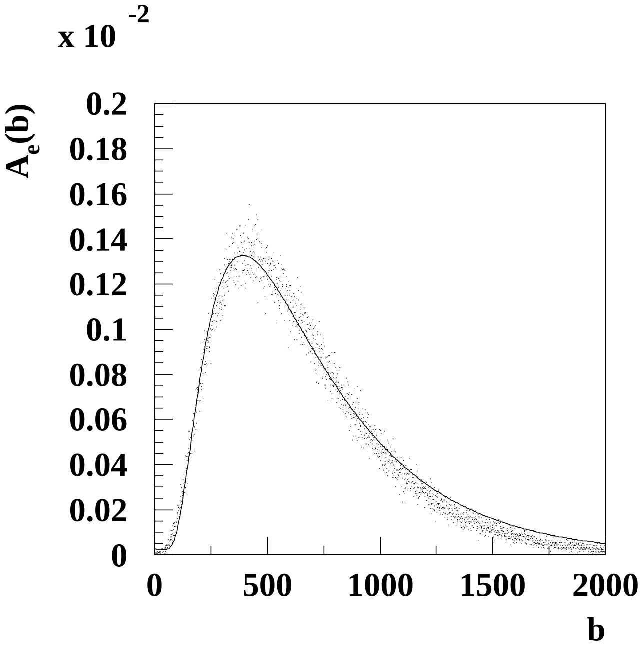

Fig. 3.7: Plot of the age distribution for the atoms detected by the TGA from Monte-Carlo studies. The solid line represents the function $A_e(b)$ from Eq. (3.11).

The dwell times t_s are distributed as $d(t_s) = \exp(-t_s/\tau_s)$ with an average dwell time of $\langle t_s \rangle = \tau_s$. The polarization of a sample of atoms after a single wall collision is a function of the average dwell time τ_s and can be calculated by folding the two expressions, resulting in

$$P(\tau_s) = P(0)\frac{1}{\tau_s}\int\limits_0^\infty \exp\left(-\frac{t_s}{\tau_{wc}} - \frac{t_s}{\tau_s}\right)\, dt_s = P(0)\frac{\tau_{wc}}{\tau_{wc}+\tau_s}. \tag{3.20}$$

and the polarization $P(b)$ after a number of wall collisions b is

$$P(b) = P(0)\left(\frac{\tau_{wc}}{\tau_{wc}+\tau_s}\right)^b = P(0)\left(1 - \frac{\tau_s}{\tau_{wc}+\tau_s}\right)^b. \tag{3.21}$$

Thus, the expression $\frac{\tau_s}{\tau_{wc}+\tau_s}$ is the polarization relaxation probability γ_p per wall collision. Therefore, polarization as a function of collision number $P(b)$, for $\gamma_p \ll 1$, is

$$P(b) \approx P(0)\exp\left(-\frac{\tau_s}{\tau_{wc}+\tau_s}\, b\right) = P(0)\exp(-\gamma_p b). \tag{3.22}$$

The effect on the polarization of the atoms, which are detected by the BRP, can now be written similar to Eq. (3.14) including the effect due to recombination:

$$A_e^p(b) = P(b)A_e^r(b) = P(0)A_e^r(b)\, \exp(-\gamma_p b). \tag{3.23}$$

The age distributions are weight functions to the polarization $P(b)$. For the polarization measured by the BRP one obtains

$$P^{\mathrm{BRP}} = P(0)\frac{\int_0^\infty A_e^p(b)\, db}{\int_0^\infty A_e^r(b)\, db}, \tag{3.24}$$

where the functions used here are again of the same form of Eq. (3.18) yielding

$$P^{\mathrm{BRP}} = P(0)\frac{B'(N_0^{-1}+\gamma_r+\gamma_p)+D'(N_0^{-1}+\gamma_r+\gamma_p)}{B'(N_0^{-1}+\gamma_r)+D'(N_0^{-1}+\gamma_r)}. \tag{3.25}$$

This expression includes the age distribution of the respective sample of atoms, the loss due to recombination, and the polarizations loss due to wall collisions. For the calculation of the polarization of the atoms inside the cell the analytic form of Eq. (3.25) can be used by replacing the age distributions only. As opposed to the calculation of the degree of dissociation inside the cell the molecules do not contribute to this calculation.

The atoms detected by the BRP are expected to have a smaller number of wall collisions, since the BRP is located on the axis of the sample tube. Due to the additional beam blocker in the center, the angular acceptance of the detected atoms is approximately in the interval $[0.5^o, 2.5^o]$. The result of a Monte-Carlo simulation for the atoms detected by the BRP is plotted in Fig. 3.8. The age distribution $A_e(b)$ for the BRP is plotted on top of

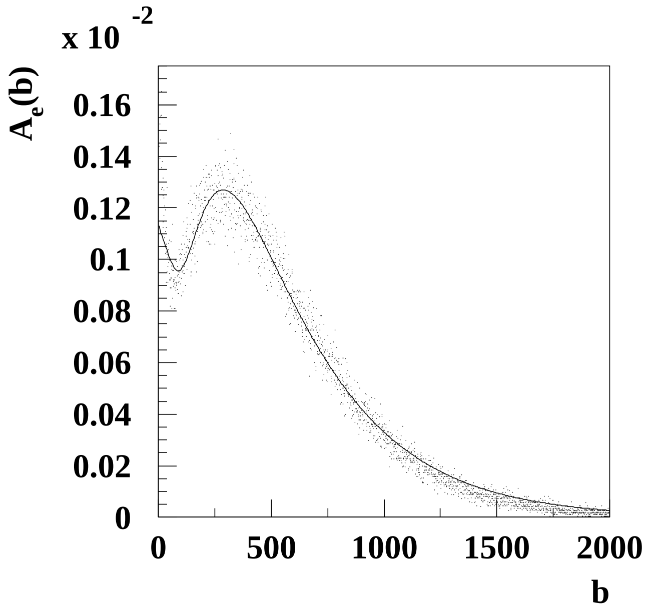

Fig. 3.8: Plot of the age distribution of atoms detected by the BRP based on Monte-Carlo studies. The solid line represents the function $A_e(b)$ from Eq. (3.11).

the data using the parameters listed in Tab. 3.1,v. The function and the age distribution are nearly identical. The fitted value for λ corresponds with the fit value for the TGA sample, the constant c_2 increases significantly by two orders of magnitudes compared to the TGA due to the big contribution of ballistic atoms.

3.4 Parameters of the Age Distributions

The parameters obtained from the fit to the Monte-Carlo results are listed in Tab 3.1. The function $N(b)$ is only determined by the cell geometry and the average path length of the atoms inside the cell. The difference between the fit parameter in the function $N(b)$ and the value resulting from the Monte-Carlo simulations, $\lambda_{\mathrm{MC}} = 11.1$, is $\approx 3\%$.

	Fig.	$N(b)$	z	$2l'$	λ	N_0	c_0		$\langle b\rangle$
i	3.3	b=50	200	421	10.8	1800	1.65		50
		b=50	200	421	10.8	1800	1.65		500
	Fig.	$A_e(b)$	z	$2l'$	λ	N_0	c_1	c_2	$\langle b\rangle$
ii	3.5	escape from cell tube	200	421	13.7	295	3.6	$1.3{\cdot}10^{-4}$	323
iii	3.6	remain in cell	200	421	15.0	264	0.52	$3.3{\cdot}10^{-3}$	268
iv	3.7	detected by TGA	220	468	6.4	396	5.1	$3.5{\cdot}10^{-5}$	658
v	3.8	detected by BRP	220	468	6.6	370	3.1	$1.1{\cdot}10^{-3}$	508

Tab. 3.1: Parameters of the age distributions $N(z,b)$ from Eq. (3.9) (i) and $A_e(b)$ from Eq. (3.11) (ii-v) used for analysis of the degree of dissociation and the polarization of the atoms. The parameter z is given by the cell geometry and the parameters l', λ and N_0 are fit parameters. The parameter $\langle b\rangle$ results from the Monte-Carlo simulations.

The function $\tilde{D}(b)$ in $N(b)$, which describes the diffusion of the atoms, behaves like an exponential function for ages larger than the average wall collision age (Fig. 3.3). The additional exponential function describes the loss due to ballistic flow which is very small compared to the diffusion.

The quantities N_0 of the functions $N(b)$ and $A_e(b)$ cannot be compared. The function $A_e(b)$ is an approximation for the functional dependence of $N(b)$ on b. The exponent N_0^{-1} in $A_e(b)$ cannot be interpreted as the average wall collision age of all the atoms, because it represents the average wall collision age of the fraction of atoms, which show a ballistic behavior in the age distributions. The average number of wall collisions of all atoms $\langle b\rangle$ is also listed in Tab. 3.1 for comparison.

4 Recombination inside the Storage Cell

There is no online measurement of the polarization of the molecules at the HERMES target, thus the understanding of the recombination of hydrogen atoms inside the target cell plays an important role in understanding the averaged target polarization. Several types of cell coatings were studied in the past [Bra95, Pri93a, Pri93b] with respect to the degree of recombination . The goal for the HERMES experiment was to maintain high polarization and low recombination inside the target cell. The intense beam current in the HERA electron ring leads to changes and damage of the cell surface, which gives an additional restriction on the choice of the surface material.

First measurements of the polarization of the molecules were performed by HERMES and NIKHEF [Vdb97]. The measurements, however, were taken under non standard conditions, such as low degree of dissociation α and temperatures close to room temperature. The results need to be extrapolated to the HERMES working point of high α and low target temperature of 100 K. A change in cell temperature might lead to a change in the sample correction for the TGA measurements and to a change in the initial polarization of the recombined atoms. A study of the temperature dependence of recombination inside the target cell is needed to understand the conditions inside the cell.

The first section gives an introduction to the theory of surface adsorption and recombination based on a rate model in which the recombination occurs via the collision of an gaseous atom with an atom adsorbed on the surface. The temperature dependence of the rate of recombination is discussed in the case of Langmuir adsorption of the adsorbed hydrogen atom on two different types of sites, which are identified by the respective binding energies as chemisorption and physisorption of the atoms. The bond to the surface is approximated by a three dimensional harmonic oscillator.

An additional steady state condition for the recombination and desorption rates of atoms from the surface allows the calculation of dwell times of the atoms on the surface. At the end of the chapter measurements of the degree of dissociation on a clean and on a water coated cell surface are presented, which allow the determination of the recombination coefficients and the binding energies on the two different types of sites. The desorption and recombination rates of the different types of sites can be derived from the fitted parameters and are used in the following chapters to study the spin relaxation (Chap. 5) and the polarization of the molecules (Chap. 7).

The possible interaction of the beam with the surface of the cell and the resulting corrections are discussed at the end of this chapter. The values of the degree of dissociation measured by the TGA and those inside the cell are put in relation to each other by analyzing the respective age distributions.

4.1 Theory of Recombination

There have been many experimental investigations of the temperature dependence of the rate coefficient for atomic recombination on solid surfaces. An overview is given in the article by Wise and Wood [Wis67]. Two kinds of mechanisms have been proposed for atomic recombination on surfaces. The first one, the Eley-Rideal mechanism (E-R) postulates the direct reaction of an atom adsorbed on the surface (SX), with an atom from the gas phase (X):

$$SX + X \leftrightarrow S + X_2. \tag{4.1}$$

The other, the Langmuir-Hinshelwood mechanism (L-H), involves surface recombination of two adsorbed atoms (adatoms):

$$2SX \leftrightarrow 2S + X_2. \tag{4.2}$$

In our investigation we follow the work of Gelb and Kim [Gel71], where the postulated mechanism for recombination is, that the reaction occurs via the collision of a gas atom with an atom adsorbed on the surface (the E-R mechanism). The L-H mechanism is neglected in this model.

The rate of recombination R in number of atoms per unit surface area is

$$R = 2M_s\theta Z \tag{4.3}$$

where M_s is the number of binding sites per unit surface area, θ is the coverage of the sites by adsorbed atoms, and Z is the reactive flux of gaseous atoms per adatom. The reactive flux is defined as the flux of those atoms incident on the surface, which lead to the recombination of a gaseous atom with an adatom. To understand how the recombination rate, which is measured in the experiment, depends on the environment, such as temperature and surface material, it is therefore necessary to understand the adsorption of atoms on the surface and the processes which enable recombination.

The adsorption of atoms on the surface is a dynamic process. If the atoms strike the surface most of them stay there for a while until they, because of Boltzmanns law, happen to have enough energy to leave the surface. This process can be described by an average dwell time which is given by an Arrhenius-law

$$\tau_s = \tau_s^0 \exp\left(\frac{E_0}{\mathrm{k}T}\right), \tag{4.4}$$

where E_0 is the binding energy and τ_s^0 is the dwell time in the high temperature limit, when the atoms scatters off the surface. The distribution of the times the atoms spend on the surface is given by

$$d(t_s) = \exp\left(-\frac{t_s}{\tau_s}\right). \tag{4.5}$$

In the case of adsorption equilibrium, where the rate of adsorption is equal to the rate of desorption, the amount of adsorbed atoms has a definite value.

The numbers of gaseous atoms N_g and adsorbed atoms N_s in the state of equilibrium was calculated by Fowler [Fow66] by means of statistical mechanics for the case of energetical homogeneity of the binding energies E_0 of the surface sites, neglecting interactions among the adsorbed atoms, as follows:

$$N_g = \lambda \frac{(2\pi m \mathrm{k} T)^{\frac{3}{2}} V_g}{h^3} b_g(T) \exp\left(-\frac{E_0}{\mathrm{k}T}\right), \tag{4.6}$$

$$N_s = \frac{\lambda v_s(T)}{1+\lambda v_s(T)} M_s. \tag{4.7}$$

In Eq. (4.6) The term $(2\pi m \mathrm{k} T)^{\frac{3}{2}} V_g/h^3$ is the partition function for free translation of an atom in a volume V_g, where m is the mass of the atom (hydrogen atom), k is Boltzmann's constant, T is the absolute temperature. In the case of hydrogen atoms the partition function [8] factor is $b_g(T) = 1$. The partition function is multiplied by the Boltzmann factor to take the energy difference between the lowest adsorbed state and the lowest free state E_0 in the gas into account – the heat of adsorption per atom at absolute zero (binding energy). For adsorbed atoms the partition function v_s is approximated by the partition function of a three dimensional harmonic oscillator of frequency ν and a truncation [Gel71] due to the finite depth E_0 of the hermonic potential,

$$v_s(T) = \frac{\left[1-\exp\left(-\frac{1}{3}\frac{E_0}{\mathrm{k}T}\right)\right]^3}{\left[1-\exp\left(-\frac{h\nu}{\mathrm{k}T}\right)\right]^3}. \tag{4.8}$$

In this equation the resulting partition function is the ratio of the partition function with the energy of the harmonic oscillator $h\nu$, which is typically in the order of a few percent of E_0, and the partition function with the binding energy E_0. The resulting partition function includes the fact that the maximum possible energy of the oscillator is the binding energy E_0. The partition function Eq. (4.8) increases with an increasing frequency of the harmonic oscillator and yields a constant in the high temperature limit.

The number of atoms in the gaseous and adsorbed states in Eqs. (4.6) and (4.7) are expressed in terms of partition functions, the number of possible states the atoms take on in the respective system. The dependenc of the number of adsorbed atoms on the number of atoms in the gaseous phase (and vice versa) is expressed by the parameter λ. A comparison of Eq. (4.6) and (4.7) yields $\lambda = n\Lambda^3$, where Λ is the thermal de Broglie wave length of the atoms in the gas. In the state of equilibrium λ takes on the same value in Eqs. (4.6) and (4.7) and combines them. In Eq. (4.7) the nominator takes into account, that each site can be occupied by one atom only.

With $\theta = N_s/M_s$ defined as the fraction of surface sites, which are covered, and the pressure $p = N_g \mathrm{k}T/V_g$ one obtains

$$\theta = \frac{Ap}{1+Ap}, \tag{4.9}$$

[8] The partition function is defined analogous to the Zustandssumme as the sum over the possible quantum states with energy η_r and weights ρ_r, $f(T) = \sum_r \rho_r \exp(-\eta_r/\mathrm{k}T)$.

which is known as Langmuir's adsorption isotherm [Fow66, Flo67, Sir88] with A defined as

$$A = \frac{h^3}{(2\pi m)^{\frac{3}{2}}(\mathrm{k}T)^{\frac{5}{2}}}\, v_s(T)\, \exp\left(\frac{E_0}{\mathrm{k}T}\right). \tag{4.10}$$

The adsorption isotherm given by Eq. (4.10) is only valid for the case of energetical homogeneity of the binding energies on the surface. In general a heterogeneity of the binding energies on the surface might lead to a change of the binding energy dependent on the adsorbed amount of a respective gas. The binding energy can be calculated from adsorption isotherms ($\theta(p)$ at constant T) measured at different temperatures [Sir88]. For energetical homogeneity of the binding energies on the surface, the binding energies increases with the coverage θ at a rate proportional to the strength of the adsorbate-adsorbate (lateral) interactions. It remains constant, if the interactions are weak.

The heterogeneity of the binding energies on the surface causes E_0 to decrease with θ. In addition, gas adsorption takes place on sites of different energies at all coverages θ. The sites filled at low coverage are predominantly the ones of high binding energy E_0. Sites with lower binding energy E_1 are filled when the coverage increases. A variety of models are available for the function θ which describes the adsorption of a pure gas on a energetical homogeneity of the binding energies on the surface, including models of localized adsorption and lateral interactions between adsorbed monolayers and multi layer adsorption [Sir88, Ree81].

Our data presented in the following is consistent with the assumption of an energetical homogeneity of the binding energies on the surface and the model of the Langmuir adsorption isotherm in the case of the clean cell. The data taken with the water coated cell indicate a change in the binding energy. Because information about the water coverage of the surface is not available, non of the models including lateral interactions on the surface can be applied.

4.1.1 The Rate Model

A simple kinetic theory can be used to calculate the reactive flux Z of gaseous atoms colliding with adatoms [Gel71]. The surface population is calculated using the Langmuir adsorption isotherm Eq. (4.9). The rate of recombination R is then proportional to the product of the reactive flux and the surface population Eq (4.3). The recombination coefficient γ_r is defined as the ratio of the recombination rate R and the incident flux Z_0. For small recombination coefficients $\gamma_r \ll 1$ the non-equilibrium effects on the surface population are negligible and the calculation based on rates is sufficient.

The reactive flux Z, defined as the flux of atoms incident on the surface, which leads to recombination, is

$$Z = Z_0\, g\, \sigma_0\, \exp\left(-\frac{E_a}{\mathrm{k}T}\right), \quad Z_0 = \frac{n\mathrm{k}T}{h}\Lambda, \tag{4.11}$$

where Z_0 is the incident flux of atoms on the surface, $n = N_g/V_g$ is the atom density of the gas, $\Lambda = h\,(2\pi m\mathrm{k}T)^{-\frac{1}{2}}$ is the thermal de Broglie wavelength of the atoms, and g is a statistical factor due to the electron degeneracies of the atoms and molecules [Kim67]. E_a is the activation energy for recombination. Its relation to the binding energy E_0 is given by the Hirschfelder relation $E_a = 0.055E_0$ [Hir41]. For the reaction cross section σ_0 the following hard sphere model is assumed :

$$\sigma = 0\,, \quad \text{for } \frac{1}{2}mv_z^2 < E_a, \tag{4.12}$$

$$\sigma = \sigma_0\,, \quad \text{for } \frac{1}{2}mv_z^2 > E_a, \tag{4.13}$$

which leads to the parameterization $\sigma = \sigma_0 \exp(-E_a/\mathrm{k}T)$ The recombination coefficient γ_r is defined as the ratio of R to Z_0, which is equal to the probability for a single atom to recombine during a wall collision. From Eq. (4.3) one obtains

$$\gamma_r = \frac{R}{Z_0} = 2\,g\,\theta M_s \sigma_0 \exp\left(-\frac{E_a}{\mathrm{k}T}\right). \tag{4.14}$$

The different terms in Equation (4.14) can be interpreted as follows: The cross section σ_0 is the effective surface area of a single atom adsorbed on the surface and θM_s is the occupied number of sites per unit surface area. The product of both is the probability for a gaseous atom to hit an atom adsorbed on the surface during a wall collision. The exponential term is the statistical weight, which expresses the probability to overcome the activation energy at the temperature T and describes, in combination with the remaining terms, the probability of the recombination to occur if two atoms collide. In Fig. 4.1 the recombination coefficient γ_r as a function of the temperature is plotted for two different values of the frequency of the harmonic oscillator ν (Eq. (4.8)). The relation of the binding energy E_0 to the energy $h\nu$ of the oscillator determines θ at high temperatures (Eq. (4.9)). At low frequency ν of the harmonic oscillator the number of thermally accessible bound states is large (partition function) and results in a high coverage of the surface, thus a higher coverage of the surface is found in the case of a low frequency ν compared to a high frequency ν (Fig. 4.1).

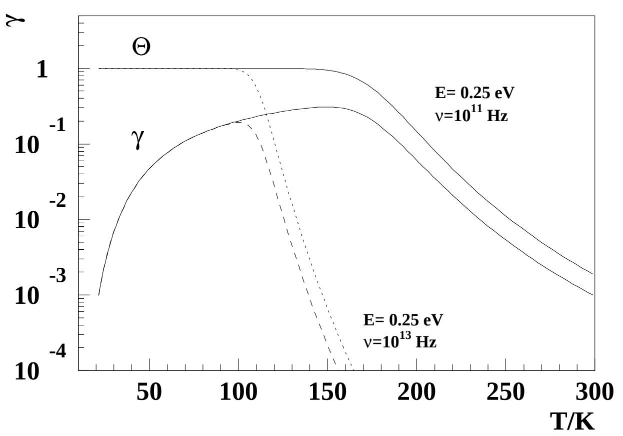

Fig. 4.1: Coverage θ and recombination coefficient γ_r dependent on temperature for two different frequencies ν of the harmonic oscillator at the same binding energy. The lower oscillator frequency ν results in a higher coverage of the surface. The data is plotted asuming a density of $n = 2 \cdot 10^{12}$ atomscm^{-3} and an arbitrary binding energiy and oscillator frequencies.

In the limits of low and high temperatures, γ_r can be approximated as follows:

$$T^< : \quad \theta \approx 1, \quad \gamma_r^< = 2gM_s\sigma_0 \exp\left(\frac{-E_a}{\mathrm{k}T}\right), \tag{4.15}$$

$$T^> : \quad \theta \ll 1, \quad \gamma_r^> = 2gM_s\sigma_0 n\Lambda^3 v_s(T) \exp\left(\frac{E_0}{\mathrm{k}T}\right), \tag{4.16}$$

using $E_a \ll E_0$. In the low temperature limit γ_r is density independent, whereas in the high temperature limit γ_r shows a linear dependenc on the density n of the gas. In the case of hydrogen recombination there are two types of binding sites on the surface. The first causes chemisorption of an atom on the surface which builds a chemical bond with the surface atoms (CH-sites). The second is physisorption of an atom due to the much weaker Van der Waals forces (PH-sites). Both types are described by different binding energies E_0 and respective activation energies E_a given by the Hirschfelder relation. The total recombination coefficient is given by the sum

$$\gamma_r = \sum_j \gamma_r^{(j)}, \tag{4.17}$$

where the contribution from both types of sites is added independently.

4.1.2 The Steady State Model

In the case of a high recombination coefficient γ_r the rate of recombination R and the surface coverage θ can be described by a steady state condition [Gel71], where the number of atoms incident on the surface is equal to the number, which evaporate either as atoms or as molecules. A comparison with the results from the previous section yields expressions for the fluxes of atoms and molecules, which evaporate from the surface. The contributions from the two different binding sites is of interest in understanding the average polarization of the target and will be discussed in Chaps. 5 and 7.

The steady state condition is given by the definition of the steady state coverage of the surface

$$\theta^{(s)} = 1 - \frac{\mathcal{V}}{Z_0} - \frac{\mathcal{R}}{2Z_0}, \tag{4.18}$$

where Z_0 is the collision frequency of atoms incident on a unit area of the surface and $\mathcal{V}$ and $\mathcal{R}$ are the evaporation flux and the recombination flux, respectively. Introducing the dimensionless ratios ϕ_v and ϕ_r defined by

$$\mathcal{V} = Z_0\theta^{(s)}\phi_v, \qquad \mathcal{R} = Z_0\theta^{(s)}\phi_r, \tag{4.19}$$

the steady state coverage is expressed as

$$\theta^{(s)} = \frac{1}{1 + \phi_v + \frac{1}{2}\phi_r}. \tag{4.20}$$

A comparison of Eq. (4.20) with (4.9) under the conditions $\theta = 1$ and $\mathcal{R} = 0$ yields an expression for ϕ_v and a comparison of Eq. (4.19) with (4.14) yields an expression for ϕ_r:

$$\phi_v = \frac{1}{n\Lambda^3 v_s(T)} \exp\left(\frac{E_0}{\mathrm{k}T}\right), \tag{4.21}$$

$$\phi_r = 2g\sigma_0 M_s \exp\left(-\frac{E_a}{\mathrm{k}T}\right). \tag{4.22}$$

The recombination coefficient in the steady state $\gamma_r^{(s)}$ is given by the same definition as in Eq. (4.14)

$$\gamma_r^{(s)} = \frac{\mathcal{R}}{Z_0} = \theta^{(s)}\phi_r. \tag{4.23}$$

It is related to the recombination coefficient of the semi equilibrium state γ_r (Eq. (4.14)) by

$$\gamma_r^{(s)} = \frac{\gamma_r}{1 + \frac{1}{2}\gamma_r} \tag{4.24}$$

and for low values of γ_r the relation $\gamma_r \approx \gamma_r^{(s)}$ is true. The rates $\mathcal{V}$ and $\mathcal{R}$ are defined for each type of sites separately. They can be calculated, if the parameter values involved in the calculation of γ_r are known.

The recombination process has an influence on the average dwell time of the adsorbed atoms and in comparison to desorption it removes the atoms faster. The average dwell time $\tilde{\tau}_s$ which results if atoms recombine can be calculated from the evaporation rates $\mathcal{V}$ and $\mathcal{R}$. The evaporation rate depends on the number N_s of atoms on the surface, which is equal to the number of sites multiplied by the coverage, $M_s \cdot \theta^{(s)}$. The average time in which N atoms desorb from the surface is τ_s and the evaporation rate yields $\mathcal{V} = N\tau_s^{-1}$. The atoms which desorb from the surface show a dwell time distribution $d(t_s)$ independent of recombination. Any additional recombination rate $\mathcal{R}$ lowers the dwell times t_s for the atoms, which recombine. Thus, the average dwell time $\tilde{\tau}_s$ is given by the ratio of the number of atoms on the surface and the desorption and recombination rates:

$$\tilde{\tau}_s = \frac{M_s\theta^{(s)}}{\mathcal{V} + \frac{1}{2}\mathcal{R}}. \tag{4.25}$$

The time distribution is then

$$\tilde{d}(t_s) = \exp\left(-\frac{t_s}{\tilde{\tau}_s}\right) \tag{4.26}$$

with $\tilde{\tau}_s$ from Eq. (4.25).

4.2 Determination of the Recombination Coefficient

In order to calculate the recombination coefficient γ_r the relation between α^{TGA} and γ_r from Eq. (3.18) can be used. This function, which includes the ballistic and diffusive term, cannot be solved for γ_r, but a fit of the function from Eq. (3.18) to the measured α^{TGA} data allows the determination of the recombination coefficient. Measurements of the degree of dissociation in a clean cell were taken over a range in temperature from

35 K to 260 K a short time after a cell exchange and are shown in Fig 4.2 as data points. The Drifilm surface was not yet exposed to the synchrotron light of the HERA beam and therefore no damage of the Drifilm coating is assumed. The amount of water entering the cell from the ABS was small.

To describe the recombination coefficients for both types of sites several parameters are necessary. The values used in the fit are listed below. The density n was set to the average atom density inside the target cell and g and σ_0 are taken from references [Gel71, Kim67].

$$
\begin{aligned}
n &= 2 \cdot 10^{12}\,\mathrm{cm}^{-2}, \\
g &= \tfrac{1}{4}, \\
\sigma_0 &= \pi r^2(H_2) = 1.72 \cdot 10^{-16}\ \mathrm{cm}^2.
\end{aligned}
$$

The binding energies $E_0^{(1,2)}$ as well as the area density of binding sites and the frequency in the harmonic binding potential $\nu^{(2)}$ are fitted to the data. The resulting function for α^{TGA} is plotted in Figure 4.2, left, as a solid line. The parameters are listed in the following table with a value of $\chi^2 = 0.003$.

$$
\begin{aligned}
M_s^{(1)} &= (0.09 \pm 0.01) \cdot 10^{15}\ \mathrm{sites\,cm}^{-2}, & M_s^{(2)} &= (1.08 \pm 0.05) \cdot 10^{15}\ \mathrm{sites\,cm}^{-2}, \\
E_0^{(1)} &= (0.611 \pm 0.015)\,\mathrm{eV}, & E_0^{(2)} &= (0.0318 \pm 0.0004)\,\mathrm{eV}, \\
\nu^{(1)} &= \text{—} & \nu^{(2)} &= (1.39 \pm 0.06) \cdot 10^{10}\,\mathrm{Hz}.
\end{aligned}
$$

The value for $\nu^{(1)}$ could not be fitted to the data because the recombination on the CH-sites is not dependent on the harmonic potential in the measured temperature range.

The binding energies of both types of sites differ significantly. Each layer can be considered as independent and the recombination coefficient γ_r was calculated using Eq. (4.17) and is plotted in Figure 4.2, right, as a solid line. The slope of the function for the PH-sites determines the binding energy and the frequency of the harmonic oscillator as shown in Figure 4.2. The slope of the function α^{TGA} for the CH-sites is given by the activation energy E_a calculated from the binding energy using the Hirschfelder relation. The fraction of the surface, which is covered with hydrogen atoms in the limit $\theta \to 1$, is the product of the number M_s and the surface area of a single hydrogen atom $\pi r^2(H_2)$ and yields $M_s^{(1)} \cdot \pi r^2(H_2) = 0.016$ and $M_s^{(2)} \cdot \pi r(H_2) = 0.19$. The number of sites with a high binding energy is a factor of eleven lower compared to the number of sites with a low binding energy. This is expected due to the nature of the bond, the number of chemisorption sites is lower compared to the number of physisorption sites. On the other hand, a full coverage of the surface is expected, which leads to $\sum_i M_s^{(i)} \cdot \pi r^2(H_2) = 1$. The full coverage of binding sites is observed as the well known $cos\theta$ distribution of the emission angles of atoms from the surface. A possible explanation for the difference in the fitted values and the expected values might be found in additional binding sites with much lower binding energy or a higher cross section compared to the one assumed in the calculation.

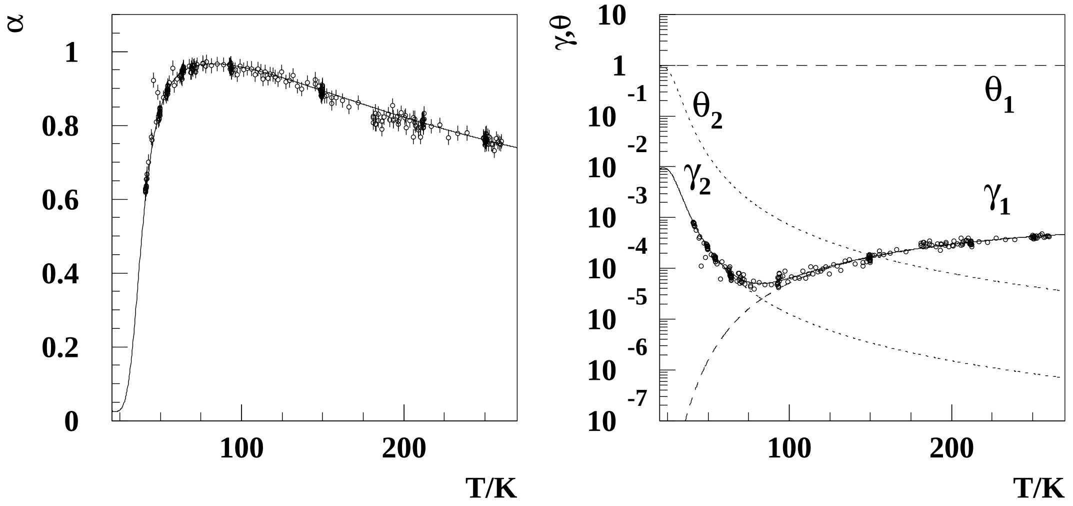

Fig. 4.2: Measured α^{TGA} values versus temperature for a clean cell (open circles, left). The solid line shows a fit of α^{TGA} assuming two different types of sites. The calculated values for γ_r (Eq. (4.27)) and $\theta_{1,2}$ are plotted with fitted functions for γ_r (open circles, right). The solid line represents the sum $\gamma_r = \gamma_r^{(1)} + \gamma_r^{(2)}$. The dashed lines represent θ_1 and $\gamma_r^{(1)}$ and the dotted lines θ_2 and $\gamma_r^{(2)}$.

A simplification of Eq. (3.18), which neglects the term D', can be solved for γ_r, using the TGA fluxes for mass 1 and mass 2

$$\gamma_r = \frac{\tilde{n}_2}{\tilde{n}_1}\frac{1}{N_0} = \frac{\Phi_2^{TGA}}{\Phi_1^{TGA}}\frac{1}{N_0}, \tag{4.27}$$

where $N_0 \neq \langle b \rangle$ is taken from Tab. 3.1. The simplification in this equation leads to a shift for a calculated γ_r to lower values by a factor of 2.75 because the effect of recombination of atoms with a low number of wall collisions is overestimated assuming only an exponentially decaying function A_e. However, the important information about the temperature dependenc of γ_r can be deduced. The values of the recombination coefficient γ_r calculated by Eq. (4.27) are plotted in Figure 4.2, right, and shifted on top of the fitted function to show the temperature behavior.

Plots of the evaporation rates of atoms and molecules calculated within the steady state model are based on the fitted parameters and are shown in Fig. 4.3. The steady state coverage shows a similar behavior as the coverage calculated by the absolute rate model. The evaporation rates of the atoms differ significantly for the two types of binding sites. The rate $\mathcal{V}_2$ is constant over the whole temperature range whereas the rate $\mathcal{V}_1$ is three orders of magnitude lower at 300 K and it keeps decreasing for lower temperatures. The atoms in the gas phase are dominated by atoms evaporating from the PH-sites. The fit yields $Z_0 = 7.2 \cdot 10^{16}\,\mathrm{atoms\,s^{-1}\,cm^{-2}}$, which is in good agreement with the injected nucleon flux from the ABS. The evaporation rates of recombined atoms show a different behavior. From 300 K to 80 K the recombined atoms originate predominantly from the

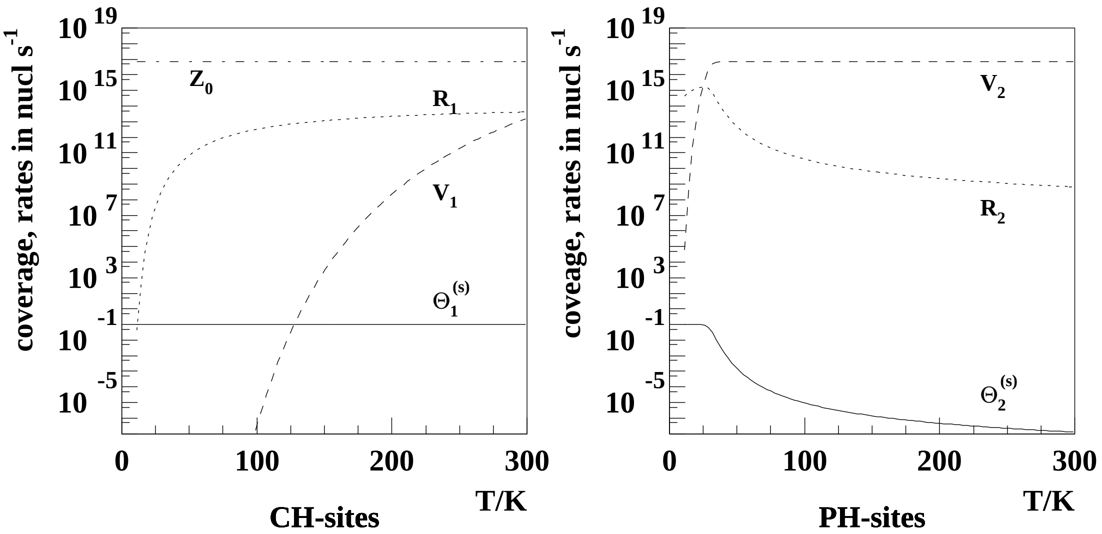

Fig. 4.3: Evaporation rates of atoms and molecules from CH- and PH-sites per unit area (cm^{-2}). The dashed and dotted lines represent the evaporation rates of atoms ($\mathcal{V}_{1,2}$) and recombined atoms ($\mathcal{R}_{1,2}$) respectively. The dashed dotted line represents the flux Z_0. The solid line represent the steady state coverages ($\theta_{1,2}^{(s)}$) of the two binding sites.

CH-sites whereas at 80 K both layers contribute equally and below 80 K recombined atoms originate predominantly from the PH-sites.

Inside the storage cell where the atoms undergo a large number of wall collisions the rates Z_0, $\mathcal{V}$ and $\mathcal{R}$ are not independent. Atoms, which evaporate, participate in the rate Z_0 at the next wall collision. Atoms, which recombine and form the rate $\mathcal{R}$, deplete the rate Z_0 and do not participate as atoms in the following wall collisions. Due to the flow of atoms from the cell center to the exit of the cell a change in the incident rate Z_0 dependent on the position inside the cell is therefore expected.

4.3 The Effect of Water on the Recombination of Hydrogen

To achieve a high degree of dissociation inside the ABS dissociator, a small amount of oxygen is added to the hydrogen gas input [Wis67, Kor90]. As a result, water molecules are injected into the target cell by means of ballistic flow through the ABS and cause a much higher water coverage of the cell walls compared to the clean cell.

In this case an additional complexity results from the competitive adsorption of the components of the gas mixture on the binding sites of the surface. The binding energies for the single components could possibly be estimated from the pure gas adsorption isotherms, but the surface energy of a site might be altered by the presence of another component [Fow66]. The adsorption isotherm Eq. (4.8) can be extended for the case of a gas mixture of a number of j components [Sir88, Fow66] for the simple case of all particles having the same size (equal m_j):

$$\theta_i = \frac{A_i p_i}{1 + \sum_j A_j p_j}. \tag{4.28}$$

Further studies on the adsorption of components with different sizes (unequal m_j) were made using numerical techniques [Sir88], but can not be applied in the present work. It follows from Eq. (4.28), that an additional water coverage of the surface reduces the coverage for hydrogen and results in a lower recombination coefficient $\gamma_r \propto \theta$. A measurement of α_r^{TGA} and γ_r with a cell, which was exposed to the beam for 1 month and is covered with water, is shown in Figure 4.4. It should be noted that α_r^{TGA} is very near to unity at temperatures above 60 K. The data were taken a month after the data shown in Figure 4.2 as data points. The effect due to the water results in a different slope for the function

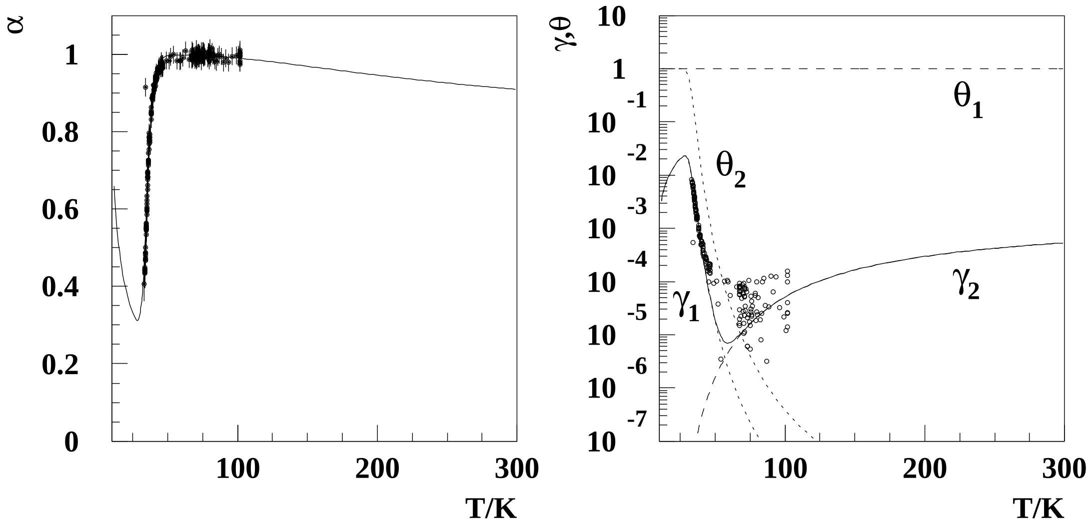

Fig. 4.4: Measured alpha values versus temperature for a water covered cell (open circles, left). The solid line shows α calculated from the fitted values. The calculated values for γ_r are plotted with the function for the recombination coefficients (open circles, right). The solid line represents the sum of the recombination coefficients.

for α^{TGA} in the low temperature range where recombination occurs predominantly on PH-sites. The parameters for the function α^{TGA} according to the PH-sites are listed in the following table.

$$\begin{array}{rlrl}
M_s^{(1)}= & (0.020 \pm 0.007)\cdot 10^{15}\ \mathrm{sites\,cm^{-2}}, & M_s^{(2)}= & (1.08 \pm 0.01)\cdot 10^{15}\ \mathrm{sites}\cdot\mathrm{cm^{-2}}, \\
E_0^{(1)}= & 0.611\,\mathrm{eV}, & E_0^{(2)}= & (0.060 \pm 0.001)\,\mathrm{eV}, \\
\nu^{(1)}= & \text{—} & \nu^{(2)}= & (6.5 \pm 0.6)\cdot 10^{11}\,\mathrm{Hz}.
\end{array}$$

The values for $\nu^{(1)}$ and $E_0^{(1)}$ could not be fitted. The binding energy of the CH-sites is taken from the clean cell measurements.

The temperature where the two recombination coefficients for atoms bound to PH- and CH-sites are equal has changed from 85 K to 65 K and the number of CH-sites is lowered by a factor of 5 compared to the clean cell. This reduction might be explained by occupation of CH-sites by water molecules, which reduces the number of sites for hydrogen atoms and thus reduces the hydrogen coverage of the surface. The slope of γ_r in the low temperature range can only be explained in the present model by a higher frequency in the harmonic binding potential and a higher binding energy E_0, which also reduces the recombination on the PH-sites. The number of binding sites is not chnaged. A possible explanation is that the additional water on the surface changes the isotherm due to additional interactions between the water and the hydrogen. This can be the reason for the increase in binding energy, but the model presented here is not able to explain the interactions of hydrogen and water on the surface. However, it is able to give a good description in the case of a clean cell and shows that the assumption of Langmuir adsorption is valid.

For further calculations the above fit parameters for the water coated cell are used as an approximation for the temperature dependence of the recombination with a water coated cell.

4.4 Degree of Dissociation in the Target Cell

The calculation of the degree of dissociation inside the cell α_r^T is carried out in a similar way as the calculation of α^{TGA}. The age distributions $N(Z,b)$ from Eq. (3.9) are used. The value for γ_r can be determined from the measurements of α^{TGA} under the assumption that γ_r has the same value throughout the cell. In addition to the differences in the ages of the atoms inside the cell and the sample tubes the calculation of α_r^T involves an additional correction for the density of the atoms and molecuyles inside the cell. The definition of α^{TGA} in Eq. (2.2) is based on flow rates and the total flow rate in the denominator is a constant if the input flow from the ABS is constant. In constrast, α^T is defined by the densities of nucleons in atoms and molecules inside the cell

$$\alpha^T = \frac{n_1^T}{n_1^T + n_2^T}. \tag{4.29}$$

The velocity of the atoms is at thermal equilibrium a factor of $\sqrt{2}$ higher than the velocity of the molecules. Nucleons which are injected into the cell as atoms and recombine to molecules yield a factor of $\sqrt{2}$ higher density, because of the different conductance due to the difference in velocity. Thus the total nucleon density (denominator in Eq. (4.29)) depends on the recombination.

According to Sec. 3.2 the degree of dissociation inside the cell α_r^T including the change in density can be written using age distributions as follows:

$$\alpha_r^T = \frac{\tilde{n}_1^T}{\sqrt{2}\tilde{n}^T - (\sqrt{2}-1)\tilde{n}_1^T} = \frac{\int_0^\infty A_e^r(b)\,db}{\int_0^\infty \sqrt{2}A_e(b) - (\sqrt{2}-1)A_e^r(b)\,db}, \tag{4.30}$$

where $\tilde{n}^T = \tilde{n}_1 + \tilde{n}_2$ is the number density of the sum of the atomic and molecular components (Eq. (3.15)) and $\tilde{n}_1^T$ and $\tilde{n}_2^T$ are the number densities of the atomic and molecular components inside the cell, respectively. The change in density can be expressed by a factor k_0 which is defined as

$$k_0 = \frac{\sqrt{2}\tilde{n}^T - (\sqrt{2}-1)\tilde{n}_1^T}{\tilde{n}^T}. \tag{4.31}$$

The previous measurements show that water adsorbed on the surface has a large influence on the recombination of hydrogen. The beam interaction might cause water to evaporate from the surface and change the recombination rate inside the cell. The effect on the measured degree of dissociation α^{TGA} is shown in Fig. 1.5, where the amount of water entering the cell from the ABS was small. The sample and extension tubes are not as strongly exposed to the HERA beam as the cell tube. This might lead to a different recombination rate in the cell and sample tubes. The dependence of α_r^T on α^{TGA} in the case of a difference between the recombination coefficients of cell γ_r^{ct} and sample tubes γ_r^{st} will change the relation as shown as an exapmle in Fig. 4.5 for the case $\gamma_r^{\mathrm{T}} = 5\,\gamma_r^{\mathrm{TGA}}$. This case might appear, if the cell and the sample tubes interact differently with the wake fields of the HERA beam.

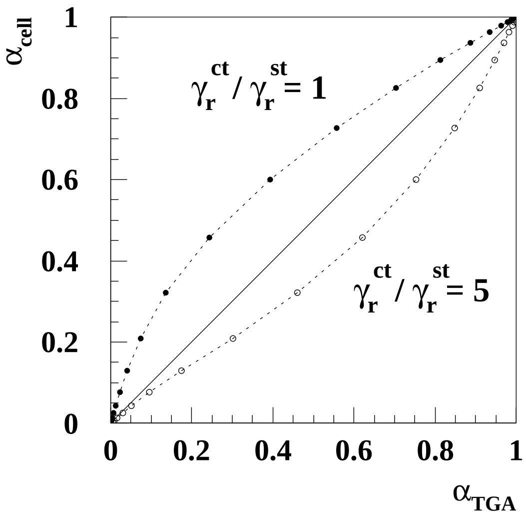

Fig. 4.5:
Calculations of α_r^{TGA} versus α_r^T for a uniform cell (dots) and a non-uniform cell with a ratio in the recombination coefficients of cell (ct) and smaple tube (st) of $\gamma_r^{\mathrm{ct}} = 5\,\gamma_r^{\mathrm{st}}$ (open circles), based on the Monte-Carlo simulations.

The value of α_r^T can be put into relation to the value of α_r^{TGA} whith the factor k_0, which accounts for the change in density inside the cell, and an additional factor c_r^α, which describes the difference in the recombination probability in the cell and sample tube

$$\alpha_r^T = \frac{c_r^\alpha}{k_0} \cdot \alpha_r^{\mathrm{TGA}} \tag{4.32}$$

The factor c_r^α depends on the uniformity of the cell surface with respect to the recombination coefficient. Both factors can be calculated by means of Monte Carlo simulations.

5 Spin Relaxation inside the Storage Cell

There are two spin relaxation processes, that have an effect on the polarization of the atoms inside the target cell, that are

- Wall relaxation: if an atom collides with the wall and adsorbs, it may diffuse on the surface and the resulting fluctuating fields, caused by the magnetic moments of the surface atoms, lead to a change of the hyperfine state of the atom.
- Spin exchange collisions: hydrogen atoms collide in the gaseous state and the spins of the electrons of both atoms interact.

In both cases the interaction affects the electron. The proton spin is coupled to the electron in states $|\,2\,\rangle$ and $|\,4\,\rangle$, with a coupling dependent on the magnetic holding field, and is effected too.

The different relaxations due to wall collisions and spin exchange collisions cannot be treated separately. After the interaction with the surface during a wall collision the atoms, now in the gaseous phase, interact through spin exchange collision and at the next wall collision they interact again with the surface. Since the atoms are constantly exposed to both interactions, an appropriate description is given by the following rate equation [Bra95] for the occupation numbers n_i of the substates $|\,i\,\rangle$, which can be solved numerically :

$$\frac{dn_c}{dt} = \sum_a W_{ac}(n_a - n_c) + \tau_{se}^{-1} \sum_{a,b} M_{ab}^c n_a n_b + t_{res}^{-1}(n_c^i - n_c). \tag{5.1}$$

The first terms represent the change of the occupation number n_c due to wall depolarization dependent on the transition probability per unit time W_{ac} encluding the hyperfine mixing. The second term represents the change of the occupation number n_c due to spin exchange collisions, where τ_{se} is the collision rate and M_{ab}^c is the transition probability for a transition from the initial states $|\,a\,\rangle$ and $|\,b\,\rangle$ to the final state $|\,c\,\rangle$ and $|\,d\,\rangle$. The third term takes the flow of atoms through the cell into account and is dependent on the initial and equilibrium occupation numbers n_c^i and n_c of the state $|\,c\,\rangle$ and the residence time t_{res} inside the cell. The effects due to recombination are not included in this formula.

The underlying assumption in this model is a homogeneous distribution of the density inside the cell and the same state of equilibrium at any position. It is also based on an average residence time of the atoms independent of the age distribution. An extension to a formalism including the cell geometry and density distribution inside the cell leads to a differential equation, which is based on the particle flow in the cell and is similar to the type of diffusion equations given in Chap. 3, where the collision age is replaced by the residence time. A similar approach was made for the recombination inside the cell [Bau96]. The different age distributions of atoms or molecules detected by the TGA and BRP cannot be simulated, especially ballistic components of the flow detected by the BRP.

The calculation of the influence of relaxation processes on the atoms based on age distribution includes the dependence of the relaxation on the age of the atoms, their position inside the cell and the acceptance of the TGA and BRP. For measurements of the recombination and relaxation coefficients using the TGA and BRP, the technique of analyzing age distributions is more sufficient because of the difference in the respective age distributions. The recombination is included in the calculation. The interacting effects of wall collisions and spin exchange collisions are not correctly described by this technique, but with measurements at high magnetic holding field the approximation of independent processes can be made.

The first section gives an overview of the theory of spin exchange collisions. It is followed by the theory of wall relaxation, which is based on surface diffusion of the hydrogen atoms. At the end of this chapter measurements of the depolarization in a clean and a water coated cell are presented. Fits of functions for the temperature dependence of the polarization including recombination and spin relaxation are used to obtain the wall collision relaxation coefficient and parameters, which characterize the surface diffusion. The corrections needed on P^{BRP} to calculate the polarization of the atoms in the target P_a^T is shown by calculating the effect of different wall relaxation probabilities on the age distributions.

5.1 Spin Exchange Collisions

Spin exchange collisions appear as a collision of two hydrogen atoms in the gaseous phase, where the spins of the electrons of both atoms interact. E. M. Purcell and G. B. Field [Pur56] and others [Swe85] described the interaction using an operator

$$\mathbf{U} = \mathbf{P}_s + \exp(-i\Phi)\mathbf{P}_t, \tag{5.2}$$

where the operators $\mathbf{P}_s$ and $\mathbf{P}_t$ are, respectively, projection operators on the singlet (attractive) and triplet (repulsive) electronic state of the combined system of interacting electron spins. The probability of a transition from an initial state $|\, ab\,\rangle$ to a final state $|\, cd\rangle$ of two hydrogen atoms is given by $|\,\langle\, cd\,|\,\mathbf{U}\,|\, ab\,\rangle\,|^2$, where a, b, c, and d are the respective hyperfine states. An integration of the difference of the singlet and triplet potentials over the collision time yields the phase factor

$$\Phi = \int \frac{V_t - V_s}{\hbar} dt. \tag{5.3}$$

The collision time is long in comparison to the period of oscillation resulting in $\phi \gg 2\pi$. This is called a 'strong' collision and results in an electron spin flip probability of $\frac{1}{2}$. The exchange rate is given by

$$\tau_{se}^{-1} = n \left\langle \sigma_{se} v \right\rangle, \tag{5.4}$$

where n is the atomic density, σ_{se} is the cross section for spin exchange, and v is the velocity of the atoms. The cross section has been measured in a temperature range from

77 K to 363 K [Des76] with a value of $\sigma_{se} = (2.31 \pm 0.28) \cdot 10^{-15}\mathrm{cm}^2$ and is constant in agreement with theoretical expectations [All72, Wit56]. The effect of spin exchange on a sample of atoms inside a storage cell is independent of the temperature of the cell because the atoms are injected at constant flux and the temperature dependence of the velocity and the density cancel in Eq. (5.4). A remaining effect is caused by a increase in the residence time of the atoms, which leads to a temperature dependence of the relaxation due to spin exchange collision proportional to $T^{-\frac{1}{2}}$.

In a very strong magnetic holding field the electron and nucleon spins are decoupled. A spin exchange collision results in an exchange of the electron spins. The nucleon acts as a spectator and the only possible exchange in terms of the representation $|\, m_I; m_S \,\rangle$ is

$$|\,+;+\,\rangle + |\,-;-\,\rangle \leftrightarrow |\,-;+\,\rangle + |\,+;-\,\rangle \quad \text{or} \quad |\,1\,\rangle + |\,3\,\rangle \leftrightarrow |\,2\,\rangle + |\,4\,\rangle\,. \tag{5.5}$$

In a weak magnetic holding field the states $|\,2\,\rangle$ and $|\,4\,\rangle$ are mixed states formed by linear combinations of the pure states $|\,+;-\,\rangle$ and $|\,-;+\,\rangle$. In this case the polarization of the nucleon can change too. Since the total angular momentum is conserved during a collision, the sum of the individual quantum numbers m_F must remain constant throughout the interaction

$$m_F^{(1)} + m_F^{(2)} = \text{constant}, \tag{5.6}$$

but a transfer of polarization from electrons to nucleons takes place. The pairs of atoms in states a and b which undergo spin exchange collisions conserving the angular momentum are listed in Tab. 5.1. As a consequence a sample of atoms in state $|\,1\,\rangle$ or $|\,3\,\rangle$ shows no

$\sum_i m_F^{(i)}$	$\vert\, a\,\rangle \vert\, b\,\rangle$
2	$\vert 1\rangle\vert 1\rangle$
1	$\vert 2\rangle\vert 2\rangle$ $\vert 1\rangle\vert 4\rangle$
0	$\vert 1\rangle\vert 3\rangle$ $\vert 2\rangle\vert 2\rangle$ $\vert 2\rangle\vert 4\rangle$ $\vert 4\rangle\vert 4\rangle$
-1	$\vert 2\rangle\vert 3\rangle$ $\vert 3\rangle\vert 4\rangle$
-2	$\vert 3\rangle\vert 3\rangle$

Tab. 5.1: Spin exchange collisions conserving the angular momentum.

relaxation via spin exchange collisions. A specific state $|\,q\,\rangle$ is given by

$$|\,q\,\rangle = q_+ \left|+;(m_q - \tfrac{1}{2})\right\rangle + q_- \left|-;(m_q + \tfrac{1}{2})\right\rangle, \tag{5.7}$$

where m_q is defined as $m_q = \langle\, q\,|\,\mathbf{F}_z\,|\,q\,\rangle$ and $q_\pm$ are factors applied to the eigenstates common to $|\,m_I; m_S\,\rangle$. They depend on the external magnetic field and can be expressed by a mixing angle θ defined by Eqs. (1.11). The transition coefficients M_{ab}^c from Eq. (5.1) which describe the relaxation from states $|\, ab\,\rangle$ to state c in $|\, cd\,\rangle$ are then given by [Wal93]

$$\begin{aligned} M_{ab}^c = \sum_d \quad & -2\ \langle c|a\rangle\, \langle d|b\rangle\, (a_+b_-c_+d_- + a_-b_+c_-d_+) \\ & + \langle m_c|m_a\rangle\, \langle m_d|m_b\rangle\, (a_+b_-c_+d_- + a_-b_+c_-d_+)^2 \\ & + \langle m_c|m_a - 1\rangle\, \langle m_d|m_b + 1\rangle\, (a_+b_-c_+d_-)^2 \\ & + \langle m_c|m_a + 1\rangle\, \langle m_d|m_b - 1\rangle\, (a_-b_+c_-d_+)^2. \end{aligned} \tag{5.8}$$

Using the condition $\sum_i n_i = 1$ and the fact that the conservation of angular momentum leads to a constant expectation value for $\mathbf{F}_z$, $\langle \mathbf{F}_z \rangle = n_1 - n_3$, Eq. (5.8) leads to the following time dependence of the hyperfine states:

$$\tau_{se} \frac{d(n_2 - n_4)}{dt} = -\sin^2 2\theta\, (n_2 - n_4), \tag{5.9}$$

$$\tau_{se} \frac{d(n_2 + n_4)}{dt} = -(n_2 + n_4) + \frac{1 - (n_1 - n_3)^2}{2} + (n_2 - n_4)\frac{\cos^2 2\theta}{2}. \tag{5.10}$$

An important effect of the spin exchange collisions on the occupation of the hyperfine states, which follows from the integration of Eq. (5.9) [Wal93], is an exponential decay of the difference of states $|\, 2\,\rangle$ and $|\, 4\,\rangle$:

$$n_2 - n_4 = (n_2 - n_4)_0 \exp\left(-t \frac{\sin^2 2\theta}{\tau_{se}} \right). \tag{5.11}$$

Eq. (5.10) shows the relaxation between the mixed states $|\, 2\,\rangle$ and $|\, 4\,\rangle$ and the pure states $|\, 1\,\rangle$ and $|\, 3\,\rangle$. The time constant, which describes the relaxation process to a state of equilibrium is

$$\tau_{eq} = \frac{\tau_{se}}{\sin^2 2\theta} = (1 + x^2)\tau_{se}. \tag{5.12}$$

The external magnetic field gives a scaling factor which is multiplied with the relaxation rate τ_{se} so that the relaxation at high fields is much slower than at low fields. The expected spin exchange rate τ_{se}^{-1} in the HERMES target cell can be calculated using Eq. (5.4) with an average atomic density of $n = 2 \cdot 10^{12}\,\mathrm{cm}^{-3}$ and a thermal velocity of $v = 1.4 \cdot 10^3\,\mathrm{m\,s}^{-1}$ and yields $\tau_{se}^{-1} = 647\,\mathrm{s}^{-1}$. With an average residence time of the atoms inside the cell of $t_{res} = 3\,\mathrm{ms}$ a single atom experiences about 1.9 spin exchange collisions inside the cell. Atoms detected by the BRP leave the sample tubes and have a higher residence time of $t_{res} = 4.4\,\mathrm{ms}$. This results in an average number of spin exchange collisions inside the sample tubes of 2.8. The relaxation time τ_{eq} at the nominal holding field of 335 mT is a factor of $(1 + x^2) \approx 50$ higher than the relaxation time τ_{se}. Due to the high holding field the spin exchange collision can also be described separately as a relaxation of the proton or electron polarization. If proton polarized states $|\, 1\,\rangle + |\, 4\,\rangle$ ($n_1 = n_4 = 0.5$) are injected, the effect on the state $|\, 4\,\rangle$ is calculated using Eq. (5.11) and results in $P_n(t_{res}) = 0.973 P_n(0)$ measured by the BRP.

5.2 Spin Relaxation by Wall Collisions

When an atom strikes the wall, the Van der Waals attraction causes it to adsorb for a brief time. The time distribution of the dwell times is given by Eq. (4.5). The adsorption interaction potential on the surface is not smooth. The diffusion of the atom on the surface and the oscillation of the atom in one site both result in a fluctuating magnetic field seen by the atom. The relaxation process can be described as an interaction of the magnetic field with the spin of the atom [Mem88, Hor82]

$$\mathbf{H_1}(t) = \gamma_s b(t)\mathbf{S}, \tag{5.13}$$

where $b(t)$ is the fluctuating field and $\mathbf{S}$ is the spin operator of the valence electron of the adsorbant. For the atoms on the surface the interaction with the fluctuating fields induces transitions from an initial substate $|\, a\,\rangle$ to substate $|\, b\,\rangle$. The time evolution of a sample of atoms in magnetic sub-states n_i is then given by the equation [Abr78, Pre94]

$$\dot{n}_a = \sum_b W_{ab}\,(n_a - n_b). \tag{5.14}$$

The transition probabilities per unit time W_{ab} can be expressed by a correlation of $\mathbf{H}_1(t)$ at different times $t = 0, t = t'$ and is defined as

$$G(t) = \overline{\langle\, b \,|\, \mathbf{H}_1(t=0) \,|\, a\,\rangle \langle\, a \,|\, \mathbf{H}_1(t=t') \,|\, b\,\rangle} \tag{5.15}$$

and results in

$$\hbar^2 W_{ab} = G(0)\, J(\omega_{ab}), \tag{5.16}$$

where $G(0)$ is the normalized autocorrelation function of $\mathbf{H}_1(t)$ and $J(\omega_{ab})$ is the spectral density of the fluctuating part of the matrix element at the transition frequency ω_{ab}. The spectral density function itself is the Fourier transform of the time correlation function $G(t)$

$$J(\omega_{ab}) = \frac{1}{G(0)} \int_0^\infty G(t)\, \exp(-i\omega_{ab})dt. \tag{5.17}$$

There are different interpretations of the correlation function. The phenomenological BPP model [Blo48] assumes a function

$$G(t) = G(0)\, \exp\left(-\frac{t}{\tau_c}\right), \tag{5.18}$$

where τ_c is a correlation time. It is the time interval t' in which the interaction $\mathbf{H}_1(t = t')$ is significantly correlated to the interaction $\mathbf{H}_1(t = 0)$. If diffusion is the model assumed to be the underlying process, then τ_c can be interpreted as an inverse jump rate Γ [Pre94]:

$$\tau_c = \frac{1}{\Gamma} = \frac{\lambda^2}{D}, \tag{5.19}$$

where λ is the hopping distance and D is the diffusion constant. Calculating the integral Eq. (5.17) using the function given by Eq. (5.18) one finds the spectral density distribution

$$J(\omega_{ab}) = \frac{2\tau_c}{1+\omega_{ab}^2\tau_c^2}. \tag{5.20}$$

The frequency ω_{ab} which is the transition frequency between the substates $|\,a\,\rangle$ and $|\,b\,\rangle$ is set in relation to the correlation time τ_c. In the limit of a short correlation time $\tau_c \to 0$ the resonant system has too little time to react to the interaction and $J(\omega_{ab}) \to 0$. In the limit of a long correlation time $J(\omega_{ab})$ depends on the product $\omega_{ab}\tau_c$. If $\omega_{ab} \gg \tau_c$, again, the resonant system has too little time to react on the interaction. If $\omega_{ab} \ll \tau_c$ and $\omega_{ab}\tau_c \ll 1$ then the function $J(\omega_{ab})$ depends linear on τ_c and the transition probability increases with an increasing τ_c.

Restrictions on the function for the correlation time τ_c arise from the dependence of the diffusion of the atoms on the surface and on the energetical homogeneity of the binding energies on the surface. An adsorbed atom normally sits in one of the potential minima associated with binding sites. While jumping to a different site it needs to overcome the potential barrier of energy $\Delta E_j < E_0$. In a Langmuir layer, a binding site can accommodate one atom only. The jump rate Γ in some direction is then given by

$$\Gamma = \nu_0 \exp\left(\frac{\Delta E_j}{\mathrm{k}T}\right), \tag{5.21}$$

where ν_0 is the jump rate in the high temperature limit. The net flow Φ, given by

$$\Phi = -D\frac{\partial c}{\partial x}, \tag{5.22}$$

where $\partial c/\partial x$ is the surface concentration gradient, yields the diffusion constant

$$D = \nu\lambda^2 \exp\left(\frac{\Delta E_j}{\mathrm{k}T}\right), \tag{5.23}$$

where λ is the average hopping distance. In combination with Eq. (5.19) and defining the inverse jump frequency

$$\tau_c^0 = \nu_0^{-1} \tag{5.24}$$

one gets the following expression for the correlation time:

$$\tau_c = \tau_c^0 \exp\left(\frac{\Delta E_j}{\mathrm{k}T}\right). \tag{5.25}$$

It is the time the atom spends in one location interacting with the local magnetic field, which is in agreement with Eq. (5.18). It can be identified with the avaerage time an atom spends at one location between two jumps or the inverse frequency of the oscillation at one location []. This form of the correlation time τ_c requires [Sch81] that $J(\omega_{ab})$ has the form [Bra, Pre]

$$J(\omega_{ab}) \propto \tau_c(\omega_{ab}\tau_c)^n, \tag{5.26}$$

where n is a constant, which is in agreement with Eq. (5.20) if $\omega\tau \gg 1$. Hence, the correlation time τ_c from Eq. 5.25 and the spectral density distribution $J(\omega)$ from Eq. (5.20) are both valid in the case of a Langmuir layer. The recombination measurements from Sec. 4.2 show that models based on the assumption of a Langmuir layer are able to describe the measured data, thus the functions introduced above are sufficient to study depolarization effects.

In addition to the above result, Memmert et al. [Mem88] and Scholl [Sch81] point out, that Eq. (5.20) is valid for the case of a three dimensional diffusion process, which might give restrictions on the use of the model. The diffusion of the atoms on the surface, which is the process that gives rise to the depolarizing Hamiltonian $\mathbf{H}_1(t)$, leads to a time dependence. It is determined by the conditional probability $P_d(\mathbf{r}_0, \mathbf{r}, t)$ that a spin located initially ($t = 0$) at $\mathbf{r}_0$ is located at $\mathbf{r}$ at a later time $t = t'$. This probability can be calculated by the diffusion equation. Further more the probability of an atom to return to $\mathbf{r}_0$ and be subjected to the same magnetic field as at $t = 0$ is

$$P_d(\mathbf{r}_0, \mathbf{r}_0, t') = (8\pi D t')^{-\frac{d}{2}}, \tag{5.27}$$

where d is the dimension of the system. Then the spectral density function for a two dimensional system is approximately given by

$$J(\omega_{ab}) = 2\tau_c \ln\left(1 + \frac{1}{\omega_{ab}^2 \tau_c^2}\right). \tag{5.28}$$

The difference in form of the spectral density functions of Eqs. (5.20) and (5.28) is important only in the low frequency range (low magnetic holding field) when $\omega\tau \ll 1$. In this case Equation (5.20) gives $J(\omega) \to \tau_c$ whereas Eq. (5.27) gives $J(\omega) \to \tau_c \ln(\omega^{-1}\tau_c^{-1})$, which was measured for surface diffusion [Mem88]. In the high frequency limit (high magnetic field), when $\omega\tau \gg 1$ and $J(\omega) \to \omega^{-2}\tau_c^{-1}$, both equations give the same. This is the case for the measurements presented here and Eq. (5.20) will be used in the following analysis.

The diffusion in a Langmuir layer is independent of the surface concentration just as in a two-dimensional gas. This point of view is correct if one assumes that the concentration gradient is the driving mechanism for the diffusion. But D. A. Reed and G. Ehrlich [Ree81] point out that the driving mechanism is the response to a gradient in the chemical potential of the adsorbed atoms. Their results indicate more complicated functions than Eq. (5.25) for the jump rate dependent on the surface concentration. On the other hand their results show that the functions for the jump rates in the different models do agree in the limiting cases of high coverage $\theta \approx 1$ and low coverage $\theta \approx 0$. This is the case for the data presented in the present work and the model of a Langmuir layer can be applied.

The results from the recombination measurements with the water covered cell show that in this case the assumption of a Langmuir layer is not valid. In addition, the interaction of the atoms with a second gas type adsorbed on the surface might have influence on the jump rate by affecting the energy ΔE_j and the correlation time τ_c.

The transition probability W_{ab} can now be calculated:

$$W_{ab} = c_b \cdot \gamma_S^2 b^2 |\langle b | S | a \rangle|^2 J(\omega_a b). \tag{5.29}$$

The constant c_b accounts for that part of the fluctuating field which is involved in the interaction. For a σ transition only parallel components and for a π transition the perpendicular components contribute to the interaction, hence $c_b = \frac{1}{3}$ in the case of a σ transition and $c_b = \frac{2}{3}$ in the case of a π transition. Since W_{ab} is the transition probability per unit time one gets

$$(\tau_{wc}^{-1})_{ab} = W_{ab}. \tag{5.30}$$

5.3 Measurements of the Polarization

Measurements of the polarization P^{BRP} were taken in combination with the measurements of the degree of dissociation α^{TGA}. The theoretical function for the polarization dependence on the temperature includes a variety of parameters. First, the polarization depends on the wall relaxation time τ_{wc}, which is proportional to the auto-correlation function $J(\omega_{ab})$ (Eqs. (5.29) and (5.30)). The transition probabilities for the electron (e) and proton transitions (n) are

$$W_{12} = W_{34} = \frac{2}{3}\gamma_S^2 b_e^2\, J(\omega_{12,34})\, \sin^2\theta, \tag{5.31}$$

$$W_{14} = W_{23} = \frac{2}{3}\gamma_S^2 b_n^2\, J(\omega_{14,23})\, \cos^2\theta, \tag{5.32}$$

where the frequencies are average frequencies of electron ($\omega_{14,23}$) and proton transitions ($\omega_{12,34}$) due to the hyperfine splitting energy at a field value of $B = 335\,\mathrm{mT}$. The constant values used in these formulas are

$$\begin{aligned}
\gamma_S &= 1.76 \cdot 10^{11}\,\mathrm{s^{-1}\,T^{-1}}, \\
\omega_{12,34} &\approx 4.451 \cdot 10^{9}\,\mathrm{s^{-1}}, \\
\omega_{14,23} &\approx 6.245 \cdot 10^{10}\,\mathrm{s^{-1}},
\end{aligned}$$

where γ_S is the gyro magnetic ratio of the electron. The interaction takes place by coupling to the electron. In the case of the states $|2\rangle$ and $|4\rangle$ the proton is effected by its coupling to the electron dependent on the magnetic field as expressed by $\sin^2\theta$ and $\cos^2\theta$, respectively. Thus the value of the fluctuating fields for both transitions is expected to be the same $b_e = b_n$. An additional difference in the relaxation times for electron and proton polarization is caused by a different magnitude in the correlation function $J(\omega)$.

As discussed in Sec. 4 there are two types of binding on the surface described by different binding energies. This results in different dwell times of the atoms on the surface and leads to a difference in the relaxation constant. The contribution of the two relaxation constants for both binding sites, which add up to the total relaxation constant, is determined by the evaporation rate $\mathcal{V}_{1,2}$ of the atoms for both types of sites (Eq. 4.19), which is calculated from the fitted values of the coverages of the two binding sites and the incident flux of atoms on the surface. The relative evaporation rates of atoms for CH- and PH-sites are

$$\tilde{\mathcal{V}}_i = \frac{\mathcal{V}_i}{\mathcal{V}_1 + \mathcal{V}_2}, \tag{5.33}$$

which are plotted in Fig 5.1 versus temperature. It is clear from the figure that the

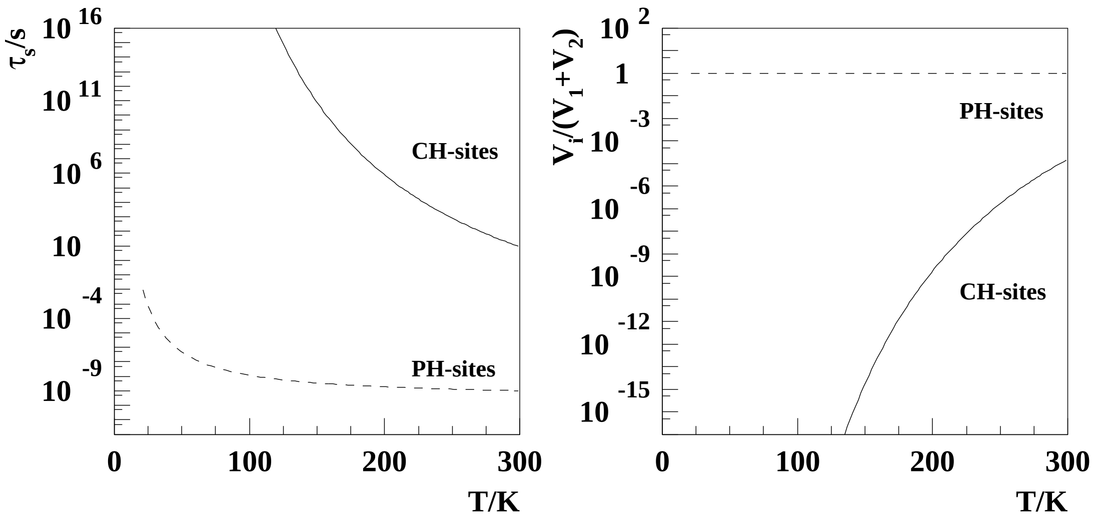

Fig. 5.1: Dependence of dwell time (Eq. (4.4), left) and relative flux (Eq. (5.33), right) from the surface on the cell temperature. The solid and dashed lines represent the calculated data for the CH- (i=1) and PH-sites (i=2), respectively.

evaporation of atoms from the CH-sites is much lower in comparison to the evaporation rate from the PH-sites at temperatures below room temperature. The high dwell time on the CH-sites leads to a small exchange rate of the atoms in that layer. The contribution of the atoms which evaporate from the CH-sites can be neglected in the calculation of the atom polarization inside the cell. Based on the results from Sec. 4.2 for the binding energy of the CH-sites the evaporation rate $\mathcal{V}_1$ can be used to calculate the average dwell time of the atoms on the CH-site using Eqs. (4.4) and (4.25). A fit to Fig 5.1, left, results in

$$\tau_s^0 = (1.0 \pm 0.2) \cdot 10^{-10}\,\mathrm{s}. \tag{5.34}$$

This quantity is the dwell time on the surface in the high temperature limit and applies for both types of site.

A measurement of the electron and nucleon polarization taken with the clean cell is shown in Fig. 5.2 as data points. The data was taken simultaneous with the recombination measurements from Sec. 4.2. The function from Eq. (3.25) for the polarization is fitted to the data and the values of the relevent parameters are

$$\begin{aligned} \tau_s^0 &= 1.0 \cdot 10^{-10}\,\mathrm{s}, & \tau_c^0 &= 2.5 \cdot 10^{-12}\,\mathrm{s}, & b_e &= 6.5\,\mathrm{mT}, \\ E_0 &= 0.0318\,\mathrm{eV}, & E_j &= 0.49 \cdot E_0, & b_n &= 6.5\,\mathrm{mT}, \end{aligned}$$

where b_e and b_n are the amplitudes of the fluctuating field for the electron and proton transitions, respectively. The field values b_e, b_n are fitted separately and yield the same value. The parameter E_0 is taken from the recombination data (Sec. 4.2). The calculated

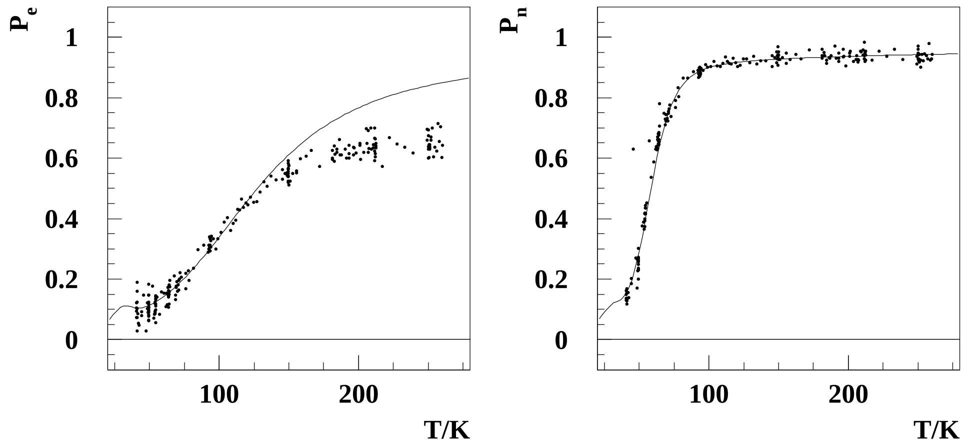

Fig. 5.2: Measured electron polarization (dots, left) and proton polarization (dots, right) versus cell temperature in an undamaged Drifilm coated cell. The solid lines show the functions for the electron and proton polarization calculated by Eq. (3.25).

functions for polarization agree well with the measurements. Above 150 K a change in the relaxation behavior in the electron polarization is observed, which cannot be explained by the present model.

The total relaxation rate γ_p is determined similar to Sec. 4.2 by simplifying Eq. (3.25). Again, the calculation of the ballistic term only leads to a shift of the data to lower values, but does not have an influence on the temperature dependence, Solving for γ_p gives

$$\begin{aligned} P^{\mathrm{BRP}} &= P(0)\frac{N_0^{-1}+\gamma_r}{N_0^{-1}+\gamma_r+\gamma_p}, \\ \Rightarrow \quad \gamma_p &= \left(\frac{P(0)}{P^{\mathrm{BRP}}}-1\right)\left(\frac{1}{N_0}+\gamma_r\right). \end{aligned} \tag{5.35}$$

It is obvious from the first equation that the measured polarization P^{BRP} shows a dependence on the recombination coefficient γ_r. It increases as soon as γ_r changes with the temperature to the same order of magnitude as N_0^{-1} or more. This effect is caused by the removal of the old atoms which have experienced the most depolarization because of their age. As a result the polarization at very low temperatures does not go down to zero although the relaxation probability γ_p increases at low temperatures (Fig. 5.2).

The relaxation rate γ_p, determined in this way, also includes the relaxation due to spin exchange collision. In principle the two relaxation rates can not be added up because they contribute in a non linear way. Since the spin exchange relaxation is weak (Sec. 5.2) the following approximation is used

$$\tilde{\gamma}_p = \left(\frac{\tau_s}{\tau_s + \tau_{wc}}\right) + \gamma_{se}, \tag{5.36}$$

where $\gamma_{se} = t_{res}/\langle b\rangle/\tau_{se}$ is the spin exchange relaxation during the time between two wall collisions and $\langle b\rangle$ is the average number of wall collisions an atom experiences inside the cell ($\langle b\rangle \neq N_0$).

The values for γ_p derived from Eq. (5.35) are plotted in Fig. 5.3, right. The spin relaxation is dominated by the spin exchange collisions for temperatures above 80 K and by the wall collision relaxation at temperatures below 80 K.

The left figure shows the contributions of the average dwell time τ_s and the wall relaxation time τ_{wc} to the relaxation probability per wall bounce. The relaxation time τ_{wc} includes the spectral density distribution $J(\omega)$ and the temperature dependence gives a maximum in the transition probability $W_{ab} \propto \tau_{wc}^{-1}$ at 40,K. Because of the strong increase in the dwell time the drop in the transition probability to lower temperatures is compensated and leads to a high γ_p. A separate measurement of the effect of spin exchange

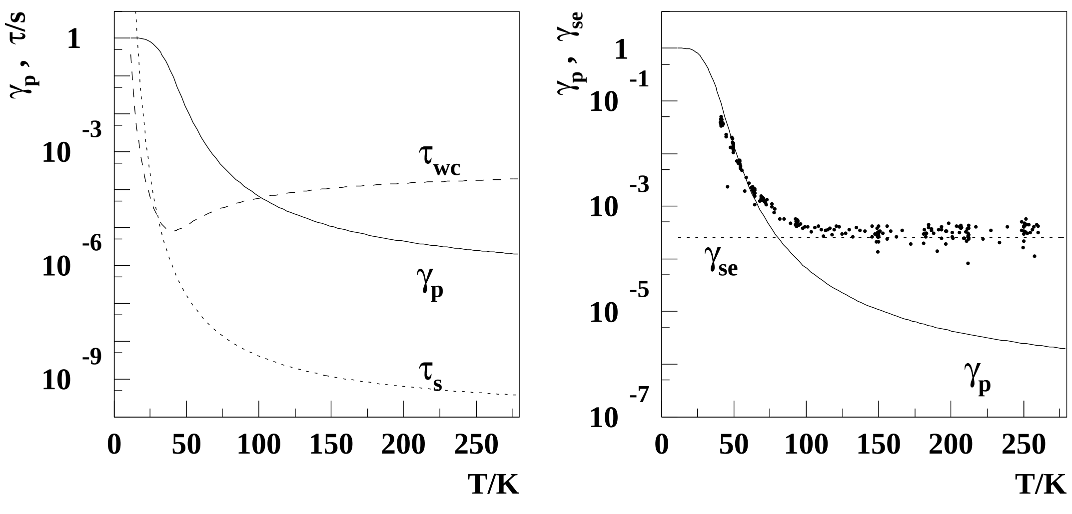

Fig. 5.3:
Relaxation times for wall collision (dashed line), dwell time (dotted line) and wall relaxation probability per wall collision (solid line) plotted versus temperature (left). On the right, the solid line represents $\gamma_p = \tau_s/(\tau_s + Tau_{wc})$ and the dotted line represents γ_{se}. The data points are calculated using Eq. (5.35).

collisions on the polarization is shown in Fig. 5.4, where the polarization dependent on the target density is plotted versus the nucleon flux measured by the TGA, which is a

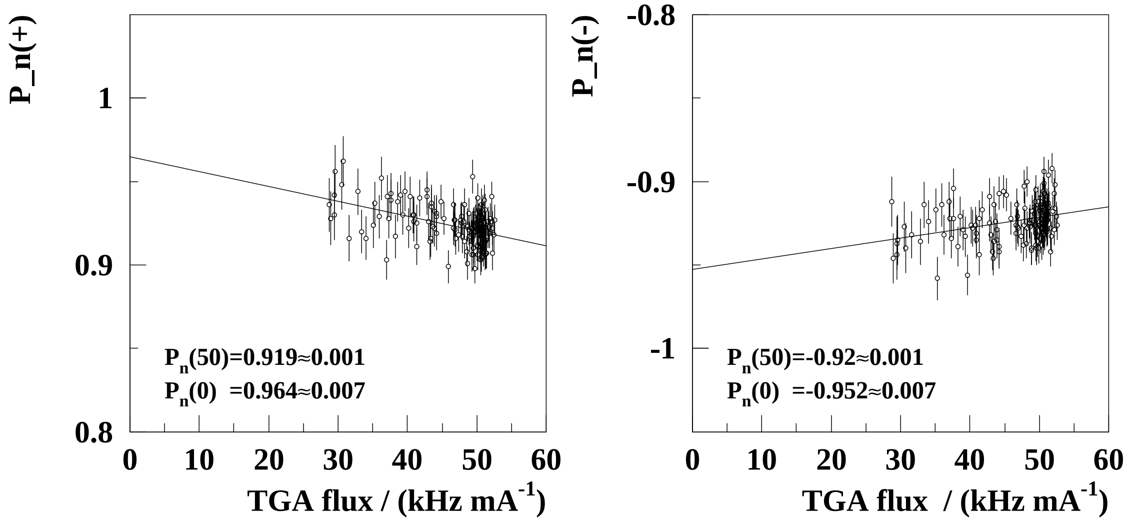

Fig. 5.4: Dependence of the Polarization on the target density. The polarization of injected states $|\,1\,\rangle$ and $|\,4\,\rangle$ (left) and injected states $|\,2\,\rangle$ and $|\,3\,\rangle$ (right) versus the TGA flux.

monitor for the target density. The linear extrapolation of the measured polarization to zero TGA flux shows an average difference in the polarization values due to spin exchange of $\Delta P = 0.375$, which is comparable with the expected value calculated in Sec. 5.1. On the other hand, the measurements also indicate that there is an additional polarization loss, which can not be explained by the present model. The extrapolation of the density to zero TGA flux shows a polarization of 0.96 without spin exchange. The expected wall relaxation in the measurement cannot account for this difference, which indicates an initial polarization of $P(O) < 1$ injected by the ABS.

5.4 The Water-Covered Cell

The measurement of the electron and proton polarization for a cell covered with water, corresponding to the recombination measurements in Sec. 4.3, are shown in Fig. 5.5. The cell has been exposed to the beam for 1 month and is partially covered with water and does not show a strong effect on the measured polarization in comparison to measurements with the clean cell. The parameters for γ_r from Sec. 4.3 are used as a parameterization for α. The following parameters are the result of a fit to the data shown in Fig. 5.5.

$$\begin{array}{rclrclrcl} \tau_s^0 &=& 1.0\cdot 10^{-10}\,\mathrm{s}, & \tau_c^0 &=& 4.0\cdot 10^{-12}\,\mathrm{s}, & b_e &=& 17\,\mathrm{mT}, \\ E_0 &=& 0.027\,\mathrm{eV}, & E_j &=& 0.35\cdot E_0, & b_n &=& 17\,\mathrm{mT}. \end{array}$$

The parameters for α are taken from Sec. 4.3.

A change in the relaxation probability is observed due to a change in the amount of water bound to the surface. The strongest change is found for the amplitude of the fluctuating magnetic fields, which increased from 6.5 mT to 17 mT indicating a change in the

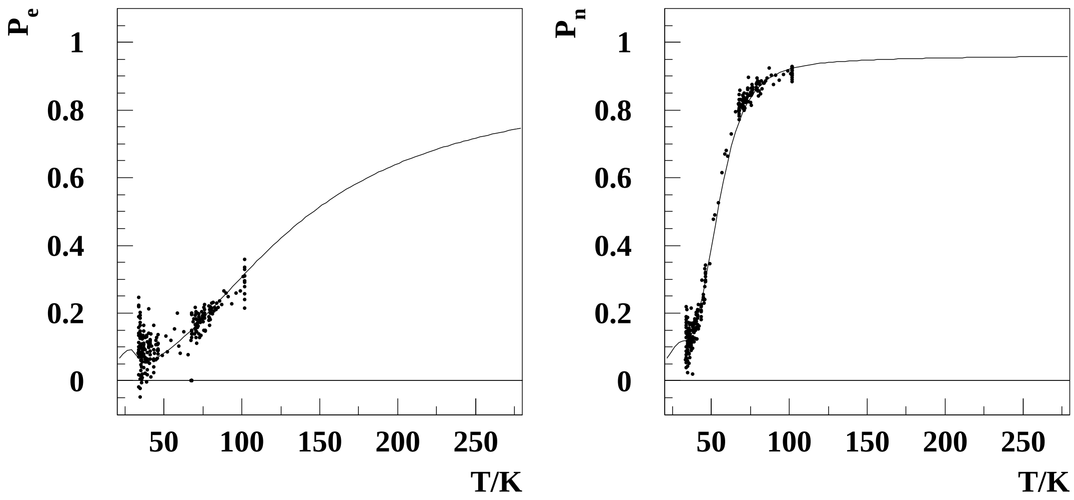

Fig. 5.5: Measured electron polarization (left) and proton polarization (right) versus cell temperature in an exposed cell. The solid line show the function calculated by the depolarization model explained in the text (see Fig. 5.2 for comparison).

interaction of the hydrogen with the surface or additional adsorbed species. The binding energy did not change significantly compared to the unexposed cell. The constants, which describe the diffusion process are also changed. The energy ΔE_j is lowered by 40% and the constant τ_c^0 increased by 60% resulting in a change of the relaxation time τ_{wc}, which increased due to the increase in b_n, at 100 K from $5 \cdot 10^{-5}$ to $2 \cdot 10^{-4}$, but remains small.

5.5 Polarization of the Atoms in the Target

Similar to Sec. 4.4, the calculation of the target polarization P_a^T is carried out using the age distribution $A_e(b)$ from Eq. (3.11) and the corresponding parameters for the cell. The calculation involves only the functions for the atoms inside the cell and no modification of Eq. (3.24) is needed.

A plot of the polarization in the BRP versus the calculated average polarization of the atoms in the cell P_a^T is shown in Fig. 5.6, left. In this case a uniform cell with a constant spin relaxation probability and two different recombination coefficients is assumed. It can be seen that for $\gamma_r \leq 0.005$ the polarization of the atoms inside the cell is equal or higher than the polarization in the BRP, which is an effect of the different age distribution of the atoms.

In the case of an nonuniform relaxation probability γ_p from Eq. (5.36) the result is similar to the non-uniformity in the recombination coefficient (Fig.5.6, right). The difficulty, which arises at this point, is to distinguish between a non-uniformity in the relaxation probability or the recombination coefficient, if none of the two quantities is

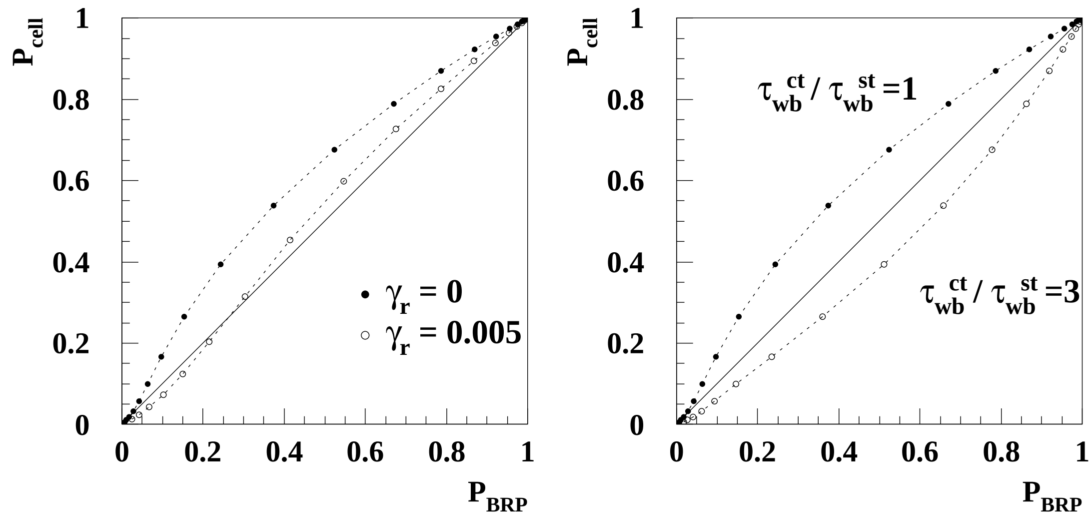

Fig. 5.6: Left picture: P^{BRP} versus P^{T} for a uniform cell with no recombination (dots) and a recombination coefficient of $\gamma_r = 0.005$ (open circles), for different values of γ_p. Right picture: P^{BRP} versus P_a^T for a uniform cell (dots) and non-uniform cell (open circles) with no recombination for different values of γ_p expressed by the wall relaxation times tau_{wb} for cell tube (ct) and sample tube (st).

measured separately. Both non-uniformities result in a similar change in the relation between P^{BRP} and P_a^T and further investigations are needed.

The correction on the BRP value can be written similar to Eq. (4.32) as

$$P^T = c^p \cdot P^{\mathrm{BRP}} \tag{5.37}$$

with c^p dependent on P and α.

6 Beam-Induced Resonant Depolarization Effects

Besides the depolarization due to wall relaxation, which can be overcome by a suitable wall coating, the intense transient magnetic field of the HERA positron beam bunches, transverse to the beam direction can cause a serious depolarization of the target atoms under certain conditions. The positron beam is bunched to provide high luminosity for the collider experiments and there are nominal 220 bunches circulating in the HERA positron ring. At a beam energy of 27.5 GeV the average beam current after injection is 35 mA. The high peak currents and the time structure of this beam lead to intense transient magnetic fields transverse to the beam direction, which have a typical peak value of 80 mT at a distance of 0.15 mm from the beam axis. The periodicity of these transient fields is seen by the hydrogen atoms moving with thermal velocity within the interaction region where there is a static holding field, which provides the quantization axis for the proton spins. This leads to depolarizing resonances at certain values of this field. There are a large number of closely spaced resonances in the usable range of holding field values. The holding field must therefore be rather uniform and the working point chosen carefully. The basic features of depolarizing resonances were calculated by Kinney [Kin91a, Kin91b, Kin93]. They gave the design criteria for the target holding field magnet.

6.1 Time Structure of the Positron Beam

The frequency spectrum of the perturbing field is the Fourier transform of the time structure of the positron beam field. Each bunch in the HERA ring, approximated by a Gaussian Distribution of the positrons in each direction, has a length of $\sigma_z = 8\,\text{mm}$ and an elliptical shape with $\sigma_x = 0.26\,\text{mm}$ and $\sigma_y = 0.07\,\text{mm}$. The revolution time of a single bunch at 27.5 GeV is T= 21.14 μs and the time interval between subsequent bunches is $\Delta t = 96\,\text{ns}$. The magnetic field of a single bunch is modified due to reflections at the beam tube. Thus the resulting bunch field is longer than the bunch length. A schematic of the time structure is given in Fig. 6.1.

A schematic of the Fourier transform of the beam is plotted in Figure 6.2. The frequency interval $\Delta\nu$ between the harmonics is $\Delta\nu = 10.4\,\text{MHz} = \Delta t^{-1}$. The shape function of the envelope Σ_ν is given by the average field of the single bunches Σ_t, which is approximated by a Gaussian function. The short length of the bunches leads to a large number N of harmonics. For an bunch length of $\sigma_z = 8\,\text{mm}$ the $1\sigma_\nu$ range of the envelope Σ_ν is expected at a frequency of $\nu = 6.0\,\text{GHz}$.

6.2 Resonance Condition

A periodic magnetic field may induce transitions between two sub-states $|\,a\,\rangle$ and $|\,b\,\rangle$, if the perturbation provides the transition (resonance) frequency ν_{ab}:

$$h\nu_{ab} = \Delta E_{ab}. \tag{6.1}$$

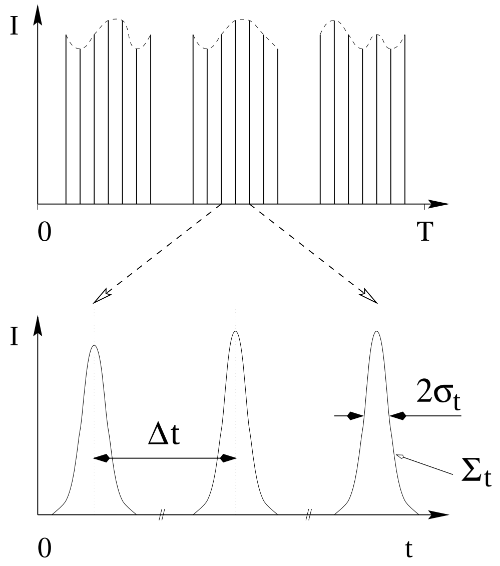

Fig. 6.1:
Upper: Schematic of the time structure of the positron beam. The beam current I is plotted versus time. Some of the buckets are left empty.
Lower: The time Δt between single bunches is 96 ns. The shape of single bunches is is approximated by a Gaussian function Σ_t of width σ_t.

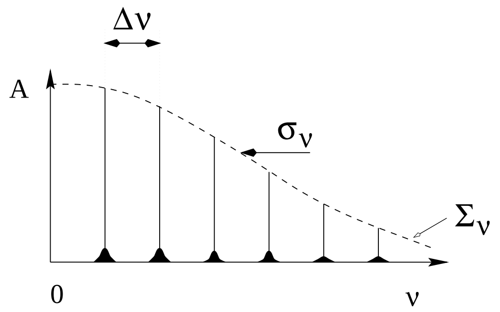

Fig. 6.2:
Schematic of the Fourier transform of the positron beam. The frequency of the harmonics is $\nu = k \cdot \Delta\nu$. The envelope Σ_ν is the Fourier transform of the field of the single bunches Σ_t, $\sigma_\nu = \sigma_t^{-1}$.

Because of the transverse direction of the perturbing fields relative to the holding field only π–transitions with $\Delta m_F = 1$ are allowed. These are

proton transitions: $|1\rangle \leftrightarrow |2\rangle$, $|3\rangle \leftrightarrow |4\rangle$, and
electron transitions: $|1\rangle \leftrightarrow |4\rangle$, $|2\rangle \leftrightarrow |3\rangle$.

In the strong field limit the transitions (1-2) and (3-4) change the proton polarization and the transitions (2-3) and (3-4) only the electron polarization. In a transverse holding field one has to consider in addition the σ transition $|2\rangle \leftrightarrow |4\rangle$ with $\Delta m_F = 0$, which changes both the electron and proton polarization.

The energy difference ΔE_{ab} between the hyperfine states is a non linear function of the magnetic field. It is plotted in Fig. 6.3 for transitions between the states $|1\rangle$ and $|4\rangle$, $|1\rangle$ and $|2\rangle$, and $|3\rangle$ and $|4\rangle$. The field values, where a beam harmonic leads to a resonance are shown schematically in the graph for both resonance types (1-2) and (3-4)and a realistic situation is shown in Fig. 6.4, upper graph.

The transition probability of a resonance depends on the hyperfine coupling coefficients and thus on the strength of the magnetic holding field. The square of the transition matrix element is proportional to $\sin^2\theta$ for the proton transitions and to $\cos^2\theta$ for the electron

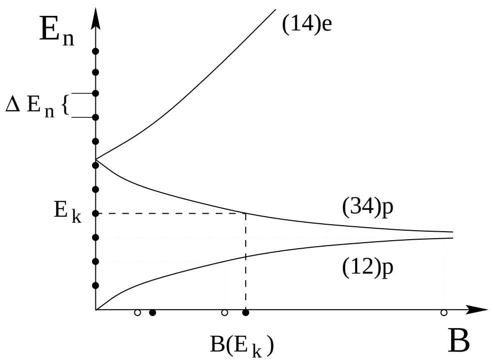

Fig. 6.3:
Schematic of the position of the harmonics versus holding field. The energy differences for the transitions (1-4), (1-2), and (3-4) are plotted. E_k is the energy value, where the harmonic k satisfies the condition $\Delta E_{ab} = kh \cdot \Delta\nu$.

transitions. The values B_k of the holding field B where the harmonic k of the transient field is resonant,

$$kh\Delta\nu_{ab} = E_a(B) - E_b(B) \tag{6.2}$$

are spaced by values $\Delta B_k = B_{k+1} - B_k$, which are inversely proportional to the above mentioned factors $\sin^2\theta$ and $\cos^2\theta$ for proton and electron transitions, respectively. Because of this spacing one expects, due to the low non-uniformity of the magnetic holding field, isolated depolarizing proton resonances ($\Delta B_{\mathrm{mag}} \ll \Delta B_k$) and a continuum of unresolved depolarizing electron resonances ($\Delta B_{\mathrm{mag}} \gg \Delta B_k$) at high holding field values.

6.3 Measurement Techniques

Two different techniques were used to observe the resonances.

- "Flip -in" measurements. In this technique the ABS and BRP are operated continuously. The RF transitions are chosen so that for ideal operation and in the absence of resonant transitions in the cell no intensity in the BRP detector is expected. Therefore the ABS injects sub-states $|1\rangle$ and $|4\rangle$ into the target cell and the MFT (1-3) transition is used in the BRP. The (1-2) or (3-4) proton resonance inside the cell depopulates the states $|1\rangle$ or $|4\rangle$, respectively. With the BRP MFT (1-3) transition[9] the injected sub-states $|1\rangle$ and $|4\rangle$ are removed from the detector acceptance. Only atoms, that experienced the bunch field resonances (1-2) or (3-4) in the cell contribute to the signal in the BRP, which is proportional to the strength of the resonance.

  injected BRP detector

$$\begin{pmatrix} n_1 \\ 0 \\ 0 \\ n_4 \end{pmatrix} \xrightarrow{\text{Reson.}:} \begin{pmatrix} n_1-\epsilon_1 \\ \epsilon_1 \\ \epsilon_4 \\ n_4-\epsilon_4 \end{pmatrix} \xrightarrow{\text{MFT13}} \begin{pmatrix} \epsilon_1 \\ \epsilon_4 \\ n_1-\epsilon_1 \\ n_4-\epsilon_4 \end{pmatrix} \xrightarrow{\text{Sextup.}} \begin{pmatrix} \epsilon_1 \\ \epsilon_4 \\ 0 \\ 0 \end{pmatrix}$$

[9]The MFT (1-3) transition is a two step transition, the transition (1-2) is followed by the transition (2-3). Both transitions occure at different positions inside the transition unit [Dre83, Bra95].

The advantage of this technique is the short time needed to obtain statistically relevant information. The data is obtained by scanning the magnetic field and gives information about the position and shape of the resonances.

- Polarization measurement. The BRP is operated to measure the occupation numbers $n_1 ... n_4$ of the sample. The polarization results as:

$$
\begin{aligned}
P_e &= n_1 - n_3 + (n_2 - n_4)\cos 2\theta, \\
P_z &= n_1 - n_3 - (n_2 - n_4)\cos 2\theta,
\end{aligned}
\tag{6.3}
$$

  with θ being the mixing angle defined by Eq. (1.9) This measurement requires a stable magnetic field for a single measurement and gives detailed information about the resonances inside the cell for different injected states from the ABS.

6.4 Measurements of the Proton Transitions

First measurements were taken at beam currents between 28 mA and 38 mA at beam energies of 27.5 GeV. During a scan of the magnetic field the H_1 signal in the BRP was measured with the RF transitions in the ABS and the BRP running continuously ("flip in"). The lower part of Fig. 6.4 shows the measured H_1 signal as a function of the current I_B of the magnetic field. The observed peaks are compared to the expected positions of the resonances calculated from the Fourier spectrum of the beam (upper part of Fig. 6.4). The position of the resonances are at the expected magnetic field values.

In a second measurement (Fig. 6.5) the proton and electron polarization of the hydrogen atoms were measured in the magnetic field range near the (1-2) resonance of the 62^{nd} harmonic of the beam, injecting again states $|1\rangle$ and $|4\rangle$, which are large proton polarization and no electron polarization. The measurements clearly indicate a change in the proton polarization caused by beam induced resonance (1-2) and, as expected, no polarization transfer from proton to electron is seen.

All measured resonances show a characteristic shape, which is the same for the (1-2) and (3-4) resonances. The widths of the resonances are proportional to their spacing. This indicates that the measured resonance shapes, which are measured dependent on the magnetic holding field, result from the broadening of an intrinsic resonance with width Γ_E. They are determined by the non uniformity of the magnetic holding field, the geometry of and the density distribution in the cell. The influence of these effects is discussed in the following.

6.4.1 Beam-Induced Resonances inside the Target Cell

The dependence of the amplitude B_{rf} of the bunch field on the distance from the beam is proportional to r^{-1} (Fig. 6.6). Hydrogen atoms passing this field in between two wall bounces experience depolarization if a resonance condition is met. The interaction time is proportional to the distance: A hydrogen atom with a trajectory of a short distance from

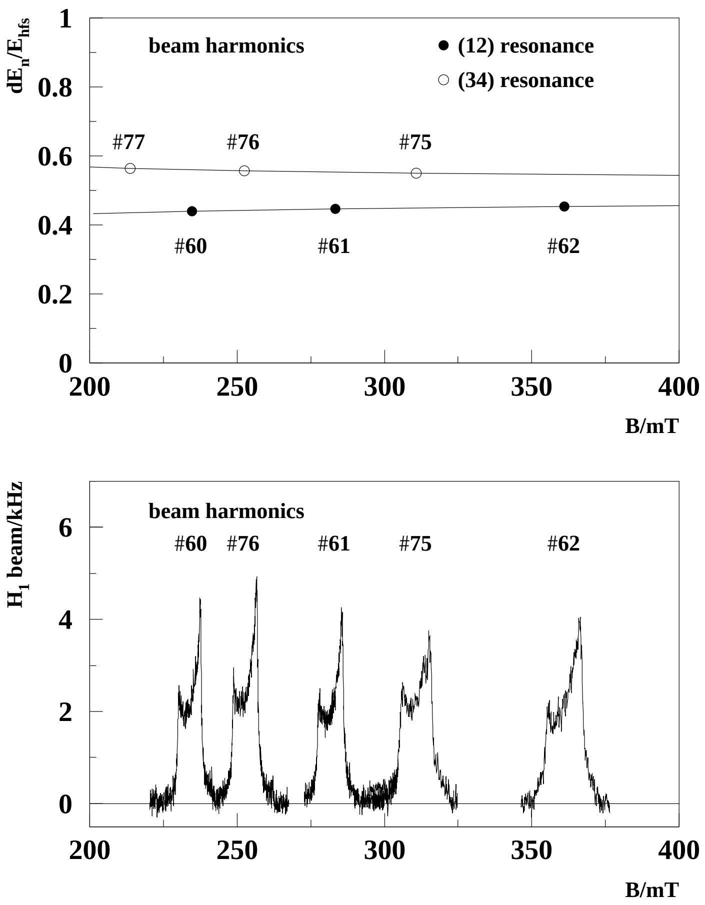

Fig. 6.4:
Upper graph:
The expected position of the resonances derived from the Fourier spectrum of the beam. The number of the beam harmonics is plotted next to the data points.
Lower graph:
Measured positions of the resonances versus the average magnetic field in the target cell. The HERMES operating point of $B = 335\,\mathrm{mT}$ lies in between two resonances.

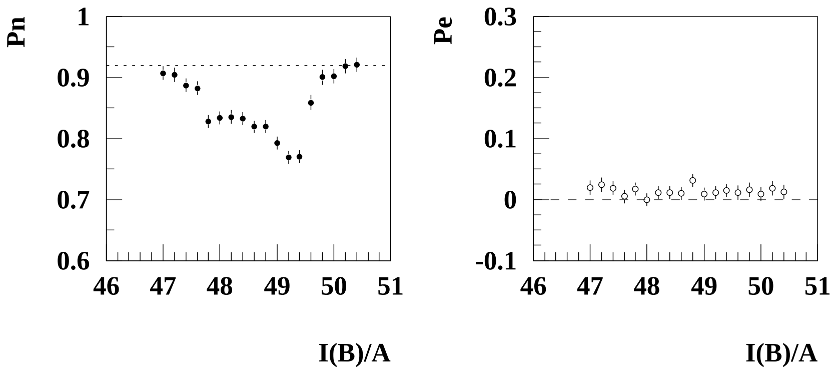

Fig. 6.5: Measured depolarization in the range of the 62$^{\mathrm{nd}}$ beam harmonic for injected states $|\,1\,\rangle$ and $|\,4\,\rangle$. The left picture shows the proton polarization, the right picture shows the electron polarization. ($B = 7.42 \cdot I_{\mathrm{mag}} \cdot \frac{\mathrm{mT}}{\mathrm{A}}$).

the beam is subject a interaction with a large transient field B for a short time whereas an atom with a trajectory at a longer distance is subject to weak interaction with a small transient field B for a long time. The width of the transition at short distance is much broader and therefore more dominant in the contribution to an intrinsic resonance spectral function, which includes the average over all trajectories in between two wall bounces in a given holding field. The depolarization (transition probability) is proportional to B^2 and weak. The depolarizations from subsequent passages of the resonant area in between the wall bounces are incoherent, thus they add up.

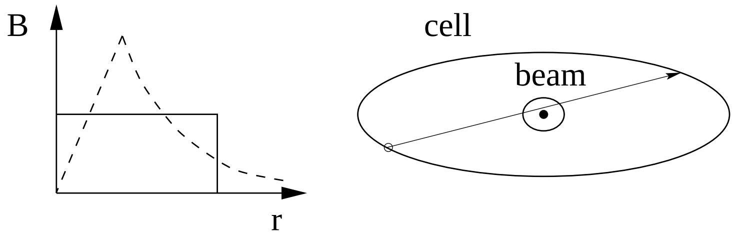

Fig. 6.6: Radial dependence of the perturbing field (dashed line, left). Approximation of the bunch field by a constant field value within a cylinder which is passed by the particle.

For simplicity one may approximate the bunch field by a constant value within a certain radius and by zero outside. Then the interaction between the gas particles and the perturbing field takes place inside a cylinder with a radius r_{int} along the beam axis. The thermal motion of the particles (Fig. 6.6, right) give a finite interaction time $2\tau = 2r_{\text{int}} v_{\text{th}}^{-1}$, which leads to an averaged intrinsic width $\Gamma_E = \hbar\tau^{-1}$ of the resonance with a spectral density distribution [Abr78] given by

$$\rho(\nu_{\text{rf}}, \nu(B(z)), \tau) = \frac{\tau}{\pi} \frac{1}{1 + (\nu_{\text{rf}} - \nu_{ab}(B(z)))^2 \tau^2}, \tag{6.4}$$

where ν_{rf} is the frequency of the perturbing field, k $\Delta\nu$, and $\nu_{ab}(B)$ is the frequency according to the energy gap between states $|\, a\,\rangle$ and $|\, b\,\rangle$ at the actual magnetic holding field B, which is a function of the position z and the magnet coil current I, $B = B(z, I)$. The transition probability W_{ab} between states $|\, a\,\rangle$ and $|\, b\,\rangle$ is then given by w

$$W_{ab}(\nu_{\text{rf}}, \nu(B(z)), \tau) = |\,\langle\, b\,|\,\mathbf{A}(S, I)\,|\, a\,\rangle\,|^2 \; \rho(\nu_{\text{rf}}, \nu(B(z)), \tau) \; \mathcal{F}_{e^+}(\nu_{\text{rf}})^2 \tag{6.5}$$

where $|\,\langle\, b\,|\,\mathbf{A}(S, I)\,|\, a\,\rangle\,|$ is the matrix element and $\mathcal{F}_{e^+}(\nu_{\text{rf}})$ is the calculated Fourier transform of the bunch field of the actually measured positron beam time structure.

For a given setting of the magnetic holding field current the magnetic field inside the cell shows a non-uniformity of $\frac{\Delta B}{B} = \pm 1.5\%$ (Fig. 6.7). The resonance condition for a certain frequency of the perturbing field is only met in a few and small areas Δz along the beam axis. The resonance condition appears locally inside the cell at different positions dependent on the holding field current. The spectral density distribution ρ of the resonance also depends on the position z inside the cell because the resonance frequency is field dependent and W_{ab} is, as a consequence, a function of position and magnet coil current, $W_{ab}(\nu_{\text{rf}}, z, I)$: By using the relation

$$\frac{1}{B_c} \mathrm{d}B = \sin^2\theta(B) \, \frac{1}{E_{\text{hfs}}} \mathrm{d}E \tag{6.6}$$

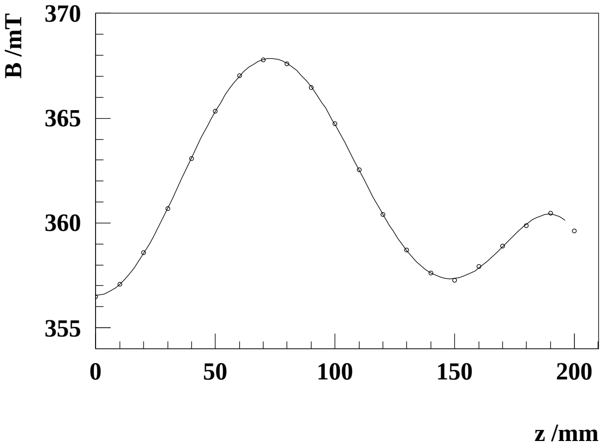

Fig. 6.7: Magnetic field map of the holding field. The dots show the measurements of the field along the cell axis. The center of the cell is at $z = 0\,\text{mm}$. The maxima at $z = 75\,\text{mm}$ and $z = 190\,\text{mm}$ correspond to the position of the magnet coils.

the spectral density function from Eq. (6.4) can be replaced in the calculation of the transition probability dependent on the position z by

$$\rho(\nu_{\text{rf}}, z, \Gamma_B) = \frac{1}{\pi} \frac{\Gamma_B}{\Gamma_B^2 + (B(\nu_{\text{rf}}) - B(z))}, \tag{6.7}$$

assuming a constant $\sin^2\theta(B)$ over the range of the magnetic field in the measurements .

The motion of the atoms inside the cell is diffusive and the rate measured by the BRP is in general proportional to the flux $\phi^d_{\text{bm}}(z)$ of atoms, that enter the interaction zone of the HERA beam, which is defined by the cylinder around the beam. The flux $\phi^d_{\text{bm}}(z)$ is proportional to the density $n(z)$ inside the cell. In addition, atoms are injected into the cell center from the ABS ballistically, which leads to an additional flux $\phi^b_{\text{bm}}(z)$ entering the interaction zone in the center of the cell in front of the injection tube. The total flux through the interaction zone is given by $\phi_{\text{bm}}(z) = \phi^b_{\text{bm}}(z) + \phi^d_{\text{bm}}(z)$ and is a step function near the center of the cell. The sampling probability $S(z)$ for a particle which crossed the beam at a certain z position is given by the probability for the particle to move back to the center of the cell since the BRP detects a sample of the particles, which enter the sample tube near the center of the cell. The sampling probability is linearly dependent on z. The product of the flux of atoms through the interaction zone and the sampling probability gives the sensitivity of the BRP of detecting a change in the proton polarization dependent on the position inside the cell. Because the density distribution $n(z)$ of the target gas also shows a linear dependence on z, the total sensitivity of the BRP is proportional to z^{-2}.

For polarized gas the measured polarization in the BRP is given by

$$P_{\text{meas}} = P_0 \cdot (1 - R), \tag{6.8}$$

where P_0 is the measured polarization in the absence of the HERA beam and R is a function, which describes the beam induced polarization loss measured by the BRP. The function R is calculated by multiplying Eq. (6.8) with the weight functions $S(z)$ and $\phi_{\mathrm{bm}}(z)$ and integrating along the cell and over all frequencies of the perturbing field

$$R = \frac{1}{N} \int_0^\infty \int_{\mathrm{cell}} W_{ab}(\nu_{\mathrm{rf}}, z, I)\ \phi_{\mathrm{bm}}(z)\ S(z)\ dz\ d\nu_{\mathrm{rf}}, \tag{6.9}$$

where N is a normalization constant. Fit parameters are the ratio of the fluxes $\phi^d_{\mathrm{bm}}(z)$ and $\phi^b_{\mathrm{bm}}(z)$, the width of the resonance Γ_B and the value of N. The resulting function is plotted in Fig. 6.8. P_{meas} and R are functions of the magnet current, therefore $P_{\mathrm{meas}}(I)$ and $R(I)$ are used. The function shows good agreement with the measured data and the

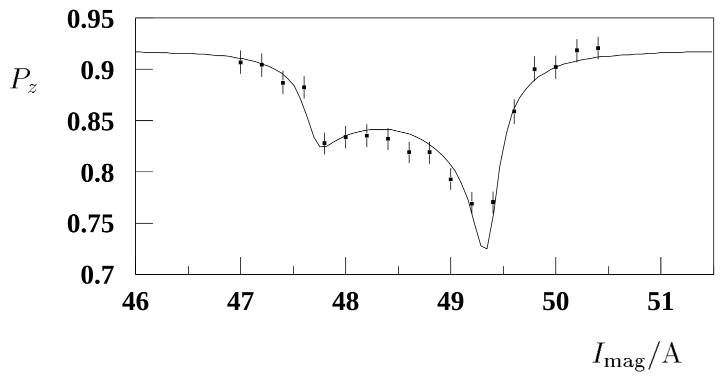

Fig. 6.8:
Measured polarization versus magnetic field for the (1-2) resonance at the 62$^{\mathrm{nd}}$ beam harmonic. The solid line represents the calculated depolarization due to the resonance according to Eqs. (6.9) and (6.13) ($B = 7.42 \cdot I_{\mathrm{mag}} \cdot \frac{\mathrm{mT}}{\mathrm{A}}$).

following parameters are obtained:

$$\begin{aligned} \Gamma_B &= 1.19\,\mathrm{mT}, \\ \phi^b_{\mathrm{bm}}(z=0) &= 1.05\,\phi^d_{\mathrm{bm}}(z=0). \end{aligned} \tag{6.10}$$

The two dips in the measured resonance are related to the maxima and minima of the holding field inside the cell, where the dip at high magnet currents is related to the minimum field value.

The intrinsic resonance width Γ_E is related to Γ_B by Eq. (6.6) and can be used to calculate the interaction time of the particles with the perturbing field

$$\Gamma_E = 6.96 \cdot 10^{-10}\mathrm{eV} \Rightarrow \tau = \frac{\hbar}{\Gamma_E} = 9.8 \cdot 10^{-7} s. \tag{6.11}$$

Assuming thermal velocity of the atoms at 100 K this gives an interaction path length of $l_{\mathrm{int}} = 2.5\,\mathrm{mm}$. Perpendicular to the beam axis this interaction path length is much longer than the average beam diameter of 0.15 mm, and shorter than the minimum cell diameter of 10 mm. Parallel to the beam axis the interaction path length is given by the product of Γ_B and the inverse magnetic field gradient $\mathrm{d}B/\mathrm{d}z$. The minimum and maximum interaction path lengths are found at the positions of maximum and minimum field gradient, respectively. The resulting minimum and maximum interaction path lengths along the beam axis for an average holding field value of 361 mT and a resonance width $\Gamma_B = 1.19\,\mathrm{mT}$ are obtained from Fig. 6.7:

$$\begin{aligned} l_{\min(z)} &= 6\,\mathrm{mm} \text{ and} \\ l_{\max(z)} &\approx 45\,\mathrm{mm}, \end{aligned} \tag{6.12}$$

where $l_{\max(z)}$ is a factor of 18 larger than l_{int}.

The fraction of the beam axis, which is inside the resonance width Γ_B, is 15%, if the resonance condition is met at the maximum holding field value (Fig. 6.8, $I_{\mathrm{mag}} = 49.3\,\mathrm{A}$). The atoms undergo multiple crossings of the interaction region while they reside inside the cell and the average polarization loss of the atoms per crossing is less than 3%.

It should be noted at this point, that the good agreement of the function R from Eq. (6.9) with the experimental data shows that the particle samples of atoms inside the cell and atoms detected by the BRP are not separated as assumed in the calculation of the age distributions, because the function R includes the detection probability $S(z)$. The consequences are discussed in Chapter 7.

6.5 Measurements of the Electron Transitions

The transition strength of the electron resonances, e.g. (1-4), depends on much higher Fourier components of the bunch field (Fig. 6.1). In the range of the holding field B from 0 to 350 mT the order k of the resonant harmonics goes from 137 to 1015 for the (1-4) resonance and from 1 to 879 for the (2-3) resonance. The distance between two field values of resonances depends on the magnetic field as $\cos\theta^2$. Because of their narrow spacing and the non-uniformity of the holding field inside the cell they cannot be resolved in the measurements of the BRP. At the critical field $B = 50.7\,\mathrm{mT}$ the distance in terms of the magnetic field is 0.38 mT whereas the field non-uniformity of the magnet is $\Delta B = \pm 0.8\,\mathrm{mT}$, which yields four resonance conditions for each electron resonance within the field non-uniformity. An increase in the holding field value leads to an increase of the number of resonance conditions within the field non-uniformity. Due to the change in the field gradient the density of the resonant area inside the cell remains constant. The $\cos^2\theta$ dependence of the transition probability and the spacing of the resonances result in a $\cos^4\theta$ dependence on the total transition strength. The following functional dependence of the resonance strength is expected with the assumption of a Gaussian shaped bunch field strength distribution:

$$R_e(B) \propto \cos^4\theta(B) \left(\frac{1}{\sqrt{2\pi}\,\sigma_B} \exp\left(-\frac{B^2}{2\sigma_B^2} \right) \right)^2 . \tag{6.13}$$

A first measurement of the electron resonances, using the flip-in technique similar to the proton measurements, was performed with an atomic hydrogen beam of states 1 and 2 injected in the cell and both the transitions SFT14 and MFT23 in the BRP active. The remaining signal in the BRP detector is proportional to the interchange of the states

$|1\rangle$ and $|4\rangle$ and states $|2\rangle$ and $|3\rangle$ due to the resonances. By defining the variable η dependent on the occupation numbers n_i, but independent on the magnetic field

$$\eta = (n_1 + n_2) - (n_3 + n_4) \tag{6.14}$$

any electron resonance will reduce the value for η. The occupation numbers are also affected by wall relaxation and spin exchange collisions. To separate the relaxation processes from the observed resonances two measurements were performed, one without the positron beam η_0 and the second with the positron beam η_{e+}. The ratio η_{e+}/η_0 is then proportional to the strength of the beam induced resonances and only weakly dependent on the relaxation processes. A plot of η_{e+}/η_0 versus the magnetic field is shown in Fig. 6.9

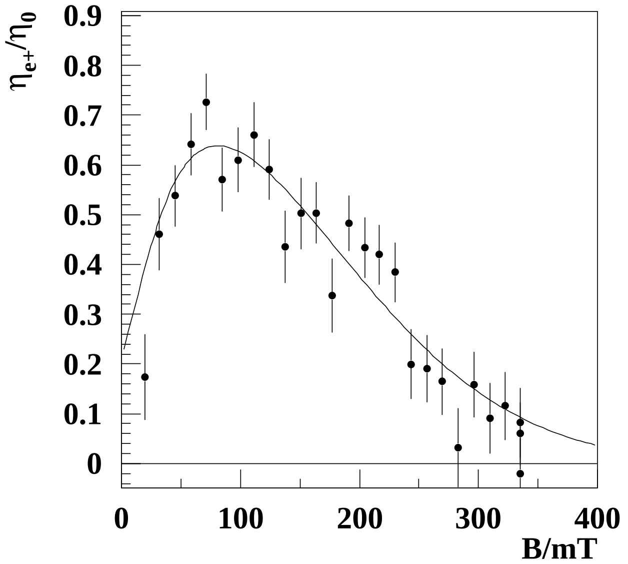

Fig. 6.9:
Measurement of the electron resonances. The measured ratio η_{e+}/η_0 for the measurements with and without positron beam is plotted as function of the target magnetic field.

for values of the magnetic field $B = 0\,\mathrm{mT}$ to $335\,\mathrm{mT}$. The maximum polarization loss is 64% at 100 mT, stronger than the observed polarization loss of the protons. The solid line represents a fit of the function from Eq. (6.13) to the data with the parameter

$$\sigma_B \quad = \quad (244 \pm 8)\,\mathrm{mT},$$

and $\chi^2 = 1.3$. Since the number of beam harmonics k_e for the electron transitions show a linear dependence on B for values of $B > B_c$ and k_e is determined by the equation $k_e \Delta\nu/\nu_{\mathrm{hfs}} = BB_c$ the value σ_B can be translated into a frequency

$$\sigma_\nu = \nu_{\mathrm{hfs}} \frac{\sigma_B}{B_c} = (6.85 \pm 0.23) \cdot 10^9 Hz \tag{6.15}$$

and the relations $\sigma_t = (2\pi\sigma_\nu)^{-1}$ and $\sigma_z = v_c \cdot \sigma_t$ (v_c speed of light) give the length of the field of the positron bunches

$$\begin{aligned} \sigma_t &= (23.3 \pm 0.8)\,\mathrm{ps}, \\ \sigma_z &= (0.70 \pm 0.02)\,\mathrm{cm}. \end{aligned} \tag{6.16}$$

This number can be compared to the theoretical length of the positron bunches of $\sigma_z =$ 0.8 cm at a beam energy of E_{e^+}=27.5 Gev.

The data in Fig. 6.9 show that the amplitude of the transient field at high magnetic holding field is small and a depolarization of the electron polarization during run of the experiment is also small. The observed depolarization of the electrons shown in Fig. 1.5 occurred only during injection and show a dependence on the beam energy. The length of the bunches depends on the energy of the beam as

$$\sigma_z(E_{e^+}) = \text{const.} \cdot E_{e^+} + \sigma_z(0), \tag{6.17}$$

which leads to the observed effect, that the electron resonances disappear after the energy of the positron beam is ramped to full energy.

7 Target Polarization

Knowledge of the target polarization is essential for the HERMES experiment, it enters directly into the determination of the asymmetries at HERMES. In addition to the polarization of the atoms, the polarization of the molecules formed by recombined atoms which remain in the target cell, affect the determination and need to be known. Measurements sensitive to the polarization of the molecules were taken at HERMES and will be discussed in the following section. A small amount of unpolarized molecular hydrogen, which does not result from the recombination of atoms enters into the cell from different sources. Other contents of the target than atomic or molecular hydrogen could not be detected during normal operation. The HERMES polarized hydrogen target is in this respect a dilution free target. A formula for target polarization taking all the contributions mentioned above into account will be discussed in the following. Additional information about the degree of dissociation and polarization can be gained using the luminosity monitor of the experiment, which measures coincident pairs of elastic scattered electrons and positrons (Bhabha scattering). The measurements with the luminosity monitor are sensitive to the integrated areal densities of electrons of atomic and molecular hydrogen in the target cell. A comparison of those measurements to the TGA and BRP measurements gives information about the corrections which have to be applied with respect to the degree of dissociation and polarization.

In the first two sections the averaged target polarization is defined based on the measurements of polarization and degree of dissociation of BRP and TGA, respectively. The next section presents a method to determine the degree of dissociation in the target cell, which combines the TGA and the luminosity monitor measurements. In Sec. 7.4 the polarization of the molecules is discussed. First, the expected polarization of the adsorbed atoms on the surface is discussed in the frame work of the recombination and relaxation models presented in Chaps. 4 and 5. Second, a preliminary measurement of the polarization of the molecules resulting from high and low α^T measurements is presented.

7.1 Formula for the Target Polarization

The averaged target polarization P^T is defined based on the entirety of all nucleons inside the target cell. Measurements exist for the polarization of the atoms and the degree of dissociation of a sample leaving the sample tubes. Besides the recombination of atoms there are two sources for molecules, which enter the target cell. The first one is the ballistic flow of undissociated molecules from the ABS dissociator into the target cell. The second source are molecules from the rest gas of the target chamber reentering the cell. The polarization of both groups of molecules is zero. In addition to the different contributions of molecules and atoms, the density distributions of the nucleons inside the cell give weight on the calculations. The polarization of the molecules from recombined atoms cannot be measured during the experiment and requires an additional measurement, which will be discussed later.

The HERA positron beam is sensitive to the total number of nucleons integrated along the cell axis. This allows calculation of the target polarization based on the average polarization of the atoms and the average degree of dissociation of the nucleons inside the cell. The formula for computing the target polarization then is

$$P^T = \alpha_0^T \left(\alpha_r^T P_a^T + (1 - \alpha_r^T)\, P_m^T \right). \tag{7.1}$$

The index T indicates the average over the target cell. Using the target thickness d^T, which is defined as the integrated areal target density

$$d^T = \int_{cell} n(z) dz, \tag{7.2}$$

the α values are then defined as

- α_0^T, the number of nucleons inside the cell which originate from injection into the cell as atoms divided by the total number of nucleons inside the cell, and
- α_r^T, the number of nucleons in atoms divided by the number of nucleons which originate from injection into the cell as atoms:

$$\alpha_0^T = \frac{d_p^T}{d_p^T + d_u^T} \quad \text{and} \quad \alpha_r^T = \frac{d_a^T}{d_a^T + d_r^T}. \tag{7.3}$$

The terms $d_{p,u}^T$ are defined as integrated nucleon areal densities in atoms or molecules, which entered the cell as

d_p^T : atoms (polarized),
d_u^T : molecules from background sources (unpolarized),

and the terms $d_{a,m}^T$ are defined as the integrated nucleon areal densities in atoms or molecules, which entered the cell as atoms and

d_a^T : remain as atoms,
d_r^T : recombine inside the cell.

The polarizations P_a^T and P_m^T are defined by the spin states of the nucleons in the atoms or recombined molecules, parallel (+) or anti-parallel (−) to the magnetic holding field inside the cell:

$$P_a^T = \frac{d_a^{T(+)} - d_a^{T(-)}}{d_a^{T(+)} + d_a^{T(-)}} \quad \text{and} \quad P_m^T = \frac{d_r^{T(+)} - d_r^{T(-)}}{d_r^{T(+)} + d_r^{T(-)}}. \tag{7.4}$$

7.2 TGA measurements of the Degree of Dissociation

The measurements of the degree of dissociation are carried out with the TGA. The TGA detects atoms and molecules, which have left the cell, and is sensitive to nucleon flow rates. The measurements of the TGA, which are based on particles flow rates, need to be related to the quantities of atoms and molecules inside the cell. The total sum of the flow rates of atoms and molecules does not change due to the recombination process, whereas the atoms, which recombine to molecules inside the cell, cause a change in the total nucleon density of the target. The values for α_0^{TGA} and α_rTGA measured by the TGA need to be corrected to obtain the respective values for the target.

The total flow rate into the cell consists of the ABS atomic flow rate, the ABS flow rate of ballistic molecules, and the rest gas flow rate of molecules. The TGA measures relative nucleon flow rates for particles mass 1 and 2 (Sec. 2.4), which leave the sample tubes of the cell. These flow rates can be put in relation to a total nucleon flow rate through the cell, which is not dependent on the temperature of the cell. A nucleon flow rate into the cell Φ^c can be put in relation to a nucleon density n^c in the cell center

$$n^c = \frac{\Phi^c}{C_c}, \tag{7.5}$$

where C_c is the cell temperature dependent conductance of the cell. The different α terms can be expressed in terms of TGA flow rates of atoms and molecules, which are accordingly related to a density of atoms and molecules in the cell center. In the following the subscripts 'a' and 'r' are used as in Eq. (7.4) and the subscripts 'bal' and 'rg' are related to the ballistic flow and rest gas flow, respectively. Similar to α^{TGA} from Sec. 2.4 the value of α_0^{TGA} is

$$\alpha_0^{\mathrm{TGA}} = \frac{\Phi_a^{\mathrm{TGA}} + \Phi_r^{\mathrm{TGA}}}{\Phi_a^{\mathrm{TGA}} + \Phi_r^{\mathrm{TGA}} + \Phi_{\mathrm{bal}}^{\mathrm{TGA}} + \Phi_{\mathrm{rg}}^{\mathrm{TGA}}}. \tag{7.6}$$

and gives information about the number of nucleons detected by the TGA, which originate from injection as atoms. A calculation of the average target values of α_0^T include the correction of the measured flow rates for the density distribution of the nucleons along the cell. The density n_{bal}, caused by the ballistic flow rate from the ABS, always has a triangular shaped distribution along the cell and is used as a reference distribution. The value of reference is its density in the center and the correction factor is set to 1. The density n_{rg} is uniformly distributed along the cell and the correction factor for the density in the center compared to a triangular shaped distribution is 2. The density distribution of the sum of densities $n_a + n_r$ depends on the recombination inside the cell which is expressed by a factor $k_0 \in [1, \sqrt{2}]$ (Eq. (4.31)) and α_0^T is given by

$$\alpha_0^T = \frac{k_0(\Phi_a^{\mathrm{TGA}} + \Phi_r^{\mathrm{TGA}})}{k_0(\Phi_a^{\mathrm{TGA}} + \Phi_r^{\mathrm{TGA}}) + \Phi_{\mathrm{bal}}^{\mathrm{TGA}} + 2 \cdot \Phi_{\mathrm{rg}}^{\mathrm{TGA}}}. \tag{7.7}$$

A correction due to the finite density at the cell ends, which is not included in the above calculation, is small. The correction on α_0^{TGA} due to the density distribution inside the cell and the measured ballistic and restgas flow rates can be described by a correction factor $\tilde{c}_0^{\alpha}$:

$$\alpha_0^T = \tilde{c}_0^{\alpha} \cdot \alpha_0^{\mathrm{TGA}}. \tag{7.8}$$

The degree of dissociation α_r^{TGA}, the fraction of the injected atoms, which remain as atoms, is given by

$$\alpha_r^{\mathrm{TGA}} = \frac{\Phi_a^{\mathrm{TGA}}}{\Phi_a^{\mathrm{TGA}} + \Phi_r^{\mathrm{TGA}}} \tag{7.9}$$

and, α_r^T is given by

$$\alpha_r^T = \tilde{c}_r^{\alpha} \frac{\Phi_a^{\mathrm{TGA}}}{\left(\Phi_a^{\mathrm{TGA}} + \Phi_r^{\mathrm{TGA}}\right)}, \tag{7.10}$$

where the correction factor $\tilde{c}_r^{\alpha} = c_r^{\alpha}/k_0$ (see Eq. (4.32)) describes the correction on α_r^{TGA} due to the density distribution of the molecules inside the cell and a possible difference in the recombination coefficients in cell and sample tube.

7.2.1 Measurement of the Rest Gas Flow Rate

The measurement of the rest gas flow rate was carried out using a gas feed line which injects molecular hydrogen into the target chamber. The gas flow is adjusted to different pressures in the target chamber, which are in the order of the pressure during normal run of the ABS. The hydrogen gas distributes inside the chamber and enters the target cell. Once a state of equilibrium is reached the pressure inside the target cell is equal to the chamber pressure. The conductances of the feed and sample tubes are small compared to the conductances of the beam tube and the density of the gas inside the cell is uniformly distributed. The gas flow leaving the sample tubes is measured by the TGA dependent on the chamber pressure p^{TC}. The measurements were reproduced over a years time and one obtains the following dependence of the restgas flow rate on the target chamber pressure:

$$\Phi_{\mathrm{rg}}^{\mathrm{TGA}} = -0.0159\,\mathrm{kHz\,mA^{-1}} + p^{TC} \cdot 3.384 \cdot 10^{6}\,\mathrm{kHz\,mA^{-1}\,mbar^{-1}} \tag{7.11}$$

measured as count rate in the TGA divided by emission current of the QMS detector. The error is dominated by the uncertainty in the pressure readout of $\Delta p^{TC}/p^{TC} = 0.1$ and the resulting error in the determination of the restgas flow rate is $\Delta\Phi_{\mathrm{rg}}^{\mathrm{TGA}}/\Phi_{\mathrm{rg}}^{\mathrm{TGA}}$ =0.1. For typical values of the target chamber pressure of $p^{TC} = 1.6 \cdot 10^{-7}$ mbar one obtains a TGA rest gas flow rate of 0.53 kHz mA^{-1}. The contribution of the rest gas flow rate to the TGA total flow rate which is about 1% of the measured total TGA flow rate (sum of atomic and molecular flow rate) of 50 kHz mA^{-1} and the contribution to the total target is 2%.

7.2.2 Measurement of the Ballistic Molecule Flow Rate

The flow rate of ballistic molecules from the ABS detected by the TGA can be measured by a combination of two ABS modes, 'ahx' and 'ehx' (Tabs. 2.1 and 2.8), which inject different intensities into the cell: In 'ahx' mode the ABS injects two hyperfine substates but only one in 'ehx' mode, which results in different intensities, but the ballistic flow of molecules from the ABS remains constant. Defining $\Phi_{\mathrm{tot}}^{\mathrm{TGA}}$ as the sum of the flow rates of mass 1 and mass 2 measured by the TGA, Eq. (7.9) gives the following equation, which is satisfied in each measurement mode of the ABS e.g. 'ahx' or 'ehx':

$$\frac{\Phi_{\text{tot}}^{\text{TGA}} - \Phi_{\text{rg}}^{\text{TGA}} - \Phi_{\text{bal}}^{\text{TGA}}}{\Phi_{a}^{\text{TGA}}} = \frac{1}{\alpha_r^{\text{TGA}}}, \tag{7.12}$$

The measured rates from the modes 'ahx' and 'ehx' can be combined, if α_r^{TGA} yields the same value and the terms dependent on α_r^{TGA} cancel. Solving for $\Phi_{\text{bal}}^{\text{TGA}}$, which is the same in both measurement modes gives

$$\Phi_{\text{bal}}^{\text{TGA}} = \frac{(\Phi_{\text{tot}}^{\text{TGA}} - \Phi_{\text{rg}}^{\text{TGA}})_{\text{ehx}}(\Phi_{a}^{\text{TGA}})_{\text{ahx}} - (\Phi_{\text{tot}}^{\text{TGA}} - \Phi_{\text{rg}}^{\text{TGA}})_{\text{ahx}}(\Phi_{a}^{\text{TGA}})_{\text{ehx}}}{(\Phi_{a}^{\text{TGA}})_{\text{ahx}} - (\Phi_{a}^{\text{TGA}})_{\text{ehx}}}. \tag{7.13}$$

The restriction of equal α_r^{TGA} values gives only a small error in the limit $\alpha_r^{\text{TGA}} \to 1$ with alternating measurement modes 'ahx' and 'ehx'. The ballistic flow rate was measured at a constant input of $1.25\,\text{mbar}\,\text{l}\,\text{s}^{-1}$ into the ABS dissociator and one obtains a ballistic flow rate of

$$\Phi_{\text{bal}}^{\text{TGA}} = (0.470 \pm 0.115)\,\text{kHz}\,\text{mA}^{-1} \tag{7.14}$$

measured as count rate in the TGA divided by emission current. The measured degree of dissociation for both measurement modes was $\alpha^{\text{TGA}} \approx 0.97$ and the approximation of an equal degree of dissociation is true. At a typical value of the total TGA flow rate of $50\,\text{kHz}\,\text{mA}^{-1}$ the contribution of the ballistic flow rate to the TGA total flow rate and total target is about 1%.

7.3 Measurement of the Degree of Dissociation using the Luminosity Monitor

The luminosity monitor measures coincident pairs of elastic scattered electrons and positrons (Bhabha scattering). The measured count rates of the luminosity monitor are proportional to the target thickness d_{el}^T of the electrons in the target gas. At the HERMES target, the electron density equals the nucleon density, where the target thickness of the electrons and nucleons is equal $d^T = d_{el}^T$. Since a change in the recombination coefficient changes the number of nucleons inside the storage cell the luminosity measurement can be used to measure the degree of dissociation inside the storage cell. For this purpose the rates N_L need to be normalized by a reference value of α^T and the target thickness. The target thickness depends on the input flow rate from the ABS and the cell temperature thus a normalization includes both quantities. In a first step the rates N_L can be related to the TGA flow rate by applying a similar normalization as in the case of the TGA rates (Sec. 2.4). In the second step a calibration measurement is defined, which in combination with the normalized rates yields an expression, which is proportional to the degree of dissociation of the total target. The following calculation does not include the molecules from restgas or ballistic flow. An expansion of the calculation including the case where the restgas and ballistic flow contribute to the target is given once the formalism is established.

The dependence of the luminosity monitor rates N_L on the experiment parameters is

$$N_L \propto \frac{I_{e+}}{\mathrm{e}}\, d^T \int\limits_{\Delta\Omega} \left(\frac{\mathrm{d}\sigma}{\mathrm{d}\Omega}\right)_{\mathrm{bha}} \mathrm{d}\Omega \tag{7.15}$$

where I_{e+}/e is the HERA beam positron rate, $\Delta\Omega$ is the acceptance of the luminosity monitor and $\left(\frac{\mathrm{d}\sigma}{\mathrm{d}\Omega}\right)_{\mathrm{bha}}$ is the Bhabha scattering differential cross section. The total target thickness can be put in relation to the TGA flow rate measurement in the following way. In the case of recombination inside the cell the flow rate of atoms and molecules add up to the total flow rate

$$\Phi_{tot}(z) = \Phi_1(z) + \Phi_2(z) = \mathrm{const.} \tag{7.16}$$

The total flow rate through the cell is constant along the cell position and proportional to the ABS flow rate $\Phi_{tot} \propto \Phi^{ABS}$. The difference between the two flow rates is given by the flow rates into the injection and sample tubes. The flow rate can be expressed in terms of the density n and the average velocity v^a of the nucleons perpendicular to a surface A, and yields, using Eq. (7.16),

$$\Phi_{tot} = A(v_1^a n_1 + v_2^a n_2) = A v_2^a(\sqrt{2}\, n_1 + n_2), \tag{7.17}$$

where the subscripts 1 and 2 denote particles with masses 1 and 2, respectively. Here the surface A is given by the cross section of the cell. The factor $\sqrt{2}$ is the difference in the velocities of the mass 1 and mass 2 particles. In each position along the cell Eq. (7.17) is fulfilled and an integration along the cell yields

$$\sqrt{2}\, d_1^T + d_2^T = \frac{\Phi_{\mathrm{tot}}\, l_c}{A\, v_2^g} = \mathrm{const.}, \tag{7.18}$$

where l_c is the length of the cell. A comparison with the definition of α_r^T in Eq. (7.3)yields the following expression for the total target thickness

$$d^T = \frac{\Phi_{tot}\, l_c}{A\, v_2^g} \left((\sqrt{2}-1)\alpha_r^T + 1\right)^{-1}. \tag{7.19}$$

Because of the dependence of the rates N_L on d^T, Eq. (7.19) can be used to define the normalized luminosity rate

$$L = \frac{N_L}{I_{e+}\, T_c^{\frac{1}{2}}\, \Phi_{\mathrm{tot}}^{\mathrm{TGA}}}, \tag{7.20}$$

which is dependent on the degree of dissociation of the total target. The normalized rates are only dependent on additional parameters of the experiment, which are not constant such as: the HERA beam current and the cell temperature which has influence on the velocity of the hydrogen atoms and molecules. The total flow rate is replaced by the TGA flow rate, which is proportional to the total flow rate and can be measured.

The calibration measurement is carried out in the limits of α_r^T with a pure atomic or molecular target. In the case of a pure atomic target the calibration measurement yields the constant normalized rate

$$C_a = \frac{N_L^a}{I_{e+}\, T_c^{\frac{1}{2}}\, \Phi_a^{\mathrm{TGA}}}. \tag{7.21}$$

The normalized rates divided by the calibration constant give a number between 1 and $\sqrt{2}$ dependent on α_r^T

$$\frac{L}{C_a} = \frac{\sqrt{2}}{(\sqrt{2}-1)\alpha_r^T + 1} \in [1\,,\ \sqrt{2}\,] \tag{7.22}$$

and are independent of the cell temperature and injected flow rate into the cell. Equation (7.22) can be solved for α_r^T and yields $\alpha_{\text{lum}}^T \equiv \alpha_r^T$

$$\alpha_{\text{lum}}^T = \frac{\sqrt{2}\,C_a\,L^{-1} - 1}{\sqrt{2}-1}, \tag{7.23}$$

which gives a direct measurement for the degree of dissociation inside the target cell.

A plot of α_{lum}^T calculated by Eq. (7.23) compared to α_r^{TGA} for several fills in the 1997 running period is shown in Fig. 7.1 and includes high α^T as well as low α^T measurements. The calibration constant is calculated under the assumption that α_{lum}^T equals α^{TGA} for high values of α and yields $C_a = 0.210 \pm 0.002$. The fills at $118 \le t \le 130$ days are used to determine the reference value of C_a (Fig. 7.1, left). The data for a high α were taken under normal running conditions $T_c = 100\,\text{K}$. The low α data were taken to study the polarization of the molecules (Sec. 7.5), which is at present the dominant error on the target polarization. The cell temperature was raised to $T_c = 250\,\text{K}$, to remove most of the water from the cell surface and lower α_r^T.

The relation between α_{lum}^T and α^{TGA} is shown in Fig. 7.1, right. The solid line represents data for α_r^{TGA} (Eq. (3.16)) and α_{lum}^T (Eq. (7.23)) calculated using the age distributions. The measured data are consistent with a calculation with a relation between the recombination coefficients in beam tube and sample tubes of $\gamma_r^c = 10\gamma_r^{\text{sam}}$.

7.3.1 Determination of the Correction Constant for the Degree of Dissociation

The case of an additional contribution of restgas flow and ballistic flow o molecules from the ABS to the target is included into the calculation of α_{lum}^T in Section 7.3 as follows:

$$C_a = \frac{L_a + L_r + L_{\text{rg}} + L_{\text{bal}}}{k_0(\Phi_a^{\text{TGA}} + \Phi_r^{\text{TGA}}) + 2\Phi_{\text{rg}}^{\text{TGA}} + \Phi_{\text{bal}}^{\text{TGA}}} \cdot \frac{1}{I_{e^+} T_c^{\frac{1}{2}}}, \tag{7.24}$$

where k_0 is the correction constant from Eqs. (7.7) and (7.10), which is applied to the measured TGA flow rate of the nucleons injected as atoms and accounts for the change in the density of the nucleons, which have recombined in the target. The normalized rates L_r, L_{rg} and L_{bal} are the respective rates due to the target thicknesses d_a^T, d_r^T, d_{rg}^T and d_{bal}^T. The constant C_a results from the definition of k_0 and represents the calibration constant from Eq. (7.21). Solving Eq. (7.24) for k_0 and using the identity

$$\begin{aligned} L &= L_a + L_r + L_{\text{rg}} + L_{\text{bal}} \\ \Phi_{\text{tot}}^{\text{TGA}} &= \Phi_a^{\text{TGA}} + \Phi_r^{\text{TGA}} + \Phi_{\text{rg}}^{\text{TGA}} + \Phi_{\text{bal}}^{\text{TGA}}, \end{aligned} \tag{7.25}$$

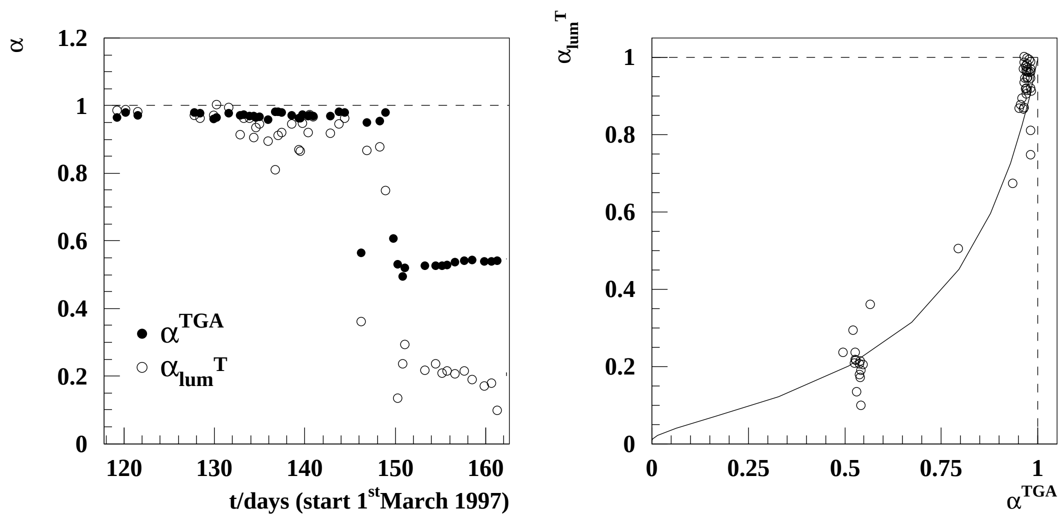

Fig. 7.1: Measurements of α^T_{lum} based on the Luminosity monitor measurements. Values of α^T_{lum} (circles) and α^{TGA} (dots) during a time period with a change in the recombination caused by a high temperature of the cell (left picture). Values of α^T_{lum} compared to the measurements of α^{TGA} during the low alpha studies (right). The solid line is the calculated relation between α^T_r and α^{TGA} based on age distributions for $\gamma^c_r = 10\gamma^{\text{sam}}_r$

which is the measurement of the total rates of L and Φ^{TGA}, it follows

$$k_0 = \left(\frac{1}{C_a} \frac{L}{\left(\Phi^{\text{TGA}}_{\text{tot}} - \Phi^{\text{TGA}}_{\text{rg}} - \Phi^{\text{TGA}}_{\text{bal}}\right)} - \frac{2\Phi^{\text{TGA}}_{\text{rg}} + \Phi^{\text{TGA}}_{\text{bal}}}{\left(\Phi^{\text{TGA}}_{\text{tot}} - \Phi^{\text{TGA}}_{\text{rg}} - \Phi^{\text{TGA}}_{\text{bal}}\right)} \right) \frac{1}{I_{e^+} T_c^{\frac{1}{2}}}, \tag{7.26}$$

where all the different terms involved in this equation are measured separately. The constant C_a is again derived from a measurement with a target without recombination expressed by $k_0 = 1$. It follows from the definition of k_0 that

$$k_0 \in [1\,,\,\sqrt{2}\,] \tag{7.27}$$

and the values of α^T_0 and α^T_r can be directly calculated from Eqs. (7.7) and (7.10).

7.3.2 Uncertainties in the determination of the Correction Coefficient

The measurements of the Luminosity monitor give an alternative method to determine the calibration constant k_0. The presented data show a variation in the quantities α^T_{lum}, which are only seen in the averaged values over one HERA fill (Fig. 4.5), e.g. the time period $t = [132\,d, 144\,d]$. This variation is not seen during a HERA fill, except for the constantly increase over a fills time, and indicates a large systematic uncertainty in the determination of the calibration constant C_a. A comparison of the measured α^T_{lum} and α^{TGA} values during one fill is shown in Fig. 7.2. The left and right picture show the time

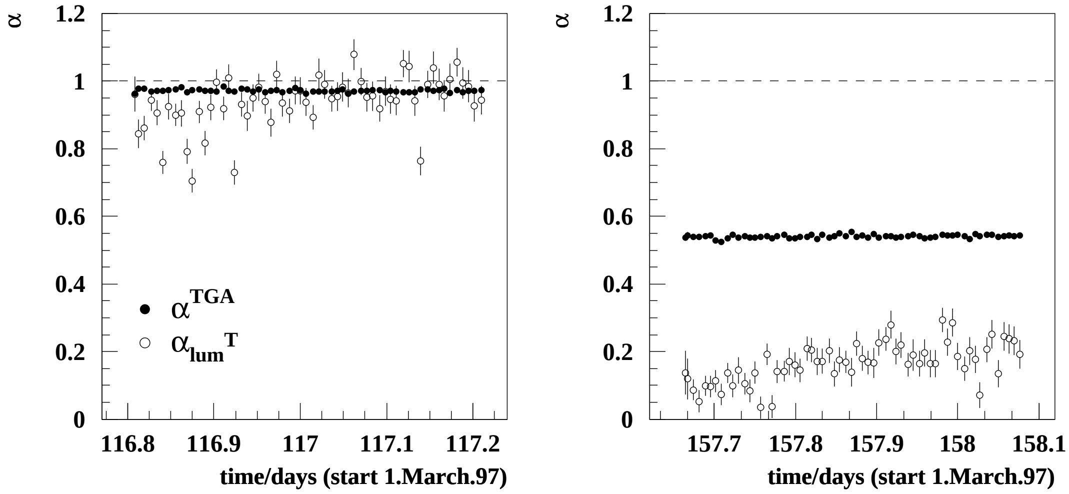

Fig. 7.2: Values of $\alpha^T_{\rm lum}$ (circles) compared to a measurement of $\alpha^{\rm TGA}$ (dots) during a high α (left) at normal running conditions and a low α period (right) at high target cell temperature. Both figures show a time period of one HERA fill.

dependence of both values for a high and low degree of dissociation, respectively, during one HERA fill. The low degree of dissociation was caused by a high temperature of the cell of 250 K. It is clear from both figures that $\alpha^T_{\rm lum}$ shows a lower value at the beginning of the fill, where the positron beam currents are typically $I_{e^+} = 40\,{\rm mA}$, compared to the value at low positron beam currents, which are typically $I_{e^+} = 15\,{\rm mA}$ at the end of the fill. The change in high $\alpha^T_{\rm lum}$ might be identified as due to a change in the amount of water adsorbed on the surface as seen in Fig. 1.5. The cell tube is exposed to beam interactions and the adsorbed water inside the beam tube can pick up energy from the electro magnetic fields, which are caused by the beam. Figure 1.5 also shows that changes in the recombination caused by the HERA beam, which are in the order of 0.1 measured by the TGA, are already seen at high values of $\alpha^{\rm TGA} = 0.85$. Figure 7.2, right, shows a value $\alpha^{1\rm TGA} = 0.5$, which is stable during the HERA fill, but a typical change in $\alpha^T_{\rm lum}$ of 0.1. In addition the low α data were taken with a dry surface, so no water could be removed by the beam. The observed changes must be caused by a different process, which is not understood yet. Possible sources for the systematic uncertainty are the stability of the measurements of the Luminosity monitor rates and the stability of the measurements of the TGA flow rates, which enter as absolute values into the normalized rates L. The rates measured by the Luminosity monitor might depend on the position and slope of the positron beam inside the target cell.

The presented data show that, if the systematic uncertainties are understood in the future, the presented method is able to measure the degree of dissociation seen by the positron beam with a sufficient statistical uncertainty of e.g. $\Delta\alpha^T_{\text{lum}} = \pm 0.05$ within a time period of 600 s.

7.4 Polarization of the Molecules

The polarization of the molecules contributes to the total target polarization as

$$P = (1 - \alpha^T_r) P^T_m. \tag{7.28}$$

The variable P^T_m is defined as the polarization of the nucleons in molecules, which entered the cell as atoms and then recombined inside the cell. The knowledge about the value of P^T_m is important, if significant recombination is found inside the cell. The uncertainty of P^T dependent on P^T_m is given by

$$\Delta P = (1 - \alpha^T_r) \Delta P^T_m \tag{7.29}$$

and at low α^T values the uncertainty in P^T_m might add a significant contribution to the uncertainty in the total target polarization. If P^T_m is unknown an uncertainty of $\Delta P^T_m = 0.5$ at $\alpha^T = 0.9$ will result in a 5% error in P^T.

An expected value of P_m can be deduced from the models of recombination and relaxation. The recombination process discussed in Chap. 4 describes recombination as an interaction of a gaseous atom and an atom adsorbed on the surface and the respective polarizations enter into the polarization of the molecules. The relaxation process discussed in Chap. 5 is caused by a diffusion process of the atoms on the surface, where the atom has to overcome a potential barrier, which is less than the binding energy. The parameters involved in this process could only be measured for the atoms bound to the PH-sites and assumptions have to me made for the diffusion of atoms bound to the CH-sites.

The polarization of the molecules P_m dependent on the initial polarizations of the atoms in the gaseous state and on the surface is given by

$$P_m = \eta_r \, P^{(r)}_a, \tag{7.30}$$

where $P^{(r)}_a$ is the initial polarization of the atoms, which recombine, and η_r is a factor, which accounts for a possible change of the polarization of the nucleons caused by the recombination process. The initial polarization is given by the average polarization of the gaseous atoms $P^{(g)}_a$ and the surface atoms $P^{(s)}_a$, $P^{(r)}_a = (P^{(g)}_a + P^{(s)}_a)/2$. The change of the polarization of the nucleons during the recombination process is expressed as

$$\eta_r = 1 - 2P^{\text{rec}}_{\text{flip}}, \tag{7.31}$$

where $P^{\text{rec}}_{\text{flip}}$ is, according to Eq. (1.2), the probability for a spin flip of a single atom in the sample to occur during the recombination process. A measurement of the polarization of the gaseous atoms exists and the polarization of the atoms bound to the surface $P^{(s)}_a$ and the quantity η_r remain the values of interest.

7.4.1 Initial Polarization of Adsorbed Atoms in the Recombination Process

The polarization $P_a^{(s)}$ of the adatoms, is one term in the calculation of the initial polarization $P_a^{(r)}$ Eq. (7.30). It is calculated as the weighted average of the polarizations of the adatoms on the two types of site, where the relative recombination rates are the weight factors

$$P_a^{(s)} = \frac{\mathcal{R}_1 P_{a,1}^{(s)} + \mathcal{R}_2 P_{a,2}^{(s)}}{\mathcal{R}_1 + \mathcal{R}_2}. \tag{7.32}$$

Figure 4.3, right, shows the contribution of the two binding sites to the recombination as a function of the temperature. Below 80 K the atoms bound to the PH-sites and those bound to the CH-sites above 80 K dominate the recombination process. Due to the difference in binding energy the dwell times differ a lot on both types of sites and the wall relaxation has a different influence on the polarization of the atoms. The relaxation probability per wall collision of the polarized atoms is calculated using Eq. (5.35) and parameters from Sec. 5.3, assuming the same relation of E_0 to ΔE_j and the same value of the fluctuating fields for the CH-sites as for the PH-sites. These assumptions are made, because the polarization measurements are only sensitive to the atoms, which desorb from the PH-sites.

The resulting polarization after a single wall collision of the atoms from the PH-sites is not depleted over most of the temperature range, whereas the atoms, which adsorbed to the CH-sites are expected to be strongly depolarized in the whole temperature range. This is shown in Fig. 7.3, right. No recombination is assumed in this calculation.

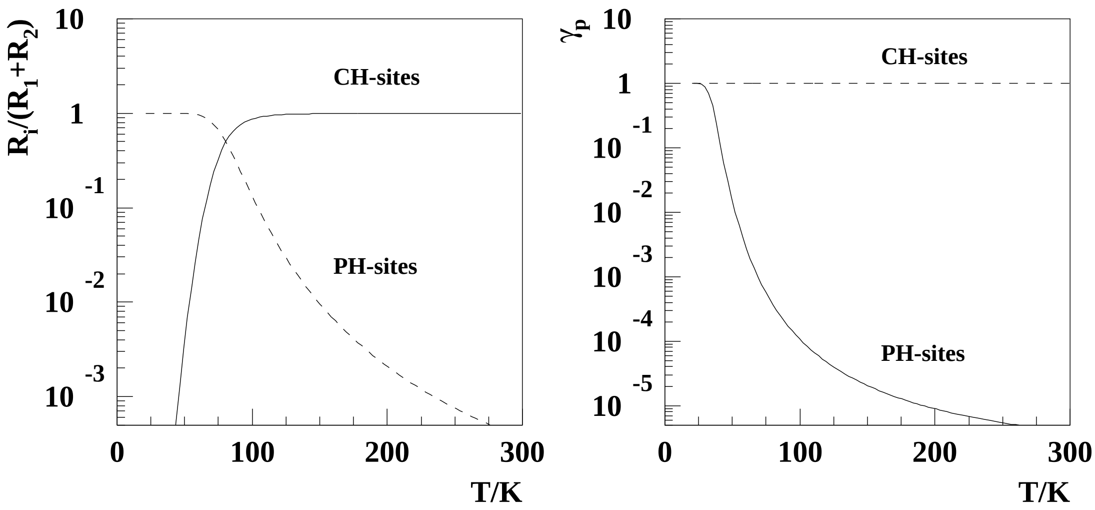

Fig. 7.3: Relative recombination rate and relaxation probability of the desorbed atoms on the two types of sites dependent on cell temperature. The data is based on the parameters fitted in Sec. 5.4 and the assumptions on diffusion energy and strength of the fluctuating fields given in the text.

The evaporation rates from the two binding sites, derived from the recombination measurements in Sec. 5.4 (Fig. 5.2), show that the contribution of the atoms from the CH-sites to the gaseous phase can be neglected. On the other hand it can be seen from the results in Sec. 4.2 that the recombination at temperatures higher than 80 K mainly involves atoms from the CH-sites and that, other than for the calculation of the polarization of the atoms, the CH-sites give the dominant term in the calculation of the polarization of the molecules. In Fig. 7.3, left, the relative rates of molecules, which evaporate from the two types of sites are shown dependent on the temperature (compare Fig. 4.3).

Recombination removes the atoms faster from the surface compared to the desorption process. The average dwell times τ_s and $\tilde{\tau}_s$ for desorption and recombination, respectively, are shown in Fig 7.4, left. The ratio of the initial and final polarization of the atoms

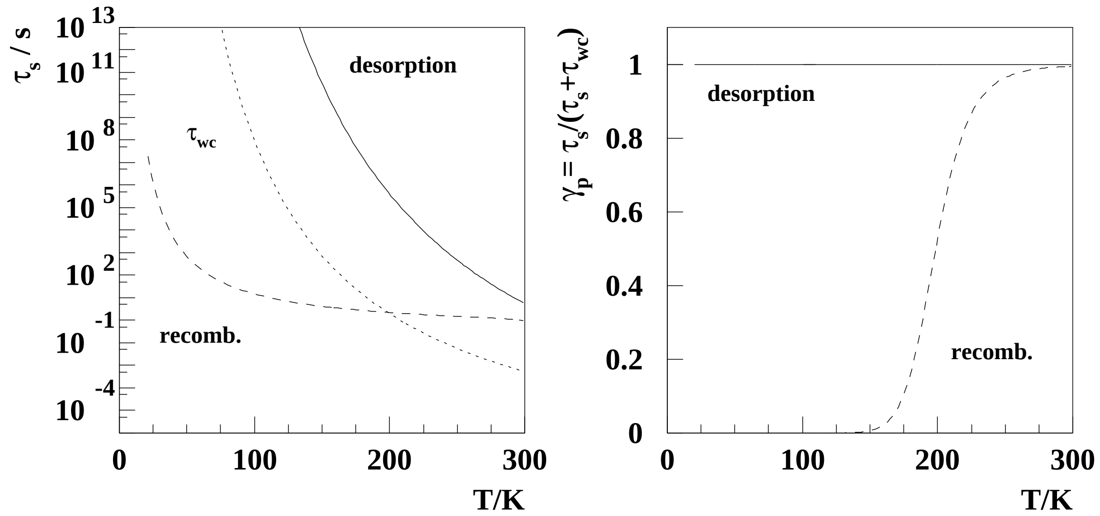

Fig. 7.4: The average dwell time of the atoms on the CH-sites dependent on cell temperature (left picture) for atoms, which desorb from the surface (solid line) and atoms which recombine (dashed line) calculated by Eq. (4.25). The wall relaxation time $\tau_{\rm wc}$ is plotted for comparison (dotted line). The polarizatio relaxation probability γ_p of atoms on the CH-sites is plotted versus temperature in the right picture for atoms which desorb from the surface (solid line) and atoms which recombine (dashed line).

which evaporate or recombine from the CH-sites is shown in Fig. 7.4, right, expressed as γ_p, and shows that the polarization of the recombined nucleons increases with decreasing temperature and no significant depolarization is obtained below 200 K. The calculations are based on the calculated recombination rates which are derived from the recombination measurements in Sec. 4.3. The polarization of the atoms after a single wall collision is strongly temperature and recombination dependent. The polarization depends on the ratio $\tau_{\rm wc}/(\tau_{\rm wc} + \tau_s)$ (Eq.(3.21)) and in the case of missing recombination a long dwell time $\tau_s \gg \tau_{\rm wc}$ leads to a strong depolarization. Additional recombination reduces the dwell time as shown in Fig. 7.4, left, and if the dwell time τ_s is much shorter than τ_{wc}, the depolarization of the atoms which recombine is small too.

The two assumptions, which entered into the calculation of the polarization, were, that the same relation of E_0 to ΔE_j (Sec.5.2) on both types of site and that the same values of the fluctuating fields b_n are found on both types of site. These assumptions have to be questioned for different reasons. The different types of binding at the CH- and PH-sites are one reason. The bond of the atoms to the CH-sites is due to chemisorption and needs to be viewed as a strong perturbation of the hydrogen atom. The depolarization model discussed in Sec. 5.2 is based on the perturbation theory with a weak interaction of the hydrogen atoms with the surrounding environment and is probably not able to describe the interaction with the surface. The second reason is the diffusion process that causes the depolarization. One condition for the surface diffusion is a low enough coverage of the surface. Since a single site is only able to bind a single atom, the diffusion process should be altered by the high coverage, which is seen on the CH-sites.

The recombination rate below 80 K is dominated by the atoms adsorbed on PH-sites. The relaxation model can be applied to those atoms, and their initial polarization in the recombination process is expected to be high at low temperatures, because of the reduced dwell time.

7.4.2 Measurement of the Polarization of the Molecules

A value for the polarization of the molecules in the HERMES target can be determined from the low α_r^T measurements in comparison with the high α_r^T measurements. The asymmetries $A_{||}$ of inclusively measured deep inelasticly scattered positrons at the HERMES experiment allow this comparison. The asymmetries $A_{||}$ are proportional to the target polarization and one yields

$$\frac{A_{||}^{<}}{A_{||}^{>}} = \frac{\alpha_r^{T,>}P_a^{T,>} + (1-\alpha_r^{T,>})P_m^{T,>}}{\alpha_r^{T,<}P_a^{T,<} + (1-\alpha_r^{T,<})P_m^{T,<}}, \tag{7.33}$$

where the super scripts $>$ and $<$ denote the high and low α_r^T measurements, respectively. The measured ratio of molecular and atom polarization in the target defines the quantity β. Under the assumption of $\alpha_r^{T,>} \approx 1$ and equal target and beam polarization for both measurement periods, introducing an additional systematic error of ≈ 0.03, β is given by

$$\beta = \frac{P_m^{T,<}}{P_a^{T,<}} \approx \left(\frac{A_{||}^{<}}{A_{||}^{>}} - \alpha_{\mathrm{lum}}^{T,<}\right)\left(1-\alpha_{\mathrm{lum}}^{T,<}\right)^{-1}. \tag{7.34}$$

This value gives a limit on the product of η_r and P_m, because the two quantities are not independent on each other in this measurement (Eq. (7.31)).

The limiting cases are shown in Tab. 7.1 for a general case with an initial polarization of the gaseous atoms of $P_a^{(g)} = 1$ and the assumption, that the polarization of the atoms on the surface $P_a^{(s)}$ is either 0 or 1. If $\beta = P_m/P_a^{(g)} = 0$, the only limit, which can be set

$\beta = P_m/P_a^{(g)}$	$P_a^{(g)}$	$P_a^{(s)}$	$P_a,^{(r)}$	η_r	$P_{\text{flip}}^{\text{rec}}$
0	1	0	$\frac{1}{2}$	0	$\frac{1}{2}$
0	1	1	1	0	$\frac{1}{2}$
$\frac{1}{2}$	1	0	$\frac{1}{2}$	1	0
$\frac{1}{2}$	1	1	1	$\frac{1}{2}$	$\frac{1}{4}$
1	1	1	1	1	0

Tab. 7.1: Limiting cases for the determination of P_m and β with an initial polarization of the gaseous atoms of $P_a^{(g)} = 1$.

is $\eta_r = 0$, and no information about the polarization of the molecules is gained. If $\beta = \frac{1}{2}$, the two cases give the limit $\eta_r \in [\frac{1}{2}, 1]$. If $\beta = 1$, all quantities are fixed at the maximum value 1. The quantity η_r is assumed to be a general property of the recombination process and can also be measured in different experiments.

The measurements with a low α^T traget were taken at a cell temperature of 250 K and a dry Drifilm coated cell, which was exposed to the positron beam for ca. 150 days. The measured degree of dissociation in the TGA was $\alpha^T \approx 0.5$ (see Fig. C.2). A preliminary analysis of the asymmetries with reduced statistics [Mar97], in combination with the analysis of α_{lum} obtains a value of

$$\beta = \frac{P_m^{T,<}}{P_a^{T,>}} = 0.56 \pm 0.16_{\text{stat}} \pm 0.15_{\text{sys}}. \tag{7.35}$$

This result can be identified with as third and fourth case in Tab. 7.1, which sets limits on the value of $\eta_r \in [\frac{1}{2}, 1]$ dependent on $P_m^{T,<}$. The cases $\beta = 0$ and $\beta = 1$ in Tab. 7.1 are excluded.

Based on this result limits on the polarization of the molecules at a cell temperature of 100 K can be estimated under the assumption that η_r is independent of the temperature. The lower limit $\eta_r = \frac{1}{2}$ restricts the molecular polarization to values of $\beta \in [\frac{1}{4}, \frac{1}{2}]$ and the higher limit $\eta_r = 1$ restricts the molecular polarization to values of $\beta \in [\frac{1}{2}, 1]$. At present, without knowledge of the value of η_r, the polarization of the molecules at a cell temperature of 100 K can be restricted to $\beta \in [\frac{1}{4}, 1]$, if further analysis of the asymmetries and an improved error yield the result discussed above.

It should be noted, that, according to Sec. 7.4.1, in the case of $P_a^{(g)} \ll 1$, values of $\beta > 1$ are possible. The measured values of the atomic polarization in the temperature range of the high and low α measurements (Eq. (7.35)) are $P^{\text{BRP}} \approx 0.92$, so that the assumptions of $P_a^{(g)} = 1$, $P_a^{(s)} \leq P_a^{(g)}$ and $\beta \leq 1$ in the previous discussion are appropriate.

7.5 Errors of the Determination of the Target Polarization

With the definition of β in Eq. (7.34) the formula for the target polarization, Eq. (7.1), can be written as

$$P^T = \alpha_0^T P_a^T \left(\alpha_r^T + (1 - \alpha_r^T)\beta\right), \tag{7.36}$$

where the uncertainty due to the recombination and polarization of the molecules results as

$$\Delta P^T(\alpha_r^T, \beta) = \alpha_0^T P_a^T \left[\left((1-\alpha_r^T)\Delta\beta\right)^2 + \left((1-\beta)\Delta\alpha_r^T\right)^2\right]^{\frac{1}{2}}. \tag{7.37}$$

The value of β gives a weight on the uncertainty of α_r^T, and vice versa. As a consequence, the results of Sec. 7.4.2 lead to a reduction of the uncertainty in the measurement of the degree of dissociation.

The error on the determination of the target polarization includes the uncertainties of the following quantities:

- the measurement of P^{BRP}, including the efficiencies of the RF transitions,
- the correction factor c^P,
- the measurement of β,
- the measurement of α_0^{TGA} and α_r^{TGA} including the calibration constant κ,
- flow rates $\Phi_{\mathrm{bal}}^{\mathrm{TGA}}$ and $\Phi_{\mathrm{rg}}^{\mathrm{TGA}}$,
- the correction factor k_0 and c_r^α.

The values of the systematic errors for the TGA and BRP measurements are listed in Tab. 7.2. The statistical errors listed are those during normal operation of the target with a spin reversal time of 60 s. The errors of the BRP RF-transition efficiencies are listed in Tab. A.2.

Quantity	Error	
α_r^{TGA}	$\pm\,0.02_{\mathrm{stat}}$	$\pm\,0.01_{\mathrm{sys}}$
α_0^{TGA}	$\pm\,0.02_{\mathrm{stat}}$	$\pm\,0.01_{\mathrm{sys}}$
P^{BRP}	$\pm\,0.019_{\mathrm{stat}}$	$\pm\,0.009_{\mathrm{sys}}$

Tab. 7.2: Errors of the polarization and degree of dissociation measurements during the data taking period in 1997.

The measurement of P_m^T enters into the calculation of the polarization based on the measurements of the asymmetries at high and low α^T. The value of P_m^T can generally be restricted based on the measurement of $P_m^T/P_a^{(g)}$ Sec. 7.4.2. At present the interval $P_m^T \in [0.25, 1] \pm 0.125_{\mathrm{stat+sys}}$ is obtained.

The factor k_0 enters into the calculation of α_0^T and α_r^T and the factor c_r^α into the calculation of α_r^T (Eqs. (7.7) to (7.7)). These factors result from Monte-Carlo simulations. The presented simulations are not able to give small systematic errors, because they do not involve the interaction of the atoms on different surfaces. More advanced Monte-Carlo studies, which include different recombination and relaxation probabilities are needed. An alternative method to derive the correction factor k_0 is given by the combined measurements of TGA and Luminosity monitor (Sec. 7.3.2), which needs further investigation of the systematic uncertainties.

8 Conclusion

The recombination and depolarizing processes in the HERMES internal target were studied in the present work. Measurements were performed on

- recombination of the target atoms,
- depolarisation of the target atoms due to wall relaxation, and
- depolarisation caused by the interaction of the target atoms with the HERA positron beam.

The polarization and degree of dissociation in the target was studied by analyzing a sample beam from the target cell. Due to the diffusion of the particles inside the target cell the atoms or molecules, which are detected in the TGA and BRP, have a characteristic wall collision age distribution. Therefore the measured quantities on recombination and polarization are substantially modified. To gain information about the polarization and degree of dissociation inside the target cell, based on the measurements of TGA and BRP, the effect of the recombination and relaxation probabilities on the respective age distribution was analyzed.

Mont-Carlo Simulations were performed, which were developed within the HERMES target group to simulate molecular flow of atoms and molecules inside the HERMES target cell, taking into account the different acceptance of the TGA and BRP for the particles leaving the sample tube. An analytical model based on the diffusion of particles in tubes was used to describe the results of the Monte-Carlo simulations. The parameters for the mean path length λ of the particles inside the cell and the effective length of the cell z' due to the conductance, which determines the diffusion process and the density distribution, are in agreement within 3% and 1.5%, respectively. This gives confidence in the Monte-Carlo simulations and shows that the alternative method of calculating rate equations, which are based on the diffusion equation and include the spin exchange collisions, are an equivalent description for the interactions of the atoms inside the target cell.

The measurements of the TGA and BRP and their calibration were described. The calibration result in systematic uncertainties of $\Delta\alpha^{\mathrm{TGA}} = 0.01$ and $\Delta P^{\mathrm{BRP}} = 0.009$. The detection of the molecular background in the target cell, consisting of restgas flux from the target chamber and ballistic flow of undissociated molecules from the ABS dissociator, is based on measurements of the TGA and results in a systematic uncertainty of $\Delta\alpha_0^{\mathrm{TGA}} = 0.01$.

Recombination The measurements of the degree of dissociation of the sample beam were taken over the temperature range 35 K<250 K with a Drifilm coated cell and over 35 K<110 K for the water coated Drifilm cell. The measured degree of dissociation was in the range $\alpha^{\mathrm{TGA}} \in [0.4-0.98]$. The data were analyzed based on a model for recombination, which describes the recombination process by the collision of a gaseous atom with an adsorbed atoms on the surface, which are be bound to different types of sites through chemisorption and physisorption. An expression for the recombination probability per wall collision was derived and included in the calculation of the age distributions. Each bound state of the atom is described by a binding energy and harmonic potential, where binding energies of $E_0^{(1)} = (0.611 \pm 0.015)\,\mathrm{eV}$ and $E_0^{(2)} = (0.0318 \pm 0.0004)\,\mathrm{eV}$ are obtained for the chemisoprtion and physisorption sites on the Drifilm coated cell, respectively. The temperature dependence of the coverage of the atoms on both types of sites was in agreement with a Langmuir adsorption isotherm. The desorption and recombination rates calculated from this model have an average dwell time of the desorbing atoms on the surface of $\tau_s = \tau_s^0 \exp(E_0/\mathrm{k}T)$, where $\tau_s^0 = (1.0 \pm 0.2) \cdot 10^{-10}\,\mathrm{s}$, the average dwell time in the high temperature limit, was obtained. The measurements with water adsorbed on the Drifilm coating of the cell, showed a significantly different recombination behavior and a degree of dissociation close to unity for most of the measured temperatures. The temperature dependence of the coverage of the atoms on the sites could not be explained by a Langmuir adsorption isotherm.

Spin Relaxation The measurements of the polarization data were taken simultaneously with the recombination measurements. A 3.5% loss in polarization was measured as an effect of the spin exchange collisions on the polarization of the sampled atoms. The data were analyzed based on a model in which surface diffusion is the underlying process for the relaxation on the surface and which is in agreement with the assumption of a Langmuir type of adsorption of the atoms. An expression for the relaxation probability per wall collision was derived and in addition to the recombination probability included in the calculation of the age distributions. The diffusion of the atoms on the surface is described by a correlation time $\tau_c = \tau_c^0 \exp(\Delta E_j/\mathrm{k}T)$, which can be identified as a inverse jump frequency of the atoms on the surface, where the energy ΔE_j is the potential barrier they have to overcome during the diffusion process. The values for the diffusion on the physisorption sites obtained from the measurements are in fair agreement with $\tau_c^0 = 2.5 \cdot 10^{-12}\,\mathrm{s}$ and $\Delta E_j^{(2)} = 0.49\, E_0^{(2)}$ for the Drifilm coated cell. The comparison with the water adsorbed on the surface showed only a small change in the measured polarization, although the data give evidence that the fluctuating magnetic fields seen by the atoms due to the diffusion process increased. The correlation time τ_c^0 increased while the the energy ΔE_j decreased, which is both in agreement. In addition the increase of the magnitude of the fluctuating fields from 6.5 mT to 17 mT lead to an increase of the relaxation probability per wall collision from $5 \cdot 10^{-5}$ to $2 \cdot 10^{-4}$ at 100,K, which is comparable to the effect due to spin exchange collisions, and a polarization of $P^{\mathrm{BRP}} = 0.92$ measured by the BRP.

Beam Induced Spin Depolarizing Resonances Measurements of the proton and electron depolarizing resonances were made by scanning the magnetic holding field of the target over a range in magnetic field, where the resonance condition given by the frequency of a harmonic of the highly bunched positron beam and the transition frequency between two hyperfine states of the atom is met. The resonance condition for the electron resonances is met at very high harmonics of the beam. The dependence of the transition probability on the amplitude of the beam harmonics allows to measure the envelope of the Fourier spectra of the positron bunches, and a value of $\Delta z_{\mathrm{fwhm}} = (16.5 \pm 0.5)$ mm was obtained. In the case of the proton resonances the measured resonances appeared at the expected positions regarding the magnetic holding field and can be resolved. A model based on the cell geometry and the acceptance of the BRP was able to reproduce the measured resonance shape. The assumption that the interaction between the hydrogen atoms and the transient fields of the beam is located inside a cylinder around the positron beam allowed to estimate the fraction of the cell which is covered by the resonances. An average interaction path of $l_{int} = 2.5$ mm was obtained with a maximum length of the resonant area along the beam of 45 mm. The spacing between the resonances at the working point and the uniformity of the target magnet is sufficient to avoid depolarization of the target atoms during run of the experiment.

The Average Target Polarization The average target polarization is the weighted sum P_a^T and P_m^T, where the weight given each is expressed by the degree of dissociation α_r^T. The degree of dissociation α_0^T gives the fraction of initial number of nucleons in atoms entering the target. The difference of the quantities of α_0^T, α_r^T, and P_a^T to the quantities measured in TGA and BRP can be expressed by correction factors, which are calculated by means of Monte-Carlo simulations. As an alternative a measurement of the correction factors for α_0^T and α_r^T with was presented, but shows large systematic uncertainties. The interactions of the beam with the cell surface have a strong effect on the recombination if water is adsorbed on the surface. Because the sample and extension tubes are mainly not affected by the interaction an inhomogeneous surface regarding the relaxation and recombination probabilities is expected. An extension of the simulations to multiple relaxation and recombination probabilities at different locations in the cell and sample tubes is required. The polarization of the molecules could be restricted for the nominal target cell temperature of 100 K to values $P_m^T \in [0.25, 1] \pm 0.125_{\mathrm{stat+sys}}$ based on the comparison of the measured asymmetries $A_{||}$ at high and low α^T.

The measurements of the degree of dissociation have shown a value of $\alpha_r^T \approx 0.9 - .95$ at 100,K cell temperature with an undamaged Drifilm coating of the cell. During run of the experiment the Drifilm coating is affected by the beam intreactions and values $\alpha_r^T \approx 0.2$ were observed. Evidence is given, that water adsorbs on the cell surface, which originates from the ABS dissociator. The recombination and polarization was measured on both surfaces, a clean cell and a water covered cell, and shows that the water layer inhibits recombination, with values $\alpha_r^{\mathrm{TGA}} \approx 1$ observed on a water covered cell. The effect of the water layer on the polarization of the atoms is small and measured values of $P^{\mathrm{BRP}} = 0.92$, $\alpha_r^{\mathrm{TGA}} \approx 1$, and $\alpha_0^{\mathrm{TGA}} \approx 0.97$ were obtained in the case of a fully optimized operation of the target.

A BRP Beams and Efficiencies

Table A.1 shows the different beam signals which can be measured by the BRP dependent on the RF transition units. All of the shown settings are used for a calibration measurement (Sec 2.6.2). Table A.2 shows the measured values of the efficiencies of the BRP transition units.

Beam I	SFT 1-4		SFT 2-4		MFT 1-3	MFT 2-3
index	RF	field	RF	field	RF & field	RF & field
off	off	off	off	off	off	off
s14	on	on	—	—	off	off
s24	—	—	on	on	off	off
m13cs14	off	on	—	—	on	—
m13s14	on	on	—	—	on	—
m23cs14	off	on	—	—	—	on
m23s14	on	on	—	—	—	on
m13cs24	—	—	off	on	on	—
m13s24	—	—	on	on	on	—
m23cs24	—	—	off	on	—	on
m23s24	—	—	on	on	—	on

Tab. A.1: Definition of the BRP beam indices.

Efficiency	ε_j	$\pm$	$(\sigma_\varepsilon)_j$	Efficiency	ε_j	$\pm$	$(\sigma_\varepsilon)_j$
s14	0.9958	$\pm$	0.0124	s24	1.0041	$\pm$	0.0098
m13r12cs14	0.9927	$\pm$	0.0103	m13r12cs24	0.9994	$\pm$	0.0067
m13r23cs14	0.9974	$\pm$	0.0132	m13r23cs24	0.8344	$\pm$	0.0077
m23r12cs14	0.0021	$\pm$	0.0106	m23r12cs24	0.0168	$\pm$	0.0103
m23r23cs14	0.9825	$\pm$	0.0119	m23r23cs24	0.9862	$\pm$	0.0101

Tab. A.2: Values for the BRP efficiencies. The first three letters of the MFT indicate the transition in general, MFT 1-3 or MFT 2-3, the letter 'r' indicates the sub-transition efficiency (1-2) or (2-3), and the letter 'c' indicates the status of the SFT magnetic field setting, SFT 1-4 or SFT 2-4.

B Contents of the Target Ntuple

Device	Symbol	Data
Time	tim	start and stop time of the event
BRP	pol	polarization, occupation numbers
BRP	per	error on pcb
BRP	pcb	corrected beam signals and errors
TGA	dcb	corrected beam signals and errors
ABS	abs	ABS pressures, valve/RFT status
BRP	brp	TGA/BRP pressures, RFT status, emis. current
Cell	cry	cryo status
DAQ	daq	HERMES run status, run number
HERA	hec	HERA positron current
HERA	hee	HERA positron energy
Lumi Monitor	lum	luminosity monitor count rates
Spectrometer	mag	HERMES spectrometer magnetic field
Cell	oxb	cell temperatures
Target chamber	tav	target chamber pressures
Target magnet	vme	target magnetic field
TGA	tga	calculated degree of dissociation

Tab. B.1: Main contents of the target ntuple.

C 1996 and 1997 Overview

An overview of the polarization of the nucleons, injected states $|1\rangle$ and $|4\rangle$, the degree of dissociation α_r^{TGA} and the cell temperature T_c is shown in Figures C.1 and C.2 for the data taking periods in 1996 and 1997, respectively.

1996 Overview:

The upper graph shows the BRP measurement of the proton polarization, with an average polarization of 86% for time periods during data taking of the HERMES experiment. The letter R indicates the time period, where the polarization was lowered by beam induced resonances. The magnetic holding field was adjusted after $t = 20d$ to a value between the resonances.

The graph in the center shows the TGA measurement of the degree of dissociation for time periods during data taking of the HERMES experiment. The letter V indicates a venting of the target chamber and the resulting drop in α_r. The letter D indicates the measurements after the HERA beam was accidentally dumped near the target region.

The lower graph shows the cell temperature for all times when the ABS injected polarized hydrogen into the cell. The cell temperature at normal operation of the target is 100 K. The letter L indicates measurements with a low cell temperature for the TGA calibration. The letter H indicates a warm up of the cell to 280 K for studies on changes in the cell surface.

1997 Overview:

The upper graph shows the BRP measurement of the proton polarization, with an average polarization above 90% during data taking of the HERMES experiment. The letter B indicates time periods, in which the target operated in bhabha-mode ('ehx').

The graph in the center shows the TGA measurement of the degree of dissociation during data taking of the HERMES experiment. The letter D indicates the measurements after a HERA beam dump in the target region. The letter H indicates the measurements with a high cell temperature. The letter T indicates the improvement of the control software. The ratio of time periods for measurements of mass 1 and mass 2 were redefined to decrease the statistical error. The increase in the measured α^{TGA} value in respect to the measure values in 1996 is caused by an increase of the water flow into the target cell by increasing the oxygen admixture to the ABS dissociator.

The lower graph shows the cell temperature for all time periods in which the ABS injected polarized hydrogen into the cell. The cell temperature at normal operation of the target is 100 K. The letter L indicates measurements with a low cell temperature for the TGA calibration.

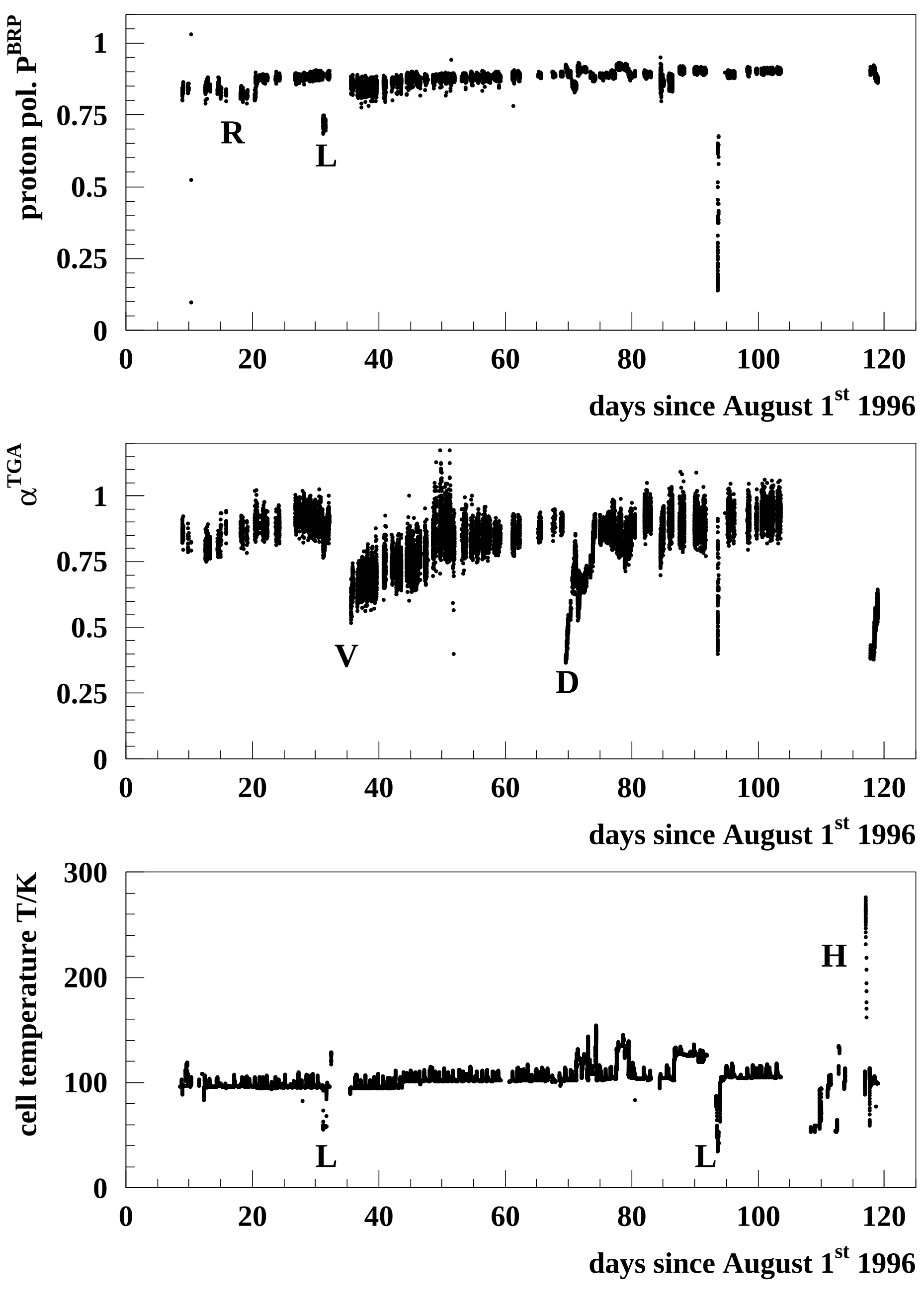

Fig. C.1: Proton polarization P^{BRP} and degree of dissociation α^{TGA} during data taking in 1996. The target cell temperature is plotted for all time periods with the ABS running during the data taking period 1996.

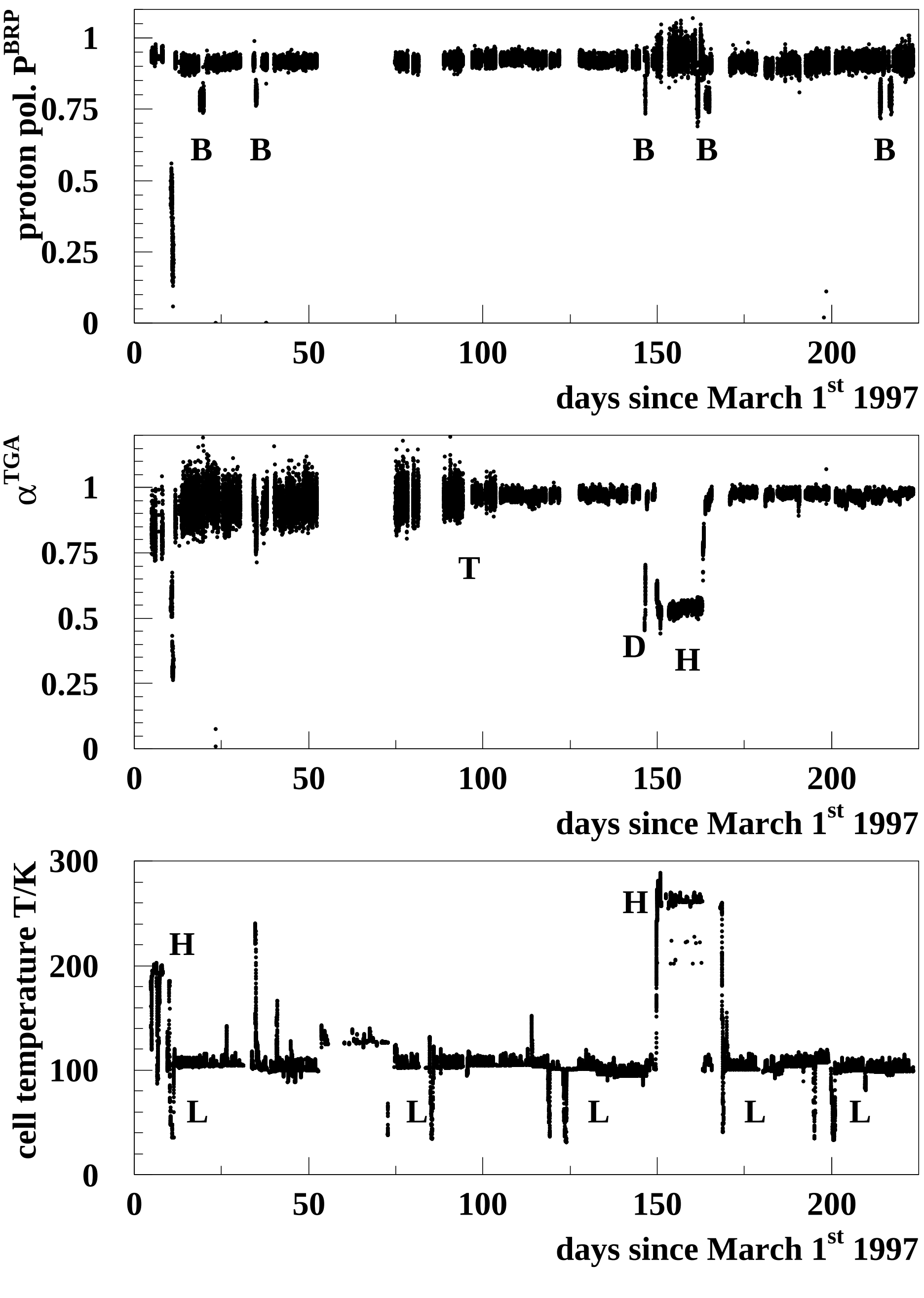

Fig. C.2: Proton polarization P^{BRP} and degree of dissociation α^{TGA} during data taking in 1997. The target cell temperature is plotted for all time periods with the ABS running during the data taking period 1997.

References

[Ade93] B. Adeva et. al.; Phys. Lett. **B302**, (1993) 533

[Abe95] E-142, K. Abe et. al.; Phys. Rev. Lett. **74**, (1995) 346

[Abr58] A. Abragam, J. M. Winter; Phys. Rev. Lett. **1**, (1958) 375

[Abr78] A. Abragam; "Principles of Nucelar Magnetism", University Press, Oxford (1978)

[Al76] SLAC-Yale E-80 Collaboration, M. J. Alguard et. al.; Phys. Rev. Lett. **37**, (1976) 1261; **41**, (1978) 70

[All72] A. C. Allison; Phys. Rev. **A5**, (1972) 2695

[Ant93] E-142, P. L. Anthony et. al.; Phys. Rev. Lett. **71**, (1993) 959

[Ash88] EMC, J. Ashman et. al.; Phys. Lett. **B206**, (1988) 364

[Bau83] SLAC-Yale E-80 Collaboration, G. Baum et. al.; Phys. Rev. Lett. **51**, (1983) 115

[Bau96] Ch. Baumgarten; Diplomarbeit, Univ. Hamburg (1996)

[Ben98] T. Benisch; Ph.D. Thesis, Universität Erlangen – nürnberg (1998), to be published

[Blo48] N. Bloembergen,E. Purcell, and P.V. Pound; Phys. Rev. **73**, (1948) 697

[Bra90] B. Braun, Diplomarbeit, Heidelberg (1990)

[Bra92] B. Braun et. al.; Annual Report 1992, Max Planck Institut für Kernphysik, Heidelberg

[Bra95] B. Braun; Dissertation, LMU München (1995)

[Bra97] B. Braun; Proc. Pol. Beams and Pol. Gas Targets, Urbana-Champaign 1997; pp. 156

[Bra] B. Braun; Universität Erlangen, private comunication 1997

[Che76] P. Chen; "The Entity Relationship Model – Toward a Unified View of Data", ACM Transactions on Database Systems 1 (1976) 9

[Dre83] W. Deves et. al.; Phys. Rev. Lett. **50**, (1983) 1795

[Hae67] W. Haeberli, Ann. Rev. Nucl. Sci. **17**, (1967) 373

[Her90] HERMES Collaboration, K. Coulter et. al.; Proposal DESY-PRC 90/01 (1990)

[Her93] HERMES Collaboration; Technical Design Report DESY-PRC 93/06 (1993)

[Des76] M. Desaintfuscien and C. Audoin; Phys. Rev. **A 13** (1976) 2070

[Dmi85] V. F. Dmitriev et. al.; Phys. Lett. **157B**, (1985) 143

[Dun84] J. S. Dunham et. al.; Nucl. Inst. Meth. **219**, (1984) 46

[Dre83] W. Dreves, et. al.; Phys. Rev. Lett **50** (1983) 1759

[Fis93] S. M. Fischer; "The ADAMO Data System. Programmers Manual – Version 3.2", CERN–EPC and Rutherford Appleton Laboratory (UK) (1993)

[Flo67] E. A. Flood; "The Solid-Gas Interface" (Dekker, New York; 1967); Vol. 1

[Fow66] R. H. Fowler; "Statistical Mechanics", 2. Ed., (Cambridge, 1966)

[Gau92] H. G. Gaul and E. Steffens; Nucl. Inst. Meth. **A 316**, (1992) 297

[Gel71] A. Gelb and S. K. Kim; J. Chem. Phys. **55**, (1971) 4939

[Gil90] R. A. Gilman et. al.; Phys. Rev. Lett **55**, (1990) 1733

[Gol90] R. A. Gilman et. al.; Phys. Rev. Lett **55**, (1990) 1733

[Hir41] J. O. Hirschfelder; J. Chem. Phys. **9**, (1941) 645

[Hor82] B. Horn, W. Dreves, and D. Fick; Condensed Matter **48**, (1982) 335

[Kim67] S. K. Kim; J. Chem. Phys. **46**; (1967) 123

[Kin91a] E.R. Kinney; "Simulations of the Atomic Polarization and Density in the HERMES Polarized Internal Target", HERMES Internal Report 3/90, (1991)

[Kin91b] E.R. Kinney; Proc. Pol. Gas Targets and Storage Rings, Heidelberg 1991, pp. 155

[Kin93] E.R. Kinney; Proc. Pol. Ion Sources and Pol. Gas Targets, Madison 1993, pp. 78

[Kor90] W. Korsch; Dissertation, Univ. Heidelberg (1990) (1967) 291, and references contained therein.

[Lor93] W. Lorentzon et. al.; Phys. Rev **A47**, (1993) 468

[Mar97] J. Martin; HERMES Collaboration meeting, August 1997

[Mem88] U. Memmert et. al.; Hyperfine Interactions **39**, (1988) 295

[Met96] A. Metz; Diplomarbeit, LMU München (1996)

[MFun95] M. A. Funk; The PINK Documentation page, `http://www-hermes/pink` (1995)

[Pre94] W. Preyß; Dissertation, Universistät Marburg (1994)

[Pre] W. Preyß, private comunication

[Pri93a] J. S. Price; Ph.D. Thesis, University of Wisconsin-Madison (1993)

[Pri93b] J. S. Price and W. Haeberli; Nucl. Instr. Meth. **A326**, (1993) 416

[Pur56] E. M. Purcell and G. B. Field; Astrophys. J. **124**, (1956) 542

[Ree81] D. A. Reed and G. Ehrlich; Surface Science **102**, (1981) 588

[Sch49] K. E. Shuler and K. J. Laidler; J. Chem. Phys. **17**, (1949) 1212

[Sch81] C. A. Scholl; J. Phys. C: Solid State Phys. **14**, (1981) 447

[Sir88] S. Sircar and A. L. Myers; Surface Science **205**, (1988) 353

[Sol64] A. A. Solokov and I. M. Ternov; Sov. Phys. Dokl. **8**, (1964) 1203

[Ste95] J.A. Stewart; Proc. Pol. Beams and Pol. Gas Targets, Cologne 1995, pp. 408

[Ste97] J.A. Stewart; Proc. Pol. Beams and Pol. Gas Targets, Urbana-Champaign 1997; pp. 69

[Sto94a] F. Stock; Ph.D. thesis, Univ. Heidelberg (1994)

[Sto94b] F. Stock, et. al.; Nucl. Instr. Meth. **A343**, (1994) 334

[Sto95] F. Stock; Proc. Pol. Beams and Pol. Gas Targets, Cologne 1995, pp. 260

[Swe85] D. R. Swenson, D. Tupa and L. W. Anderson; J. Phys. B: At. Mol.Phys. **18**, (1985) 4433

[UFun95] U. Funk; Diplomarbeit, Univ. Heidelberg 1995

[Vdb97] J. van den Brand et. al.; Phys. Rev. Letters **78** (1997) 1235

[Wal93] T. Walker and L. W. Anderson; Nucl. Instr. Meth. **A 334**, (1993) 313

[Wan95] W. Wander et. al.; "DAD – Distributed ADAMO Database System at HERMES", Proc. of CHEP 1995, Rio de Janeiro, (1995)

[Wil] F. Willeke; DESY Hamburg, private comunication

[Wis67] H. Wise and B. J. Wood; Advan. Mol. At. Phys. **3**, (1967) 291, and references contained therein.

[Wit56] J. P. Wittke and R. H. Dicke; Phys. Rev. **103**, (1953) 620

[Zho96] Z.-L. Zhou et. al.; Nucl. Instr. and Methods in Phys. Res. **A 378** (1996) 40